

DISSERTATION

EMERGENT TOPOLOGICAL PHENOMENA IN LOW-D SYSTEMS INDUCED BY GAUGE
POTENTIALS

Submitted by

Aidan Winblad

Department of Physics

In partial fulfillment of the requirements

For the Degree of Doctor of Philosophy

Colorado State University

Fort Collins, Colorado

Fall 2024

Doctoral Committee:

Advisor: Hua Chen

Richard Eykholt

Martin Gelfand

Olivier Pinaud

ABSTRACT

EMERGENT TOPOLOGICAL PHENOMENA IN LOW-D SYSTEMS INDUCED BY GAUGE
POTENTIALS

In this dissertation we discuss how gauge potentials can be used as a key ingredient for inducing topological phase transitions in condensed matter systems, such as conductors, insulators, and superconductors. ~~We will cover~~ some important background physics: Maxwell's ~~equation~~, gauge invariance, minimal coupling, and Peierls phase. A review of how one can ~~achieve~~ Majorana fermions in superconductors ~~is shown~~ and their importance to topological quantum computing. ~~Followed by some~~ basics of Landau ~~level in relation~~ to the Chern number, ~~a parameter that indicates if a system is in a non-trivial topological phase~~. Then, ~~applying these concepts to superconductors and conductors, for 2D electron gases (2DEG) and Dirac systems, we see topological phenomena occur.~~

~~In the case of a superconductor we can induce~~ topological phase transitions that allow for Majorana fermions to be hosted and rotated along the corners of a hollow equilateral triangle, a basic building block for ~~a topological quantum logic gate~~. This provides a potential new avenue for achieving a topological quantum computation where a network of interconnected triangular islands allows for braiding of Majorana fermions.

For ~~2DEG~~ and Dirac systems we show ~~oblique incident circularly polarized light~~, using Floquet theory and high-frequency expansion, can ~~achieve Landau Levels~~, or quantum Hall effect, where the effective magnetic field is related to the electric field of the laser light. Outside of having the electric field as a useful parameter for achieving a QHE device, ~~this lets us explore non-equilibrium systems which is a burgeoning field of interest in condensed matter physics.~~

ACKNOWLEDGEMENTS

DEDICATION

I would like to dedicate this dissertation to my dog, Zeta.

42	ABSTRACT	ii
43	ACKNOWLEDGEMENTS	iii
44	DEDICATION	iv
45	LIST OF TABLES	vii
46	LIST OF FIGURES	viii
47	Chapter 1 Introduction	1
48	1.1 Maxwell's equations and gauge transformations	1
49	1.2 Minimal coupling and Canonical momentum	2
50	1.3 Peierls phase in tight-binding models	5
51	1.4 Majorana fermions and topological superconductors	6
52	1.4.1 Kitaev chain	8
53	1.4.2 Half-quantum vortices in p -wave superconductors	10
54	1.4.3 Braiding	13
55	1.4.4 T-junction qubit	14
56	1.4.5 Effective p -wave superconductors	15
57	1.5 Landau levels and quantum Hall effect	20
58	1.5.1 Landau levels in condensed matter systems	20
59	1.5.2 Quantized Hall conductivity and Chern number	23
60	1.5.3 Laughlin pump on a Hall cylinder	25
61	Chapter 2 Superconducting Triangular Islands as a Platform for Manipulating Majorana Zero Modes	27
62	2.1 Context	27
63	2.2 Paper abstract	27
64	2.3 Supplemental material	38
66	Chapter 3 Landau Level-Like Topological Floquet Hamiltonians	51
67	3.1 Introduction	51
68	3.2 Floquet Landau level-like bands in Dirac systems	52
69	3.3 Floquet Landau level-like bands in 2DEG systems	56
70	3.4 Discussion and conclusion	58
71	Chapter 4 Conclusion	62
72	Appendices	64
73	Appendix Chapter A Superconducting Triangular Islands	64
74	A.1 Kitaev chain	64
75	A.2 Gauge potential and gauge invariance	79
76	A.3 Kitaev Triangle and Peierls substitution	81

77	Appendix Chapter B	Landau Level-Like Topological Floquet Hamiltonians	84
78	B.1	Quantum harmonic oscillator	84
79	B.2	Dirac equation in the presence of a magnetic field	87
80	B.3	General framework of Floquet theory	89
81	B.4	High Frequency (Van Vleck) expansion from degenerate perturbation the-	
82		ory	95
83	B.4.1	Non-uniform circularly polarized light on Dirac	97
84	B.4.2	Non-uniform circularly polarized light on 2DEG	99
85	B.5	Tight-binding model Dirac	101
86	B.6	Tight-binding model 2DEG	105
87	B.7	Chern number of Landau levels	109
88	Bibliography		118

LIST OF TABLES

91	1.1	The top chain represents the system in a trivial topology where each complex fermion $c_j = \frac{1}{2}(a_j + ib_j)$ is a linear combination of intraconnected MFs. The bottom chain represents the system in a non-trivial topology where each complex fermion $\tilde{c}_j = \frac{1}{2}(a_j + ib_{j+1})$ is a linear combination of interconnected MFs, leaving the non-localized complex fermion $f = \frac{1}{2}(a_0 + ib_N)$, and thus leaving one MF located at each end of the chain.	9
97	1.2	The order phase φ and angle α of \mathbf{d} rotate by π : $(\varphi, \mathbf{d}) \rightarrow (\varphi + \pi, -\mathbf{d})$. The order parameter θ maps to itself, $(0, 2\pi)$, under simultaneous change of both \mathbf{d} and φ : $\theta = \varphi + \alpha$	11
100	1.3	Two vortices in an elementary braid exchange.	13
101	1.4	Braid group relation for $T_i T_{i+1} T_i = T_{i+1} T_i T_{i+1}$	14
102	1.5	Braiding two Majorana fermions on a T-junction.	15
103	1.6	Ladder junction schematic for hosting and braiding multiple Majorana fermions.	16
104	2.1	Schematics of two triangle structures proposed in this work. (a) Three-site Kitaev triangle with bond-dependent Peierls phases. (b) Hollow triangular island with a uniform vector potential.	30
107	2.2	(a) Evolution of the eigenvalues of the 3-site Kitaev triangle along the closed parameter path for ϕ on the three edges. (b) MZM wavefunctions at different points of the parameter path. Clockwise from the upper left panel: $\phi_1 \rightarrow \frac{1}{2}(\phi_1 + \phi_2) \rightarrow \phi_2 \rightarrow \phi_3$	32
110	2.3	(a) Schematic illustration of a finite-width ($W = 3$ here) ribbon based on the triangular lattice in the presence of a vector potential $\mathbf{A} = A(-\sin\varphi\hat{\mathbf{x}} + \cos\varphi\hat{\mathbf{y}})$. (b) Topological phase diagram for a $W = 1$ triangular chain obtained by superimposing the $\mathcal{M}_{b,t}(A, \mu)$ (b -bottom edge, t -top edges) plots of 1D chains with $\mathbf{A} = A\hat{\mathbf{y}}$ (bottom edge) and $\mathbf{A} = A(\frac{\sqrt{3}}{2}\hat{\mathbf{x}} + \frac{1}{2}\hat{\mathbf{y}})$ (top edges). Color scheme: black— $[\mathcal{M}_b, \mathcal{M}_t] = [1, 1]$, yellow— $[-1, -1]$, purple— $[-1, 1]$, orange— $[1, -1]$ (not present in this case) (b) Near-gap BdG eigen-energies vs A for a finite triangle with edge length $L = 50$, $W = 1$, and $\mu = 1.6$. $t = \Delta = 1$ in all calculations.	34
118	2.4	(a) Topological phase diagram for a $W = 1$ triangle by superimposing the $\mathcal{M}_{b,r,l}(A, \varphi)$ plots of 1D chains (b -bottom, r -right, l -left, $\mu = 1.1$). $\varphi_{r,l}$ are equal to $\varphi_b + \pi/3$ and $\varphi_b - \pi/3$, respectively. The colors are coded by which edges have non-trivial topology. For example, Black— $[\mathcal{M}_b, \mathcal{M}_r, \mathcal{M}_l] = [1, 1, 1]$ means all edges are trivial. The behavior depicted in panels (b-f) is representative of that when A is in the range of $(2.25, 2.5)$, for which the $\mathcal{M} = -1$ phase “crawls” through the three edges counter-clockwise as φ increases. (b) Spectral flow of a triangle with $W = 1$, $L = 50$, $\mu = 1.1$, and $A = 2.35$ with increasing φ . (c-f) BdG eigenfunction $ \Psi ^2$ summed over the two zero modes at $\varphi = 0, \frac{\pi}{12}, \frac{\pi}{6}$, and $\frac{\pi}{3}$, respectively. The bottom edge is parallel with $\hat{\mathbf{x}}$ in the coordinates illustrated in Fig. 2.3 (a).	35

128	2.5	Representative steps for braiding four MZM in four triangles sharing corners. (a)	
129		Initialization of four MZM $\gamma_1, \gamma_2, \gamma_3, \gamma_4$. All three edges of the bottom-middle and	
130		the top triangles are in the trivial phase by e.g. controlling the chemical potential.	
131		The bottom-left and bottom-right triangles have $\varphi = 0$ so that their bottom edges	
132		are nontrivial. (b) Moving γ_3 by “switching on” the middle triangle by changing the	
133		chemical potential under a fixed vector potential at $\varphi = \frac{\pi}{6}$, and then turning on the	
134		top triangle with similar means except $\varphi = 0$. (c) Transporting γ_2 to the right triangle	
135		through rotating the vector potential in the middle triangle counterclockwise by $\pi/6$.	
136		(d) Moving γ_3 to the left triangle by “switching off” the top triangle followed by the	
137		middle triangle.	37
138	2.6	(a) Topological phase diagram for a $W = 3$ hollow triangle obtained by overlapping	
139		the $\mathcal{M}_{b,t}(A, \mu)$ plots of 1D chains with $\mathbf{A} = A\hat{\mathbf{y}}$ and $\mathbf{A} = A(\frac{\sqrt{3}}{2}\hat{\mathbf{x}} + \frac{1}{2}\hat{\mathbf{y}})$. Color scheme:	
140		purple— $[\mathcal{M}_b, \mathcal{M}_t] = [1, 1]$, yellow— $[\mathcal{M}_b, \mathcal{M}_t] = [-1, -1]$, red— $[\mathcal{M}_b, \mathcal{M}_t] = [-1, 1]$, orange—	
141		$[\mathcal{M}_b, \mathcal{M}_t] = [1, -1]$ (b) Near-gap BdG eigen-energies vs A for a finite triangle with	
142		edge length $L = 80$, $W = 3$, and $\mu = 1.6$	47
143	2.7	(a) Topological phase diagram for three $W = 3$ ribbons corresponding to the three	
144		edges of a hollow triangle. ($\mu = 1.6$ in all panels.) (b) Minimum of the bulk gaps of the	
145		three ribbons plotted on the (A, φ) plane. (c) Spectral flow of a hollow triangle with	
146		$W = 3$, $L = 80$, and the parameter path given in Eq. (2.37). (d-g) BdG eigenfunction	
147		$ \Psi ^2$ summed over the two zero modes at $\varphi = 0, \frac{\pi}{6}, \frac{\pi}{3}, \frac{\pi}{2}$, respectively.	49
148	2.8	(a) Spectral flow for the critical step of swapping γ_2 and γ_3 in the example of Fig. 5	
149		in the main text, calculated using four corner-sharing triangles of $W = 1$ and $L = 50$,	
150		with $\mu = 1.6$ and $A = 2.6$. Vector potential for the middle triangle in the bottom row	
151		can rotate according to $\mathbf{A} = A(-\sin\varphi\hat{\mathbf{x}} + \cos\varphi\hat{\mathbf{y}})$ from $\varphi = \frac{\pi}{6}$ to $\frac{\pi}{3}$, while the other	
152		three have fixed $\varphi = 0$. (b)-(g) BdG eigenfunction $ \Psi ^2$ summed over the four zero	
153		modes at equally-spaced points along the rotation path. The black arrow indicates	
154		the direction of the vector potential for the bottom middle triangle.	50
155	3.1	Schematic of two oblique (forward and backward) and one normal incident light on	
156		graphene or a 2DEG substrate with high refractive index material on top. Oblique	
157		lasers have polarization in y -axis and travel in xz -plane and normal incidence laser	
158		has polarization in the x -axis and travel in yz -plane. With beam width large enough	
159		to cover the device fully.	53
160	3.2	Effective magnetic field (cyan) and first quasienergy (red) as a function of photon	
161		energy for various refractive materials: vacuum (triangles), germanium (squares),	
162		and Al-composite metamaterial (circles).	59
163	3.3	Effective magnetic field (cyan) and first quasienergy (red) as a function of photon en-	
164		ergy for 2DEGs for various refractive materials: vacuum (triangles) scaled by a factor	
165		of 50, germanium (squares) scaled by a factor of 10, and Al-composite metamateri-	
166		als. The 2DEG materials used are (a) GaAs and (b) InSb.	60
167	B.1	Unit cell for dirac system with gauge potential with translation symmetry in the $y -$	
168		$axis$ described by Eq. (B.81).	102

Chapter 1

Introduction

1.1 Maxwell's equations and gauge transformations

Here we give an overview of Maxwell's equations in relation to gauge potentials and transformations. The electric and magnetic fields, \mathbf{E} and \mathbf{B} , respectively, are physical observables. While differing potential fields V and \mathbf{A} are not directly observable, both give the same electric and magnetic fields. A gauge potential and its transformation are not physical and are reflected under gauge invariance. Introducing a gauge potential into a condensed matter system allows us to manipulate it. To do so, we start with Maxwell's equations and aim to rewrite them in terms of potential fields.

$$\nabla \cdot \mathbf{E} = \frac{1}{\epsilon_0} \rho, \quad (1.1)$$

$$\nabla \cdot \mathbf{B} = 0, \quad (1.2)$$

$$\nabla \times \mathbf{E} = -\partial_t \mathbf{B}, \quad (1.3)$$

$$\nabla \times \mathbf{B} = \mu_0 \mathbf{J} + \mu_0 \epsilon_0 \partial_t \mathbf{E}, . \quad (1.4)$$

One can write Maxwell's equations as a function of potentials, V and \mathbf{A} . Recall the magnetic field, $\mathbf{B} = \nabla \times \mathbf{A}$, and electric field, $\mathbf{E} = -\nabla V - \partial_t \mathbf{A}$. Eq. (1.1) and (1.4) provide the most information, which become

$$\frac{1}{\epsilon_0} \rho = -\nabla^2 V - \partial_t \nabla \cdot \mathbf{A}, \quad (1.5)$$

$$-\mu_0 \mathbf{J} = \nabla^2 \mathbf{A} - \mu_0 \epsilon_0 \partial_t^2 \mathbf{A} - \nabla (\nabla \cdot \mathbf{A} + \mu_0 \epsilon_0 \partial_t V). \quad (1.6)$$

179 We now transition to gauge transformations. Suppose $\mathbf{A}' = \mathbf{A} + \boldsymbol{\alpha}$ and $V' = V + \beta$. Both vector
 180 potentials give the same magnetic field,

$$\mathbf{B} = \nabla \times \mathbf{A} = \nabla \times \mathbf{A}' = \nabla \times (\mathbf{A} + \boldsymbol{\alpha}),$$

181 which leads to $\boldsymbol{\alpha} = \nabla \lambda$. The two potentials should also give the same electric field,

$$\mathbf{E} = -\nabla V - \partial_t \mathbf{A} = -\nabla V' - \partial_t \mathbf{A}',$$

then $\beta = -\partial_t \lambda + k(t)$ and

$$\mathbf{A}' = \mathbf{A} + \nabla \lambda \tag{1.7}$$

$$V' = V - \partial_t \lambda + k(t), \tag{1.8}$$

182 which is a general gauge transformation of potentials. A change in V and \mathbf{A} does not alter the
 183 electric and magnetic fields, i.e. they are gauge invariant, and are tuned to adjust the divergence
 184 of \mathbf{A} . This allows one to solve the scalar and vector potentials readily depending on the gauge
 185 [\[1\]](#).

186 1.2 Minimal coupling and Canonical momentum

187 With the gauge potentials and their invariance shown we next show how a gauge poten-
 188 tial couples to the momentum operator, also known as minimal coupling. This occurs when
 189 a charged particle is in a gauge potential field. Minimal coupling comes from the following
 190 substitution

$$-i\hbar\nabla \rightarrow -i\hbar\nabla - q\mathbf{A}, \tag{1.9}$$

191 which can be derived from the canonical momentum operator when a charged particle is present
 192 in a gauge potential. In this case, minimal coupling means the field is coupling the orbital and

193 potential only, ignoring higher order multipole moments. This also allows the system to have a
 194 local gauge invariance under U(1) transformations, i.e. $\mathbf{A} \rightarrow \mathbf{A} + \nabla\lambda$ [2].

195 Next, we derive the canonical momentum operator and demonstrate its gauge invariance.

196 Starting with the Lagrangian for charged particle in a scalar and gauge potential,

$$\begin{aligned}\mathcal{L} &= T - U \\ \mathcal{L} &= \frac{1}{2}m\dot{\mathbf{r}}^2 - qV + q\dot{\mathbf{r}} \cdot \mathbf{A}(\mathbf{r}, t),\end{aligned}\tag{1.10}$$

197 where $T = \frac{1}{2}m\dot{\mathbf{r}}^2$ and $U = qV - q\dot{\mathbf{r}} \cdot \mathbf{A}(\mathbf{r}, t)$. Recall from classical mechanics that

$$\begin{aligned}\mathbf{p}_{\text{can}} &= \frac{\partial \mathcal{L}}{\partial \dot{\mathbf{r}}} \\ \mathbf{p}_{\text{can}} &= \mathbf{p}_{\text{kin}} + q\mathbf{A}.\end{aligned}\tag{1.11}$$

198 With the canonical momentum defined, the Hamiltonian is

$$\begin{aligned}\mathcal{H} &= \mathbf{p}_{\text{can}} \cdot \dot{\mathbf{r}} - \mathcal{L} \\ \mathcal{H} &= \frac{1}{2m}(\mathbf{p}_{\text{can}} - q\mathbf{A})^2 + qV.\end{aligned}\tag{1.12}$$

199 Thus, a charged particle in the presence of a gauge potential has the following minimal cou-
 200 pling, $i\hbar\nabla - q\mathbf{A}$.

201 Just as before for electric and magnetic fields, we will show the Hamiltonian is gauge in-
 202 variant. It can be shown with a scalar potential in the Hamiltonian, but we do not since it is
 203 irrelevant for our purposes. Suppose $\mathcal{H}|\psi\rangle = \epsilon|\psi\rangle$ and $\mathbf{A}' = \mathbf{A} + \nabla\lambda$, then the Hamiltonian acting
 204 on the wavevector is

$$\mathcal{H}|\psi\rangle = \frac{1}{2m}(\hat{\mathbf{p}} - q\mathbf{A}' + q\nabla\lambda)^2|\psi\rangle = \epsilon|\psi\rangle. \quad (1.13)$$

205 We assert

$$\mathcal{H}'|\psi'\rangle = \frac{1}{2m}(\hat{\mathbf{p}} - q\mathbf{A} - q\nabla\lambda)^2|\psi'\rangle = \epsilon|\psi'\rangle. \quad (1.14)$$

206 Let $|\psi'\rangle = U|\psi\rangle$, where U is a unitary operator such that $U^\dagger U = \hat{\mathbf{1}}$. Position and momentum ex-
 207 pectation values should be the same under both gauge choices. Starting with position operator
 208 we have

$$\langle\psi'|\hat{\mathbf{r}}|\psi'\rangle = \langle\psi|U^\dagger\hat{\mathbf{r}}U|\psi\rangle = \langle\psi|\hat{\mathbf{r}}|\psi\rangle \quad (1.15)$$

209 which gives the following useful commutation relation is $[\hat{\mathbf{r}}, U] = 0$, which can be extrapolated
 210 to $[\mathbf{A}(\mathbf{r}), U] = 0$. With the momentum operator we find

$$\langle\psi'|\hat{\mathbf{p}} - q\mathbf{A}'|\psi'\rangle = \langle\psi|U^\dagger(\hat{\mathbf{p}} - q\mathbf{A}')U|\psi\rangle = \langle\psi|\hat{\mathbf{p}} - q\mathbf{A}|\psi\rangle \quad (1.16)$$

211 that gives the following commutation relation $[\hat{\mathbf{p}}, U] = -i\hbar\partial_{\hat{\mathbf{r}}}U = q\nabla\lambda U$. This leads us to find
 212 $U = \exp[iq\lambda/\hbar]$. The gauged Hamiltonian is related to the original basis by

$$\mathcal{H}'|\psi'\rangle = U\epsilon|\psi\rangle. \quad (1.17)$$

213 We see the local phase of the wavefunction is changed but it still represents the same energy
 214 shown by

$$\langle \psi' | \mathcal{H}' | \psi' \rangle = \langle \psi | U^\dagger U \epsilon | \psi \rangle = \epsilon,$$

$$\langle \psi | \mathcal{H} | \psi \rangle = \langle \psi | \epsilon | \psi \rangle = \epsilon. \quad (1.18)$$

215 In other words $U^\dagger \mathcal{H}' U = \mathcal{H}$ [3].

216 1.3 Peierls phase in tight-binding models

217 When working with condensed matter systems we often either work with free particles us-
 218 ing Schrodinger's or Dirac's equation or tight-binding models describing how much energy is
 219 needed for a particle to "hop" from one lattice to the next. In tight-binding models there is typi-
 220 cally no momentum term to use minimal coupling to introduce the gauge potential, but we can
 221 find a basis transformation that is equivalent. There are a few different names this can go by,
 222 Aharonov-Bohm effect, Berry phase, geometric phase, or Peierls phase. There are a few ways
 223 to derive Peierls phase and we will use the differential geometry approach. Before, we showed
 224 minimal coupling and now we would like to express it in terms of a covariant derivative

$$D_\mu = \partial_\mu - i A_\mu. \quad (1.19)$$

225 Let us now envision how a wavefunction will evolve in the presence of a gauge potential field.
 226 Using the covariant derivative with parallel transport along curves we can obtain an expression
 227 for the phase accumulation on the wave function. The covariant derivative should vanish if it
 228 has been parallel transported along the curve \mathcal{C} defined by points x and $x' = x + v t$. The expres-
 229 sion is as follows $\nabla_\nu s \rightarrow t v^\mu D_\mu s_{x(t)} = 0$. This turns out to be a first order ordinary differential
 230 equation

$$\dot{s}_{x(t)} - i \dot{x}^\mu(t) A_{x(t),\mu} s_{x(t)} = 0$$

231 with the following solution

$$s_{x(t)} = s_{x(0)} \exp \left[i \int_{\mathcal{C}} dx^\mu A_{x(t'),\mu} \right] \quad (1.20)$$

and in general rewrite it as the following expression $\psi(t) = \psi(0) \exp \left[\frac{iq}{\hbar} \int_{\mathcal{C}} \mathbf{A}(\mathbf{r}) \cdot d\mathbf{l} \right]$ [2].

Given the following tight-binding Hamiltonian

$$\mathcal{H}_t = -t \sum_{\langle j,l \rangle} c_j^\dagger c_l + h.c., \quad (1.21)$$

a gauge potential is applied to the system making the following Peierls phase transform, a unitary transform, to its creation/annihilation operators

$$c_j^\dagger c_l \rightarrow c_j^\dagger c_l \exp \left[\frac{iq}{\hbar} \int_{\mathbf{r}_j}^{\mathbf{r}_l} \mathbf{A} \cdot d\mathbf{l} \right]. \quad (1.22)$$

The Hamiltonian in the new basis takes the following form

$$\mathcal{H}_t = \sum_{\langle j,l \rangle} -t_{j,l} c_j^\dagger c_l + h.c., \quad (1.23)$$

where $t_{j,l} = t \exp \left[\frac{iq}{\hbar} \int_{\mathbf{r}_j}^{\mathbf{r}_l} \mathbf{A} \cdot d\mathbf{l} \right]$.

1.4 Majorana fermions and topological superconductors

We discuss here Majorana fermions and their connection to topological superconductors and the properties that can be exploited for topological quantum computing. There are three types of fermions: Dirac, Weyl, Majorana. Fermions are particles that follow Fermi-Dirac statistics and the Pauli exclusion principle and have half-integer spin (spin 1/2, 3/2, etc.). In 1926, both Enrico Fermi and Paul Dirac derived Fermi-Dirac statistics, independently of one another. Dirac's equation led to the derivation of a (complex) wavefunction solution for spin-half fermions that have mass and charge, and an antiparticle, coined as the positron. A few years later, Hermann Weyl derived from Dirac's equation a simplified solution for describing massless

fermions. Then, in 1937 Ettore Majorana hypothesized from Dirac's equation a (real) wavefunction solution that showed that these fermions were both particle and antiparticle and neutrally charged.

Examples of observed fermions include electrons, neutrinos, neutrons, and protons. The Standard Model does allow for neutrinos to potentially be Majorana fermions. The MAJORANA project: neutrinoless double beta decay, is one experiment for detecting neutrino Majorana fermions and has yielded negative results thus far. The particle physics community has yet to find either Weyl or Majorana fermions in experiments. There are, however, avenues for pursuing them as quasiparticles in condensed matter systems. For example, in 2011 Weyl fermions were theorized to be in topological semimetals then quickly observed as quasiparticles by 2015 in TaAs semimetals using angle-resolved photoemission spectroscopy (ARPES) [4–6].

Since 2001 it has been hypothesized that Majorana fermions can be found on p -wave superconductors in pairs of 2 and non-localized in half-quantum vortices and at the ends of wires [7, 8]. In conventional superconductors there are Cooper pairs that make up the supercurrent. These Cooper pairs are made up of two electrons (or holes) with opposite spin and momenta caused by the electron-phonon interaction, are bosonic and condensate, and are in a ground state with allowed excited states.

A Bogoliubov quasiparticle is the first excited state of a Cooper pair condensate, this is when an electron and hole with opposite momenta become paired. This usually happens when the systems chemical potential allows the electron and hole bands to cross one another in the Brillouin space and the superconducting order parameter, Δ , dictates the type of spin coupling. For example, superconductors that are s -wave pair electrons and holes with opposite spin, while p -wave pairs electrons and holes that are spin-polarized. In a p -wave superconductor if the Bogoliubov quasiparticle is a zero-energy excitation it can be written as a Majorana fermion and because of the particle-hole symmetry in the system they come in pairs.

We have yet to physically realize a p -wave superconductor experimentally, however, we can use heterostructures in proximity to an s -wave superconductor to achieve an effective p -

wave superconducting interface, which is explained and referenced in later chapters. Majorana fermions are dictated by non-Abelian exchange statistics, which allows for building a universal quantum computer, hence why they are highly sought after. Another boon of using a non-trivial topological superconductor is the ability to protect Majorana fermions from local perturbations.

1.4.1 Kitaev chain

Ivanov first showed how to derive Majorana fermions in a 2D p -wave superconductor. However, we find it easier to understand Kitaev's approach first. Let us go ahead and show how Kitaev derived Majorana zero modes (MZMs), Majorana(MFs), on a 1D spinless p -wave superconductor. Start with a 1D spinless p -wave superconductor tight-binding Hamiltonian

$$\mathcal{H} = \sum_j^{N-1} (-tc_j^\dagger c_{j+1} + \Delta c_j c_{j+1} + h.c.) - \sum_j^N \mu c_j^\dagger c_j, \quad (1.24)$$

where t is hopping amplitude, $\Delta = |\Delta|$ is the superconducting order parameter, μ is chemical potential, and $c^\dagger(c)$ is the creation (annihilation) operator for a complex fermion. We use a basis transformation to convert to the Majorana fermion basis, where $c_j^\dagger = \frac{1}{2}(a_j - ib_j)$, $\{a_j^\dagger, a_{j'}\} = \{a_j, a_{j'}\} = 2\delta_{j,j'}$ since they are Majorana fermions, and $\{a_j, b_j'\} = 0$. The Hamiltonian becomes

$$\mathcal{H} = \frac{i}{2} \sum_j (-\mu a_j b_j + (t + \Delta) b_j a_{j+1} + (-t + \Delta) a_j b_{j+1}). \quad (1.25)$$

In the trivial topology phase, there are no Majorana fermions, $\mu \neq 0$ and $t = \Delta = 0$,

$$\mathcal{H} = -\mu \frac{1}{2} \sum_j a_j b_j. \quad (1.26)$$

For non-trivial topology phase, there are Majorana fermions present, $\mu = 0$, and $t = \Delta > 0$,

$$\mathcal{H} = it \sum_j b_j a_{j+1}. \quad (1.27)$$

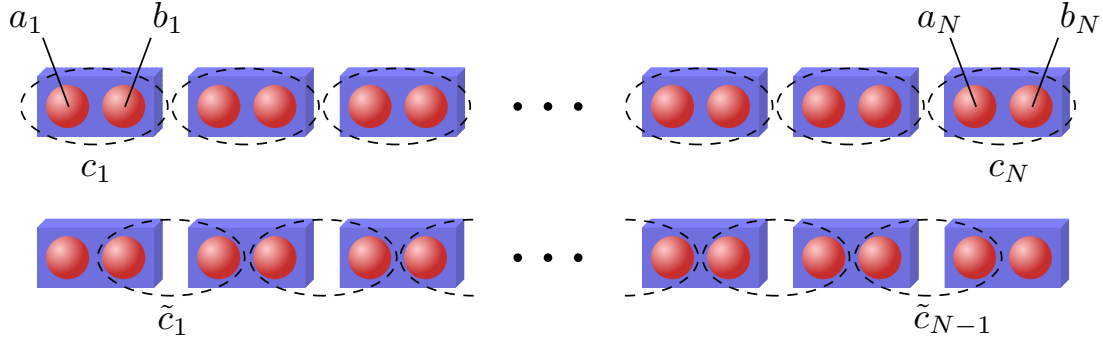


Figure 1.1: The top chain represents the system in a trivial topology where each complex fermion $c_j = \frac{1}{2}(a_j + i b_j)$ is a linear combination of intraconnected MFs. The bottom chain represents the system in a non-trivial topology where each complex fermion $\tilde{c}_j = \frac{1}{2}(a_j + i b_{j+1})$ is a linear combination of interconnected MFs, leaving the non-localized complex fermion $f = \frac{1}{2}(a_0 + i b_N)$, and thus leaving one MF located at each end of the chain.

Notice terms a_0 and b_N are missing in the non-trivial topology Hamiltonian, we can state there is a non-localized zero energy mode present in the system defined by $f = \frac{1}{2}(a_0 + i b_N)$, hence the name Majorana zero modes. Figure 1.1 shows the wire in both topological phases.

A quick note on terminology, sometimes non-trivial topology is referred to as the topological phase, for the purposes of this dissertation we will use the former option. Slightly outside the Kitaev limit, for non-trivial topology to persist, $|\mu| < 2t$ and $t = |\Delta| > 0$. Majorana zero modes are hosted at the interface of trivial and non-trivial topology due to bulk-edge correspondence.

To prove this, calculate the topological invariant for the system, also known as the Majorana number, a type of Winding number for 1D superconducting systems. While calculating the Majorana number is straight forward enough, its proof on the other hand is not, this can be found in App. A.1. Perform Majorana basis transformation on the Hamiltonian, $A = -iU\mathcal{H}U^\dagger$, then take the sign of the Pfaffian,

$$\mathcal{M} = \text{sgn}[\text{Pf}(A)]. \quad (1.28)$$

This calculation can be reduced down if we can write the Hamiltonian in momentum space. Employing the following symmetry $\epsilon(-k) = -\epsilon(k)$ we find there are n positive and n negative eigenvalues in the system for any given k value.

$$\mathcal{M} = \begin{cases} \text{sgn}[\text{Pf}(A_{k=0})\text{Pf}(A_{k=\pi})], & \text{if } L \text{ is even,} \\ \text{sgn}[\text{Pf}(A_{k=0})], & \text{if } L \text{ is odd,} \end{cases} \quad (1.29)$$

where L is the number of lattice sites from our lattice Hamiltonian. We find that under the Kitaev limit, if $|\mu| < 2t$, then $\mathcal{M} = -1$, and if $|\mu| > 2t$, then $\mathcal{M} = 1$. When a section of the material is in a non-trivial topology and either the other material is trivial or vacuum, which is also trivial, Majorana zero modes will be localized at interfaces of differing topological number, this is also known as bulk-edge correspondence and will be used later in our topological quantum logic gate. As a last note, when $|\mu| = 2t$ this is a critical point and where the gap opens and closes, it is not an ideal region of parameter space for the band gap is too small. Originally, Kitaev's proposal was to design topological quantum storage [8].

1.4.2 Half-quantum vortices in p -wave superconductors

We now transition back to Ivanov's derivation of MFs and begin to introduce *braiding* for topological quantum computing as a key reason for hosting and manipulating MFs. It was proposed by Read and Green that the Pfaffian quantum Hall state derived by Moore and Read belongs to the same topological class as the BCS pairing state. Ivanov then verified this was the case for a BCS pairing state. Since the Pfaffian state was shown to exhibit non-Abelian statistics for half-quantum vortices the same is true for p -wave superconductors. To answer why this is the case we need to understand how the superconducting order parameter acts for different pairing potentials composing of singlet or triplet states [7].

The superconducting order parameter, called order parameter or pairing potential for short, tells us the correlation between two fermionic operators in a superconductor and thus requires the state to be antisymmetric. These states are made up of a spatial and spin component. When the two electrons in a Cooper pair are a spin-singlet the spin component is antisymmetric and requires the spatial component be symmetric; this occurs in s - and d -wave superconductors. If instead the electrons in a Cooper pair are a spin-triplet the spin component is symmetric and

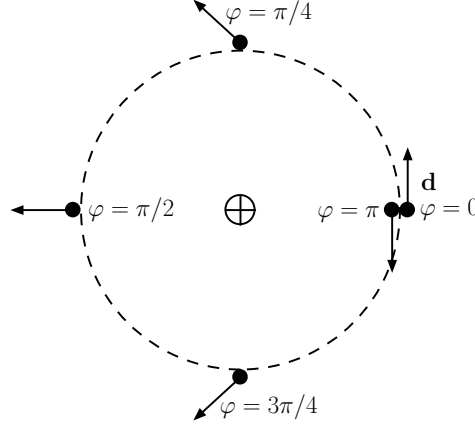


Figure 1.2: The order phase φ and angle α of \mathbf{d} rotate by π : $(\varphi, \mathbf{d}) \rightarrow (\varphi + \pi, -\mathbf{d})$. The order parameter θ maps to itself, $(0, 2\pi)$, under simultaneous change of both \mathbf{d} and φ : $\theta = \varphi + \alpha$.

requires the spatial component by antisymmetric; this occurs in p - and f -wave superconductors. In terms of Pauli matrices we can in general encode the order parameter with

$$\Delta(\mathbf{k}) = (\Delta_0(\mathbf{k}) + \mathbf{d}(\mathbf{k}) \cdot \boldsymbol{\sigma}) i\sigma_y, \quad (1.30)$$

with the following antisymmetric definition $\Delta(\mathbf{k}) = \Delta^T(-\mathbf{k})$, we see $\Delta_0(\mathbf{k})$ encodes spin-singlet components and $\mathbf{d}(\mathbf{k})$ encodes spin-triplet components, and at the end σ_y is there to keep the matrix antisymmetric. The direction vector \mathbf{d} needs to be a three dimensional vector to ensure we account for the three spin configurations $|\uparrow\uparrow\rangle$, $|\uparrow\downarrow\rangle + |\downarrow\uparrow\rangle$, and $|\downarrow\downarrow\rangle$. To account for even-parity in the symmetric spatial component, the momentum is of even powers proportional with the even spherical harmonics. While odd-parity in the antisymmetric component, the momentum is of odd powers proportional to the odd spherical harmonics. For example, in s -wave superconductors, $l = 0$ and $Y_{0,0} = \text{const.}$ and has no momentum dependence and $\Delta_s(\mathbf{k}) = i\Delta_0\sigma_y$. In the case of p -wave superconductors, $l = 1$ and $Y_{1,\pm 1} \propto k_x \pm ik_y$ leading to linear dependence in momentum such that the order parameter becomes $\Delta_p(\mathbf{k}) = i\Delta(\mathbf{d} \cdot \boldsymbol{\sigma})(k_x + ik_y)\sigma_y$ [7].

In Ivanov's case he picked a slightly different basis for the triplet-pairing order parameter,

$$\Delta(\mathbf{k}) = \Delta e^{i\varphi} [d_x \sigma_0 + i d_y \sigma_z + d_z \sigma_x] (k_x + i k_y) \quad (1.31)$$

it still follows the antisymmetric definition $\Delta(\mathbf{k}) = -\Delta^T(-\mathbf{k})$. For a half-quantum vortex to exist, we must allow \mathbf{d} to rotate in 3D or in a plane. Additionally, the order parameter maps to itself, which requires the change of sign of \mathbf{d} and shift in the phase φ by π simultaneously. This mapping is $(\varphi, \mathbf{d}) \mapsto (\varphi + \pi, -\mathbf{d})$ and can be seen in Figure 1.2 [7].

We now reduce to a 2D superconductor, this forces \mathbf{d} to point and rotate in the x-y plane and removes the coupling of spin-up and -down fermions from the order parameter. The order parameter can then be written in polar coordinates

$$\begin{aligned} \Delta(\mathbf{k}, r, \theta) &= \Delta(r) e^{i\varphi} \begin{bmatrix} e^{i\alpha} & 0 \\ 0 & e^{-i\alpha} \end{bmatrix} (k_x + i k_y) \\ &= \Delta(r) \begin{bmatrix} e^{i\theta} & 0 \\ 0 & 1 \end{bmatrix} (k_x + i k_y), \end{aligned} \quad (1.32)$$

where α is the angle of \mathbf{d} , remembering its simultaneous change w.r.t. φ . We see that the spin-up fermions have a vortex while the spin-down do not have a vortex (and thus no low energy states). The Hamiltonian for spin-up or spinful fermions can now be described by

$$\mathcal{H} = \int d^2\mathbf{r} \left[-\Psi^\dagger \left(\frac{\nabla^2}{2m} + \epsilon_F \right) \Psi + \Psi^\dagger \left[e^{i\theta} \Delta(r) * (\partial_x + i\partial_y) \right] \Psi^\dagger + h.c. \right], \quad (1.33)$$

where $*$ is the symmetrized product $[A * B = (AB + BA)/2]$. One can diagonalize the Hamiltonian using the quasiparticle operator $\gamma^\dagger = u\Psi^\dagger + v\Psi$. The creation annihilation of the same fermion is related by the parameters u and v , causing the energy eigenstates to be symmetric about zero-energy forcing $\gamma^\dagger(E) = \gamma(E)$. It then leads to the zero-energy eigenstate being self-conjugate, a Majorana fermion, $\gamma^\dagger(E=0) = \gamma(E=0)$. The spinful nature eliminates the spin degree of free-

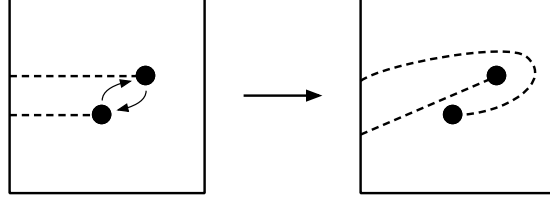


Figure 1.3: Two vortices in an elementary braid exchange.

dom and shows the creation and annihilation operators are coupled due to superconductivity, making the Majorana fermion possible through self-conjugacy [7].

1.4.3 Braiding

To speak on braiding it is important to start with gauge symmetry. Under $U(1)$ gauge transformation, if the superconducting gap is shifted by ϕ , it is the same as rotating the creation annihilation operator by half the shift. Thus, $\Psi_\alpha \mapsto e^{i\phi/2}\Psi_\alpha$, which leads to the Majorana fermion operator weights transforming as $(u, v) \mapsto (ue^{i\phi/2}, v^{-i\phi/2})$. We can see with a change of superconducting order parameter by 2π the Majorana fermion changes sign, $\gamma \mapsto -\gamma$ [7].

This change of sign is important in braiding transformations since it allows for non-Abelian statistics. We can circumvent a global phase by introducing branch cuts for the vortices to cross, causing a 2π phase change in the Majorana fermion. Vortices can be exchanged as described in Figure 1.3, with a "bird's eye" view. We can define the braiding operators as the following

$$T_i : \begin{cases} \gamma_i \mapsto \gamma_{i+1} \\ \gamma_{i+1} \mapsto -\gamma_i \\ \gamma_j \mapsto \gamma_j \quad \text{for } j \neq i \text{ and } j \neq i+1. \end{cases} \quad (1.34)$$

This leads to the following braiding relations

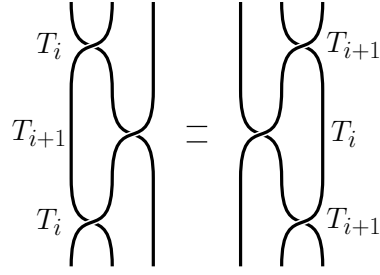


Figure 1.4: Braid group relation for $T_i T_{i+1} T_i = T_{i+1} T_i T_{i+1}$.

$$T_i T_j = T_j T_i, \quad |i - j| > 1, \quad (1.35)$$

$$T_i T_j T_i = T_j T_i T_j, \quad |i - j| = 1.$$

Figure 1.4 demonstrates three neighboring vortices with braiding statistics having two means of achieving the same braiding exchange. One can write the braiding operators in terms of fermionic operators with the following

$$\tau(T_i) = \exp\left(\frac{\pi}{4} \gamma_{i+1} \gamma_i\right) = \frac{1}{\sqrt{2}} (1 + \gamma_{i+1} \gamma_i). \quad (1.36)$$

This can be further carried out for any number of Majorana fermions and builds a set of braiding operators for that system [7].

1.4.4 T-junction qubit

The simplest qubit theorized for braiding Majorana fermions is on 1D wires connected in a T-junction, which can be extrapolated to a ladder junction for $2n$ Majorana fermions. In the T-junction we define the quasi-1D Hamiltonian

$$\mathcal{H} = -\mu \sum_j c_j^\dagger c_j - \sum_j \left(t c_j^\dagger c_{j+1} + |\Delta| e^{i\phi} c_j c_{j+1} + h.c. \right), \quad (1.37)$$

where $c_j = e^{-i\phi/2} (\gamma_{j+1,1} + i\gamma_{j,2})/2$. We additionally have to define the pairing as $|\Delta| e^{i\phi} c_j c_{j+1}$ such that the site indices have the following definitions

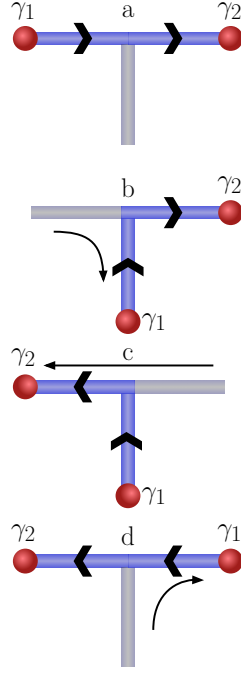


Figure 1.5: Braiding two Majorana fermions on a T-junction.

- Increase moving \rightarrow / \uparrow in the horizontal/vertical wires: $\phi = 0$,
- Decrease moving \leftarrow / \downarrow in the horizontal/vertical wires: $\phi = \pi$.

The braiding of two Majorana fermions in a T-junction is achieved by adiabatically tuning the voltage gate, or chemical potential, of the wires which can be seen in Figure 1.5. Then, extrapolate to a ladder junction as shown in Figure 1.6 [9]. While this approach is simple in theory and being seriously pursued, it is difficult to build, manipulate, and read experimentally. Another difficulty for these wires is due to not having any truly p -wave superconductors, currently they need to be built from heterostructures to make an effective p -wave superconductor.

1.4.5 Effective p -wave superconductors

There are several ways to build an effective p -wave superconductor. One example is given by Sau et. al. [10] where a zinc-blende semiconductor quantum well grown along the (100) direction is considered. We start with the relevant non-interacting Hamiltonian

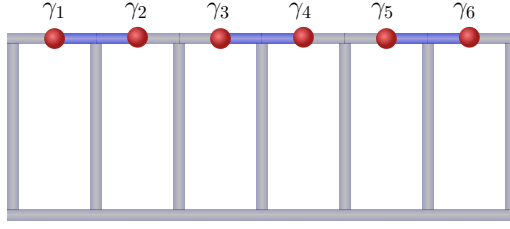


Figure 1.6: Ladder junction schematic for hosting and braiding multiple Majorana fermions.

$$\mathcal{H}_0 = \sum_{\mathbf{k}} c_{\mathbf{k}}^\dagger \left[\frac{\hbar^2 k^2}{2m} - \mu + \alpha(\sigma^x k_y - \sigma^y k_x) \right] c_{\mathbf{k}} \quad (1.38)$$

where m is the effective mass, μ is the chemical potential, α is the Rashba spin-orbit coupling strength, and σ^i are the Pauli matrices that act on the spin degrees of freedom in $c_{\mathbf{k}}$, and $\hbar = 1$ throughout.

Next, introduce a ferromagnetic insulator to induce a Zeeman effect. The ferromagnetic insulator has magnetization pointing perpendicular to the 2D semiconductor with energy

$$\mathcal{H}_Z = V_z \sum_{\mathbf{k}} c_{\mathbf{k}}^\dagger \sigma^z c_{\mathbf{k}} \quad (1.39)$$

but negligible orbital coupling. One can build an eigenbasis from the combined Hamiltonian with the following eigenenergies $\epsilon'_\pm(\mathbf{k}) = \pm \sqrt{V_z^2 + \alpha^2 k^2}$ with eigenvectors

$$u_+(\mathbf{k}) = \begin{pmatrix} A_\uparrow(\mathbf{k}) \\ -A_\downarrow(\mathbf{k}) \frac{k_y - i k_x}{k} \end{pmatrix}, \quad (1.40)$$

$$(1.41)$$

$$u_-(\mathbf{k}) = \begin{pmatrix} B_\uparrow(\mathbf{k}) \frac{k_y + i k_x}{k} \\ B_\downarrow(\mathbf{k}) \end{pmatrix}. \quad (1.42)$$

399 Where $A_\sigma = A_\sigma^*$ and $B_\sigma = B_\sigma^*$ and the coefficients are

$$A_\uparrow(\mathbf{k}) = \frac{-\alpha k}{\sqrt{2\epsilon'_+(\mathbf{k})}} \sqrt{\frac{1}{\epsilon'_+(\mathbf{k}) - V_z}} \quad (1.43)$$

$$A_\downarrow(\mathbf{k}) = \sqrt{\frac{\epsilon'_+(\mathbf{k}) - V_z}{2\epsilon'_+(\mathbf{k})}} \quad (1.44)$$

$$B_\uparrow(\mathbf{k}) = \sqrt{\frac{\epsilon'_-(\mathbf{k}) + V_z}{2\epsilon'_-(\mathbf{k})}} \quad (1.45)$$

$$B_\downarrow(\mathbf{k}) = \frac{\alpha k}{\sqrt{2\epsilon'_-(\mathbf{k})}} \sqrt{\frac{1}{\epsilon'_-(\mathbf{k}) + V_z}}. \quad (1.46)$$

400 The expressions for $A_{\uparrow,\downarrow}$ and $B_{\uparrow,\downarrow}$ can be written as

$$f_p(\mathbf{k}) = A_\uparrow(\mathbf{k}) A_\downarrow(-\mathbf{k}) = B_\uparrow(-\mathbf{k}) B_\downarrow(\mathbf{k}) \quad (1.47)$$

$$= \frac{-\alpha k}{2\epsilon'_+(\mathbf{k})}. \quad (1.48)$$

401 With the semiconductor in contact with an s -wave superconductor, a pairing term is gener-
 402 ated by the proximity effect. The full Hamiltonian becomes $\mathcal{H} = \mathcal{H}_0 + \mathcal{H}_Z + \mathcal{H}_{SC}$ with

$$\mathcal{H}_{SC} = \sum_{\mathbf{k}} \Delta c_{\uparrow,\mathbf{k}}^\dagger c_{\downarrow,-\mathbf{k}}^\dagger + H.c. \quad (1.49)$$

403 Write the pairing potential in terms of c_\pm using a basis transformation,

$$c_{\uparrow,\mathbf{k}} = \langle \uparrow | u_+(\mathbf{k}) \rangle c_{\mathbf{k},+} + \langle \uparrow | u_-(\mathbf{k}) \rangle c_{\mathbf{k},-} \quad (1.50)$$

$$= A_{\uparrow}(\mathbf{k}) c_{\mathbf{k},+} + B_{\uparrow}(\mathbf{k}) \frac{k_y + i k_x}{k} c_{\mathbf{k},-}, \quad (1.51)$$

$$c_{\downarrow,-\mathbf{k}} = \langle \downarrow | u_+(-\mathbf{k}) \rangle c_{-\mathbf{k},+} + \langle \downarrow | u_-(-\mathbf{k}) \rangle c_{-\mathbf{k},-} \quad (1.52)$$

$$= A_{\downarrow}(-\mathbf{k}) \frac{k_y - i k_x}{k} c_{-\mathbf{k},+} + B_{\downarrow}(-\mathbf{k}) c_{-\mathbf{k},-} \quad (1.53)$$

404 with the adjoints being

$$c_{\uparrow,\mathbf{k}}^{\dagger} = A_{\uparrow}(\mathbf{k}) c_{\mathbf{k},+}^{\dagger} + B_{\uparrow}(\mathbf{k}) \frac{k_y - i k_x}{k} c_{\mathbf{k},-}^{\dagger} \quad (1.54)$$

$$c_{\downarrow,-\mathbf{k}}^{\dagger} = A_{\downarrow}(-\mathbf{k}) \frac{k_y + i k_x}{k} c_{-\mathbf{k},+}^{\dagger} + B_{\downarrow}(-\mathbf{k}) c_{-\mathbf{k},-}^{\dagger}. \quad (1.55)$$

405 Reducing the pairing potential further becomes

$$\begin{aligned} \Delta c_{\uparrow,\mathbf{k}}^{\dagger} c_{\downarrow,-\mathbf{k}}^{\dagger} &= \Delta [A_{\uparrow}(\mathbf{k}) A_{\downarrow}(-\mathbf{k}) \frac{k_y + i k_x}{k} c_{\mathbf{k},+}^{\dagger} c_{-\mathbf{k},+}^{\dagger} + B_{\uparrow}(\mathbf{k}) B_{\downarrow}(-\mathbf{k}) \frac{k_y - i k_x}{k} c_{\mathbf{k},-}^{\dagger} c_{-\mathbf{k},-}^{\dagger} \\ &\quad + (A_{\uparrow}(\mathbf{k}) B_{\downarrow}(-\mathbf{k}) + B_{\uparrow}(\mathbf{k}) A_{\downarrow}(-\mathbf{k})) c_{\mathbf{k},+}^{\dagger} c_{-\mathbf{k},-}^{\dagger}]. \end{aligned} \quad (1.56)$$

406 We make the following substitutions

$$\Delta_{++}(\mathbf{k}) = \Delta f_p(\mathbf{k}) \frac{k_y + i k_x}{k} \quad (1.57)$$

$$\Delta_{--}(\mathbf{k}) = \Delta f_p(-\mathbf{k}) \frac{k_y - i k_x}{k} \quad (1.58)$$

$$\Delta_{+-}(\mathbf{k}) = \Delta f_s(\mathbf{k}), \quad (1.59)$$

407 where

$$f_s(\mathbf{k}) = (A_{\uparrow}(\mathbf{k})B_{\downarrow}(-\mathbf{k}) + B_{\uparrow}(\mathbf{k})A_{\downarrow}(-\mathbf{k})). \quad (1.60)$$

408 The pairing potential Hamiltonian then becomes

$$\mathcal{H}_{SC} = \sum_{\mathbf{k}} \Delta_{++} c_{\mathbf{k},+}^{\dagger} c_{-\mathbf{k},+}^{\dagger} + \Delta_{--} c_{\mathbf{k},-}^{\dagger} c_{-\mathbf{k},-}^{\dagger} + \Delta_{+-} c_{\mathbf{k},+}^{\dagger} c_{-\mathbf{k},-}^{\dagger} + h.c. \quad (1.61)$$

409 Writing the full Hamiltonian in matrix form we will use the following Nambu spinor

$$\Psi = (c_{\mathbf{k},+}, c_{\mathbf{k},-}, c_{-\mathbf{k},+}^{\dagger}, c_{-\mathbf{k},-}^{\dagger})^T. \quad (1.62)$$

410 Then, write the Hamiltonian using the conventional BdG approach of applying the anti-
411 commutation relation and reindexing the momentum vector of the second term to give

$$\mathcal{H} = \frac{1}{2} \sum_{\mathbf{k}} \Psi^{\dagger} H_{BdG} \Psi \quad (1.63)$$

412 with

$$H_{BdG} = \begin{bmatrix} \epsilon_{+}(\mathbf{k}) & 0 & 2\Delta_{++}(\mathbf{k}) & \Delta_{+-}(\mathbf{k}) \\ 0 & \epsilon_{-}(\mathbf{k}) & -\Delta_{+-}(-\mathbf{k}) & 2\Delta_{--}(\mathbf{k}) \\ 2\Delta_{++}^{*}(\mathbf{k}) & -\Delta_{+-}^{*}(-\mathbf{k}) & -\epsilon_{+}(-\mathbf{k}) & 0 \\ \Delta_{+-}^{*}(\mathbf{k}) & 2\Delta_{--}^{*}(\mathbf{k}) & 0 & -\epsilon_{-}(-\mathbf{k}) \end{bmatrix}, \quad (1.64)$$

413 where

$$\epsilon_{\pm}(\mathbf{k}) = \frac{k^2}{2m} - \mu + \epsilon'_{\pm}(\mathbf{k}). \quad (1.65)$$

414 Rearranging the matrix into a more block diagonal form of $(++)$ and $(--)$ gives

$$H_{BdG} = \begin{bmatrix} \epsilon_+(\mathbf{k}) & 2\Delta_{++} & 0 & \Delta_{+-}(\mathbf{k}) \\ 2\Delta_{++}^* & -\epsilon_+(-\mathbf{k}) & -\Delta_{+-}^*(-\mathbf{k}) & 0 \\ 0 & -\Delta_{+-}(-\mathbf{k}) & \epsilon_-(\mathbf{k}) & 2\Delta_{--} \\ \Delta_{+-}^*(\mathbf{k}) & 0 & 2\Delta_{--}^* & -\epsilon_-(-\mathbf{k}) \end{bmatrix}. \quad (1.66)$$

415 Upon studying $V_z \gg \alpha$, near the fermi surface the interband pairing has little affect on the band
 416 gap. Scaling it's effect from $0 \rightarrow 1$ the intraband gap appears at a slightly smaller momentum as
 417 the interband pairing is turned off. We use the approximation $\Delta_{+-}(k_f) \approx 0$ and set μ such that
 418 it only crosses the lower bands, allowing $c_+^\dagger \rightarrow 0$, leaving

$$H_{BdG} = \begin{bmatrix} \epsilon_-(\mathbf{k}) & 2\Delta_{--}(\mathbf{k}) \\ 2\Delta_{--}^*(\mathbf{k}) & -\epsilon_-(-\mathbf{k}) \end{bmatrix}. \quad (1.67)$$

419 Solving for the dispersion relation of the system

$$E_{\pm}(\mathbf{k}) = \pm \sqrt{(\epsilon_-(\mathbf{k}))^2 + 4|\Delta_{--}(\mathbf{k})|^2}, \quad (1.68)$$

420 we arrive at an effective p -wave superconductor with opening and closing band gaps.

421 1.5 Landau levels and quantum Hall effect

422 1.5.1 Landau levels in condensed matter systems

423 Here we will discuss the presence of Landau levels (LLs) in condensed matter systems like
 424 Dirac and 2DEG. We are interested in using non-uniform circularly polarized laser light to in-
 425 duce QHE in 2DEG and Dirac systems and determine whether the energy levels are Landau

level-like (LL-like). In the classical case of charged QHE, the charged particles in the system are quantized in cyclotron orbits due to uniform perpendicular magnetic field, these energies are called LLs. To understand why LLs appear and QHE arises we need to first solve the Hamiltonian associated with a 2DEG and Dirac systems in the presence of a perpendicular magnetic field. We can start with the square lattice tight-binding Hamiltonian for a 2DEG

$$\mathcal{H} = - \sum_{\langle j,l \rangle} t c_j^\dagger c_l + h.c., \quad (1.69)$$

and in momentum space

$$\mathcal{H} = - \sum_{\mathbf{p}} 2t (\cos(p_x a) + \cos(p_y a)) c_{\mathbf{p}}^\dagger c_{\mathbf{p}}. \quad (1.70)$$

Then, in the limit of small momenta p we arrive at

$$\begin{aligned} \mathcal{H} &= - \sum_{\mathbf{p}} 2t \left(2 - \frac{p_x^2 a^2}{2} - \frac{p_y^2 a^2}{2} \right) c_{\mathbf{p}}^\dagger c_{\mathbf{p}}, \\ \mathcal{H}(\mathbf{p}) &= \frac{p_x^2 + p_y^2}{2m}, \end{aligned} \quad (1.71)$$

we have arrived at Schrodingers equation for a 2DEG in the limit of small momenta. Let us assume a 2DEG in the x - y plane and have a magnetic field that points in the positive $\hat{\mathbf{z}}$ direction, $\mathbf{B} = B\hat{\mathbf{z}}$ or $\mathbf{A} = Bx\hat{\mathbf{y}}$. The Hamiltonian in momentum space then becomes

$$\mathcal{H} = \frac{1}{2m} (\hat{p}_x^2 + (\hat{p}_y - qB\hat{x})^2) \quad (1.72)$$

Recall $[\hat{r}_\alpha, \hat{p}_\beta] = i\hbar\delta_{\alpha,\beta}$, meaning magnetic term commutes with \hat{p}_y , and lets us assume $\Psi(x, y) = e^{ik_y y} \psi(x)$. Acting the Hamiltonian on the ansatz wavefunction yields

$$\mathcal{H} = \frac{1}{2m} (\hat{p}_x^2 + q^2 B^2 \hat{x}^2) \quad (1.73)$$

438 letting $x - \frac{\hbar k_y}{qB} \rightarrow x$, a shift in x coordinates. This is the expression for a quantum harmonic
 439 oscillator. A derivation for the energy solutions can be found in [B.1](#). With the energy solutions

$$E_n = \frac{\hbar q B}{m} \left(n + \frac{1}{2} \right) = \hbar \omega \left(n + \frac{1}{2} \right) \quad (1.74)$$

440 An alteration to the lattice model can have slightly different results. Using a honeycomb
 441 lattice, provided by graphene, gives the following Hamiltonian

$$\mathcal{H} = -t \sum_{\substack{j,l \\ \alpha\beta}} c_{ja}^\dagger c_{l\beta} + h.c., \quad (1.75)$$

442 with lattice vectors $\mathbf{a}_1 = \sqrt{3}a\hat{\mathbf{x}}$ and $\mathbf{a}_2 = \frac{\sqrt{3}}{2}a\hat{\mathbf{x}} + \frac{3}{2}a\hat{\mathbf{y}}$. In momentum space

$$\mathcal{H} = -t \sum_{\mathbf{p}} \begin{bmatrix} 0 & 1 + e^{i\mathbf{p}\cdot\mathbf{a}_1} + e^{i\mathbf{p}\cdot\mathbf{a}_2} \\ 1 + e^{-i\mathbf{p}\cdot\mathbf{a}_1} + e^{-i\mathbf{p}\cdot\mathbf{a}_2} & 0 \end{bmatrix},$$

443 which gives the following energy spectrum

$$E(\mathbf{p}) = \pm t \sqrt{3 + 2 \cos(\sqrt{3}p_x a) + 4 \cos\left(\frac{\sqrt{3}p_x a}{2}\right) \cos\left(\frac{3p_y a}{2}\right)}. \quad (1.76)$$

444 There are several high symmetry points on the corners of the Brillouin zone, one point is $\mathbf{K} =$
 445 $\frac{4\pi}{3\sqrt{3}a}\hat{\mathbf{x}}$. Expanding about \mathbf{K} with small \mathbf{q} , $\mathbf{q} = \mathbf{p} + \mathbf{K}$, results in

$$t(\mathbf{q}) \approx v_F e^{i2\pi/3} (q_x - i q_y),$$

$$t^*(\mathbf{q}) \approx v_F e^{-i2\pi/3} (q_x + i q_y),$$

446 keeping the leading order in \mathbf{q} and $v_F = \frac{3ta}{2}$. Using a gauge transformation and redefining $\mathbf{q} \rightarrow \mathbf{p}$
 447 the Dirac equation becomes

$$\mathcal{H}(\mathbf{p}) = v_F \boldsymbol{\sigma} \cdot \mathbf{p}. \quad (1.77)$$

448 With graphene spanning the x - y plane in the presence of a magnetic field $\mathbf{B} = B\hat{\mathbf{z}}$, $\mathbf{A} = Bx\hat{\mathbf{y}}$, the
 449 Dirac equation becomes

$$\mathcal{H}(\mathbf{p}) = v_F \boldsymbol{\sigma} \cdot (\mathbf{p} - q\mathbf{A}). \quad (1.78)$$

450 A derivation for the energy solution can be found in [B.2](#). The quantized energy solutions for a
 451 2D Dirac equation in the presence of perpendicular magnetic field are

$$E_n = v_F \sqrt{2n\hbar qB} \quad (1.79)$$

452 Energy in both systems produce discrete quantized energies for charged particles in cy-
 453 clotron orbits with no dependence on momenta, by definition LLs. It is important to note
 454 these Landau levels are highly degenerate flat bands, which will lend to the discussion of bulk
 455 insulating states.

456 1.5.2 Quantized Hall conductivity and Chern number

457 Here we will go over the relationship between quantized Hall conductivity and Chern num-
 458 ber, which is described as

$$\sigma_{xy} = -C \frac{e^2}{h}, \quad C \in \mathbb{Z}. \quad (1.80)$$

459 Consider a 2D system with translation symmetry in the x and y axis with lattice constants l_x
 460 and l_y , respectively. The Brillouin zone boundaries are

$$k_x = \frac{\pi}{l_x}[-1, 1) \quad \text{and} \quad k_y = \frac{\pi}{l_y}[-1, 1), \quad (1.81)$$

461 where the periodicity in k_x and k_y creates a torus, \mathbf{T} , in 3D space. We now introduce the Kubo
 462 formula, which is a linear response to a physical observable by a time-dependent perturbation,
 463 for conductivity as

$$\sigma_{xy} = i\hbar \sum_{E_a < E_F < E_b} \int_{\mathbf{T}} \frac{d^2 k}{(2\pi)^2} \frac{\langle u_{\mathbf{k}}^a | J_y | u_{\mathbf{k}}^b \rangle \langle u_{\mathbf{k}}^b | J_x | u_{\mathbf{k}}^a \rangle - \langle u_{\mathbf{k}}^a | J_x | u_{\mathbf{k}}^b \rangle \langle u_{\mathbf{k}}^b | J_y | u_{\mathbf{k}}^a \rangle}{(E_b - E_a)^2}. \quad (1.82)$$

464 The a and b terms represent dispersion bands below and above the Fermi energy, respectively,
 465 and a basic requirement the bands be separated to allow for an insulating state. Recall, current
 466 density defined by $\mathbf{J} = (e/\hbar)\partial_{\mathbf{k}}H$. If H is written in a basis where current density is non-zero we
 467 can continue. Plugging current density in Eq. (1.82) gives

$$\sigma_{xy} = \frac{ie^2}{h} \sum_{E_a < E_F < E_b} \int_{\mathbf{T}} \frac{d^2 k}{2\pi} \frac{\langle u_{\mathbf{k}}^a | \partial_{k_y} H | u_{\mathbf{k}}^b \rangle \langle u_{\mathbf{k}}^b | \partial_{k_x} H | u_{\mathbf{k}}^a \rangle - \langle u_{\mathbf{k}}^a | \partial_{k_x} H | u_{\mathbf{k}}^b \rangle \langle u_{\mathbf{k}}^b | \partial_{k_y} H | u_{\mathbf{k}}^a \rangle}{(E_b - E_a)^2}. \quad (1.83)$$

468 Using the product rule on the following expression $\langle \alpha | \partial_j (H | \beta) \rangle$ and using $\sum_b = \mathbf{1} - \sum_a | u_{\mathbf{k}}^a \rangle \langle u_{\mathbf{k}}^a |$
 469 simplifies the previous expression to

$$\sigma_{xy} = \frac{e^2}{h} \sum_a \int_{\mathbf{T}} \frac{d^2 k}{2\pi} i \left(\langle \partial_{k_y} u_{\mathbf{k}}^a | \partial_{k_x} u_{\mathbf{k}}^a \rangle - \langle \partial_{k_x} u_{\mathbf{k}}^a | \partial_{k_y} u_{\mathbf{k}}^a \rangle \right) = \frac{e^2}{h} \sum_a \int_{\mathbf{T}} \frac{d^2 k}{2\pi} \mathcal{F}_{xy} \quad (1.84)$$

470 recognizing the integral is the negative Chern number integral, which is always integer. The
 471 Hall conductivity becomes

$$\sigma_{xy} = -\frac{e^2}{h} \sum_a C_a = -C \frac{e^2}{h}. \quad (1.85)$$

472 Hall conductivity becomes quantized and increases as for each flat band below the Fermi level.
 473 This is one way to describe the topological invariant of the quantum Hall effect by looking at
 474 geometry of momentum space with PBC.

475 1.5.3 Laughlin pump on a Hall cylinder

476 We demonstrate another way to describe quantum Hall effect for Landau Levels on a Hall
 477 cylinder. For a 2D system let there be PBC in the y -axis with length L , which discretizes mo-
 478 mentum space into $k = 2\pi n/L$ points. This creates a cylinder with y in the angular axis and x in
 479 the axial axis. Laughlin pumping requires one apply a flux along the cylinder's x axis. We can
 480 introduce the flux in the gauge potential as

$$\mathbf{A} = (Bx + \Phi/L)\hat{\mathbf{y}}. \quad (1.86)$$

481 Inserting the flux into the LL Schrodinger Hamiltonian gives

$$\mathcal{H} = \frac{1}{2m^*} \left(p_x^2 + \left(\frac{2\pi\hbar n}{L} + eBx + \frac{e\Phi}{L} \right)^2 \right). \quad (1.87)$$

482 This becomes the quantum harmonic oscillator solution seen earlier letting $x' = x + x_n$ and

$$x_n = \frac{\hbar}{eBL} \left(n + \frac{\Phi}{\Phi_0} \right), \quad (1.88)$$

483 where $\Phi_0 = \hbar/e$ is the flux quanta. The generalized LL wave function solution is

$$\psi_n(x) \propto H_n(x + x_n) e^{-eB(x+x_n)^2/2\hbar} e^{i2\pi n/L}, \quad (1.89)$$

484 where $H_n(x)$ is the Hermite polynomial. Solving for $\langle x_n \rangle = \langle \psi_n(x) | x | \psi_n(x) \rangle$ results in each elec-
 485 tron centered at Eq. (1.88).

486 When the flux increments by one flux quanta each electron's center of mass moves by the
 487 same integer multiple, i.e. the states move from $n \rightarrow n+1$. This is a change in charge as electrons
 488 are pumped from one state to the next, or from one edge of the cylinder to the other. If n LLs are

489 filled then n electrons are transferred, as $\Delta Q = ne$. Hall conductivity is written as $\sigma_H = \Delta Q / \Delta \Phi$.
490 After a change in flux $\Delta \Phi = \Phi_0$, Hall conductivity is quantized as $\sigma_H = ne^2 / h$. Once again, Hall
491 conductivity is quantized for LL systems.

492 When the flux increases by one flux quanta, the electron's center of mass shifts by an integer
493 multiple, moving from states $n \rightarrow n + 1$. This causes a charge transfer as electrons are pumped
494 across the Laughlin cylinder. If n LLs are filled, n electrons are transferred, hence $\Delta Q = ne$.
495 Hall conductivity is $\sigma_H = \Delta Q / \Delta \Phi$, and for a change in n flux quanta, it becomes quantized as
496 $\sigma_H = ne^2 / h$. Thus, Hall conductivity remains quantized in LLs systems mapped to a Laughlin
497 cylinder.

Chapter 2

Superconducting Triangular Islands as a Platform for Manipulating Majorana Zero Modes

2.1 Context

This chapter consists of the paper *Superconducting triangular islands as a platform for manipulating Majorana zero modes*, which was published in Physical Review B in 2024. The full reference is:

A. Winblad, H. Chen, Phys. Rev. B **109**, 205158 (2024).

The supplemental information is shown in section 2.3. This article shows two ways to incorporate geometry and gauge potentials in triangular lattice models to host and manipulate Majorana zero modes for topological quantum computing systems.

Contributions

2.2 Paper abstract

Current proposals for topological quantum computation (TQC) based on Majorana zero modes (MZM) have mostly been focused on coupled-wire architecture which can be challenging to implement experimentally. To explore alternative building blocks of TQC, in this work we study the possibility of obtaining robust MZM at the corners of triangular superconducting islands, which often appear spontaneously in epitaxial growth. We first show that a minimal three-site triangle model of spinless p -wave superconductor allows MZM to appear at different pairs of vertices controlled by a staggered vector potential, which may be realized using coupled quantum dots and can already demonstrate braiding. For systems with less fine-tuned parameters, we suggest an alternative structure of a “hollow” triangle subject to uniform supercurrents or vector potentials, in which MZM generally appear when two of the edges are in a different

topological phase from the third. We also discuss the feasibility of constructing the triangles using existing candidate MZM systems and of braiding more MZM in networks of such triangles.

Research article

Introduction

For more than twenty years, Majorana zero modes (MZM) in condensed matter systems have been highly sought after due to their potential for serving as building blocks of topological quantum computation, thanks to their inherent robustness against decoherence and non-Abelian exchange statistics [7, 9, 11–13]. MZM were originally proposed to be found in half-quantum vortices of two-dimensional (2D) topological p -wave superconductors and at the ends of 1D spinless p -wave superconductors [8, 14]. Whether a pristine p -wave superconductor [15] has been found is still under debate. However, innovative heterostructures proximate to ordinary s -wave superconductors have been proposed to behave as effective topological superconductors in both 1D and 2D. These include, for example, semiconductor nanowires subject to magnetic fields [16–18], ferromagnetic atomic spin chains [19–24], 3D topological insulators [25–28], quantum anomalous Hall insulators [29–31], quasi-2D spin-orbit-coupled superconductors with a perpendicular Zeeman field [10, 32–36], and planar Josephson junctions [37–43], etc. It has been a challenging task to decisively confirm the existence of MZM in the various experimental systems due to other competing mechanisms that can potentially result in similar features as MZM do in different probes [40, 41, 44–49]. Other proposals for constructing Kitaev chains through a bottom-up approach, based on, e.g. magnetic tunnel junctions proximate to spin-orbit-coupled superconductors [50], and quantum dots coupled through superconducting links [51–53] are therefore promising. In particular, the recent experiment [53] of a designer minimal Kitaev chain based on two quantum dots coupled through tunable crossed Andreev reflections (CAR) offers a compelling route towards MZM platforms based on exactly solvable building blocks.

In parallel with the above efforts of realizing MZM in different materials systems, scalable architectures for quantum logic circuits based on MZM have also been intensely studied over

the past decades. A major proposal among these studies is to build networks of T-junctions, which are minimal units for swapping a pair of MZM hosted at different ends of a junction, that allow braiding-based TQC [13]. Alternatively, networks based on coupled wires forming the so-called tetrons and hexons, aiming at measurement-based logic gate operations [54], have also been extensively investigated. To counter the technical challenges of engineering networks with physical wires or atomic chains, various ideas based on effective Kitaev chains, such as quasi-1D systems in thin films [55], cross Josephson junctions [43], scissor cuts on a quantum anomalous Hall insulator [31], and rings of magnetic atoms [56], etc. have been proposed. However, due to the same difficulty of obtaining or identifying genuine MZM in quasi-1D systems mentioned above, it remains unclear how practical these strategies are in the near future. These challenges, along with the advancements in building designer minimal Kitaev chains, motivate us to explore new MZM platforms that are not based on bulk-boundary correspondence: In small systems with only a few fermion degrees of freedom, discussing the emergence of MZM due to bulk-boundary correspondence is less meaningful. Instead, it is easier to fine-tune system parameters based on exactly solvable models to realize well-behaved MZM.

Additionally, in this Letter we highlight triangular superconducting islands as a promising structural unit for manipulating MZM. Unique geometries combined with simple protocols of control parameters can greatly facilitate MZM creation and operations [56–59]. We also note that triangles naturally break 2D inversion symmetry and do not present a straightforward strategy for morphing into either 1D or 2D structures with periodic boundary conditions, implying different bulk-boundary physics from other quasi-2D structures. Finally, it is worth mentioning that triangular islands routinely appear spontaneously in epitaxial growth [60] on close-packed atomic surfaces.

In this Letter we propose two triangular geometry designs that are pertinent to different experimental platforms. The first is an exactly solvable “Kitaev triangle” model consisting of three fermion sites. The Kitaev triangle hosts MZM at different pairs of vertices controlled by Peierls phases on the three edges [Fig. 2.1 (a)], that is not due to topological bulk-boundary cor-

575 response, and can realize the braiding of two MZM. The second is finite-size triangles with a
 576 hollow interior [Fig. 2.1 (b)] under a uniform vector potential, which tunes its individual edges
 577 into different topological phases. Compared to existing proposals based on vector potentials
 578 or supercurrents [61–64], our design explores the utility of geometry rather than the individ-
 579 ual control of superconducting nanowires. We also discuss scaled-up networks of triangles for
 580 implementing braiding operations of MZM.

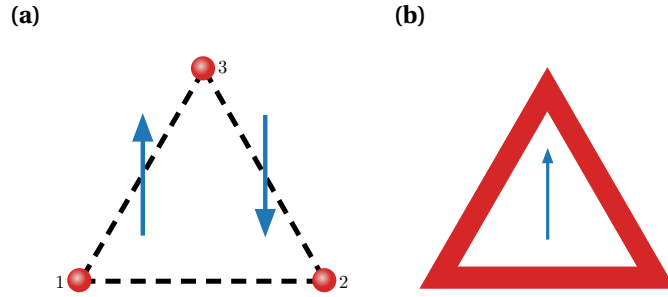


Figure 2.1: Schematics of two triangle structures proposed in this work. (a) Three-site Kitaev triangle with bond-dependent Peierls phases. (b) Hollow triangular island with a uniform vector potential.

581 Kitaev triangle

582 In this section we present an exactly solvable minimal model with three sites forming a “Ki-
 583 taev triangle” that can host MZM at different pairs of vertices controlled by Peierls phases on the
 584 edges. The Bogoliubov-de Gennes (BdG) Hamiltonian includes complex hopping and p -wave
 585 pairing between three spinless fermions forming an equilateral triangle [Fig. 2.1 (a)]:

$$\mathcal{H} = \sum_{\langle j l \rangle} (-t e^{i\phi_{jl}} c_j^\dagger c_l + \Delta e^{i\theta_{jl}} c_j c_l + \text{h.c.}) - \sum_j \mu c_j^\dagger c_j, \quad (2.1)$$

586 where t is the hopping amplitude, Δ is the amplitude of the (2D) p -wave pairing, μ is the chem-
 587 ical potential, θ_{jl} is the azimuthal angle of $\mathbf{r}_{jl} = \mathbf{r}_l - \mathbf{r}_j$ (the x axis is chosen to be along \mathbf{r}_{12}),
 588 consistent with $\{c_l^\dagger, c_j^\dagger\} = 0$. ϕ_{jl} is the Peierls phase due to a bond-dependent vector poten-
 589 tial \mathbf{A} to be specified below (the nearest neighbor distance a is chosen to be the length unit

and $e = \hbar = 1$ hereinbelow): $\phi_{jl} = \int_{\mathbf{r}_j}^{\mathbf{r}_l} \mathbf{A} \cdot d\mathbf{l} = -\phi_{lj}$. We have chosen a gauge so that the vector potential only appears in the normal part of the Hamiltonian [65], and the p -wave gap Δ is assumed to be an effective one induced by proximity to a neighboring superconductor, on which the vector potential has negligible influence. The minimal model may be realized as an effective low-energy model of carefully engineered mesoscopic superconductor devices, such as that made by quantum dots connected by superconducting islands [53]. Rewriting \mathcal{H} in the Majorana fermion basis $a_j = c_j + c_j^\dagger$, $b_j = \frac{1}{i}(c_j - c_j^\dagger)$ and specializing to the Kitaev limit $t = \Delta$, $\mu = 0$, we can obtain explicit conditions for getting MZM at different sites [66]. For example, first let $\phi_{12} = 0$ so that sites 1 and 2 alone form a minimal Kitaev chain with $\mathcal{H}_{12} = itb_1a_2$ and hosting MZM a_1 and b_2 . Then one can set ϕ_{23} and ϕ_{31} so that all terms involving the above two Majorana operators cancel out. Solving the corresponding equations gives $\phi_{23} = -\pi/3$ and $\phi_{31} = -\phi_{13} = -\pi/3$. The three Peierls phases can be realized by the following staggered vector potential

$$\mathbf{A} = [1 - 2\Theta(x)] \frac{2\pi}{3\sqrt{3}} \hat{\mathbf{y}} \quad (2.2)$$

where $\Theta(x)$ is the Heaviside step function. The above condition for MZM localized at triangle corners can be generalized to Kitaev chains forming a triangular loop, as well as to finite-size triangles of 2D spinless p -wave superconductors in the Kitaev limit, as the existence of a_1 and b_2 are only dictated by the vector potential near the corresponding corners. It should be noted that in the latter case, 1D edge states will arise when the triangle becomes larger, and effectively diminish the gap that protects the corner MZM. In this sense, the gap that protects the MZM in the Kitaev triangle model, defined by the energies of the first excited states $\pm(1 - \frac{\sqrt{2}}{2})t \approx \pm 0.29t$ [66], is due to finite size effects. On the other hand, for the longer Kitaev chain, another pair of MZM will appear near the two bottom vertices which can be understood using a topological argument given in the next section. In this sense, the MZM in the Kitaev triangle here are not due to topological bulk-boundary correspondence [the point of $A = \frac{2\pi}{3\sqrt{3}}$ and $\mu = 0$ sits in the trivial phase in Fig. 2.3 (a)].

615 We next show that the minimal Kitaev triangle suffices to demonstrate braiding of MZM. To
 616 this end we consider a closed parameter path linearly interpolating between the following sets
 617 of values of ϕ_{jl} :

$$(\phi_{12}, \phi_{23}, \phi_{31}) : \boldsymbol{\phi}_1 \rightarrow \boldsymbol{\phi}_2 \rightarrow \boldsymbol{\phi}_3 \rightarrow \boldsymbol{\phi}_1 \quad (2.3)$$

618 with $\boldsymbol{\phi}_1 = (0, -\frac{\pi}{3}, -\frac{\pi}{3})$, $\boldsymbol{\phi}_2 = (-\frac{\pi}{3}, -\frac{\pi}{3}, 0)$, $\boldsymbol{\phi}_3 = (-\frac{\pi}{3}, 0, -\frac{\pi}{3})$. It is straightforward to show that at $\boldsymbol{\phi}_2$
 619 and $\boldsymbol{\phi}_3$ there are MZM located at sites 1, 3 and 2, 3, respectively. Therefore the two original MZM
 620 at sites 1, 2 should switch their positions at the end of the adiabatic evolution.

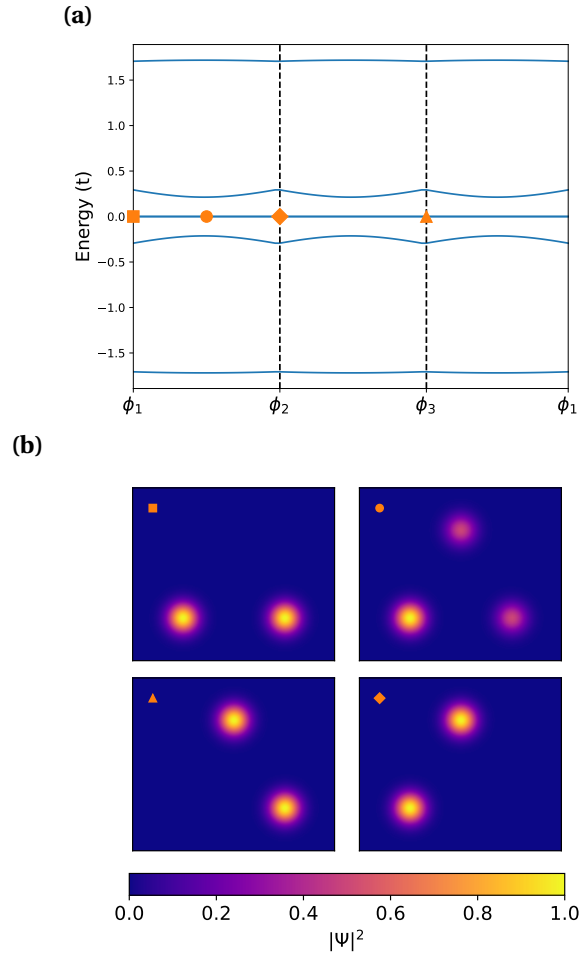


Figure 2.2: (a) Evolution of the eigenvalues of the 3-site Kitaev triangle along the closed parameter path for ϕ on the three edges. (b) MZM wavefunctions at different points of the parameter path. Clockwise from the upper left panel: $\boldsymbol{\phi}_1 \rightarrow \frac{1}{2}(\boldsymbol{\phi}_1 + \boldsymbol{\phi}_2) \rightarrow \boldsymbol{\phi}_2 \rightarrow \boldsymbol{\phi}_3$.

Fig. 2.2 shows that the MZM stays at zero energy throughout the parameter path that interchanges their positions. In [66] we proved the exact degeneracy of the MZM along the path [67]. To show that such an operation indeed realizes braiding, we explicitly calculated the many-body Berry phase of the evolution [9, 56, 66] and found the two degenerate many-body ground states acquire a $\frac{\pi}{2}$ difference in their Berry phases as expected [9]. Compared to the minimum T-junction model with four sites [9, 68], our Kitaev triangle model only requires three sites to achieve braiding between two MZM, and is potentially easier to engineer experimentally.

Hollow triangles

For systems with less fine-tuned Hamiltonians than the minimal model in the previous section, it is more instructive to search for MZM based on topological bulk-boundary correspondence. In this section we show that MZM generally appear at the corners of a hollow triangle, which can be approximated by joining three finite-width chains or ribbons whose bulk topology is individually tuned by the same uniform vector potential.

To this end, we first show that topological phase transitions can be induced by a vector potential in a spinless p -wave superconductor ribbon as illustrated in Fig. 2.3 (a). In comparison with similar previous proposals that mostly focused on vector potentials or supercurrents flowing along the chain [61, 62], we consider in particular the tunability by varying the direction of the vector potential relative to the length direction of the ribbon, which will become instrumental in a triangular structure.

Consider Eq. (A.75) on a triangular lattice defined by unit-length lattice vectors $(\mathbf{a}_1, \mathbf{a}_2) = (\hat{\mathbf{x}}, \frac{1}{2}\hat{\mathbf{x}} + \frac{\sqrt{3}}{2}\hat{\mathbf{y}})$ with W unit cells along \mathbf{a}_2 but infinite unit cells along \mathbf{a}_1 , and assume the Peierls phases are due to a uniform vector potential \mathbf{A} so that $\phi_{jl} = \mathbf{A} \cdot \mathbf{r}_{jl}$. The Hamiltonian is periodic along x and can be Fourier transformed through $c_{m,n}^\dagger = \frac{1}{\sqrt{N}} \sum_k c_{k,n}^\dagger e^{-ikm}$, where m, n label the lattice sites as $\mathbf{r}_{m,n} = m\mathbf{a}_1 + n\mathbf{a}_2$. The resulting momentum space Hamiltonian [66] can then be used to calculate the Majorana number [8, 69] \mathcal{M} of the 1D ribbon. When $\mathcal{M} = -1$, the 1D system is in a nontrivial topological phase with MZM appearing at open ends of semi-infinite ribbons, and otherwise for $\mathcal{M} = 1$.

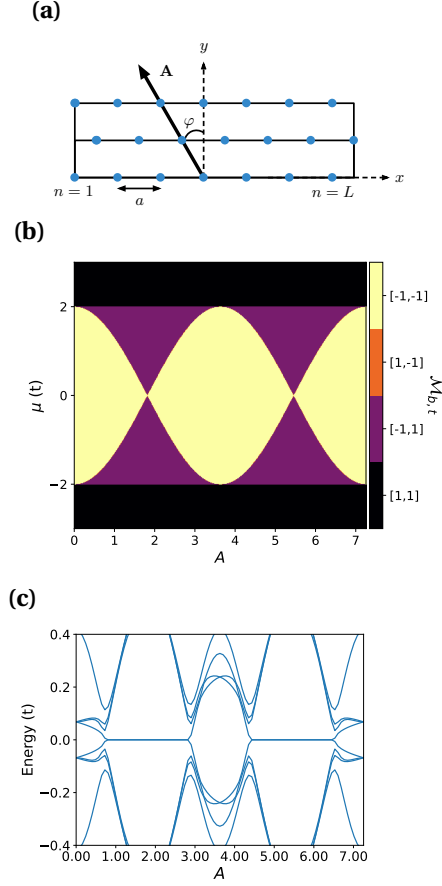


Figure 2.3: (a) Schematic illustration of a finite-width ($W = 3$ here) ribbon based on the triangular lattice in the presence of a vector potential $\mathbf{A} = A(-\sin\phi\hat{\mathbf{x}} + \cos\phi\hat{\mathbf{y}})$. (b) Topological phase diagram for a $W = 1$ triangular chain obtained by superimposing the $\mathcal{M}_{b,t}(A, \mu)$ (b -bottom edge, t -top edges) plots of 1D chains with $\mathbf{A} = A\hat{\mathbf{y}}$ (bottom edge) and $\mathbf{A} = A(\frac{\sqrt{3}}{2}\hat{\mathbf{x}} + \frac{1}{2}\hat{\mathbf{y}})$ (top edges). Color scheme: black— $[\mathcal{M}_b, \mathcal{M}_t] = [1, 1]$, yellow— $[-1, -1]$, purple— $[-1, 1]$, orange— $[1, -1]$ (not present in this case) (b) Near-gap BdG eigen-energies vs A for a finite triangle with edge length $L = 50$, $W = 1$, and $\mu = 1.6$. $t = \Delta = 1$ in all calculations.

In Fig. 2.3 (b) we show the topological phase diagrams for a 1D ribbon with width $W = 1$, $\mathbf{A} = A\hat{\mathbf{y}}$ and $\mathbf{A} = A(\frac{\sqrt{3}}{2}\hat{\mathbf{x}} + \frac{1}{2}\hat{\mathbf{y}})$ superimposed. We found that the vector potential component normal to the ribbon length direction has no effect on the Majorana number, nor does the sign of its component along the ribbon length direction. However, topological phase transitions can be induced by varying the size of the vector potential component along the ribbon, consistent with previous results [61, 62]. These properties motivate us to consider the structure of a hollow triangle formed by three finite-width ribbons subject to a uniform vector potential $\mathbf{A} = A\hat{\mathbf{y}}$ as illustrated in Fig. 2.1 (b), in which the bottom edge is aligned with $\hat{\mathbf{x}}$. The purple regions on

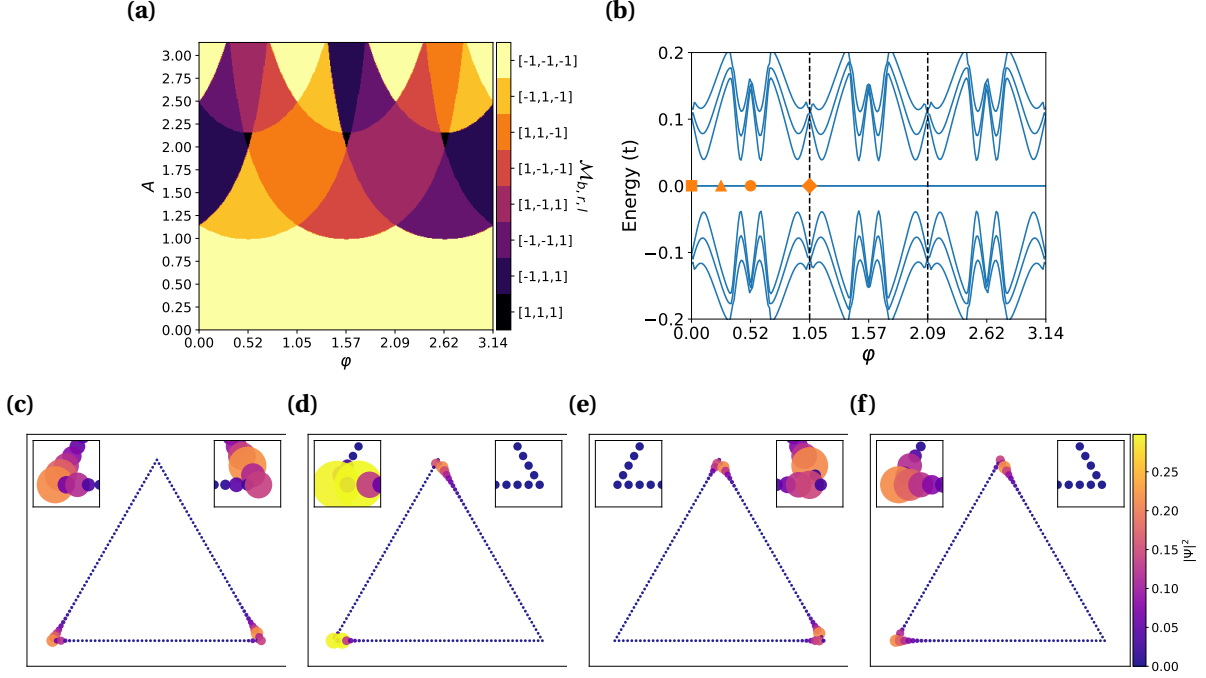


Figure 2.4: (a) Topological phase diagram for a $W = 1$ triangle by superimposing the $\mathcal{M}_{b,r,l}(A, \varphi)$ plots of 1D chains (b -bottom, r -right, l -left, $\mu = 1.1$). $\varphi_{r,l}$ are equal to $\varphi_b + \pi/3$ and $\varphi_b - \pi/3$, respectively. The colors are coded by which edges have non-trivial topology. For example, Black— $[\mathcal{M}_b, \mathcal{M}_r, \mathcal{M}_l] = [1, 1, 1]$ means all edges are trivial. The behavior depicted in panels (b-f) is representative of that when A is in the range of $(2.25, 2.5)$, for which the $\mathcal{M} = -1$ phase “crawls” through the three edges counterclockwise as φ increases. (b) Spectral flow of a triangle with $W = 1$, $L = 50$, $\mu = 1.1$, and $A = 2.35$ with increasing φ . (c-f) BdG eigenfunction $|\Psi|^2$ summed over the two zero modes at $\varphi = 0, \frac{\pi}{12}, \frac{\pi}{6},$ and $\frac{\pi}{3}$, respectively. The bottom edge is parallel with $\hat{\mathbf{x}}$ in the coordinates illustrated in Fig. 2.3 (a).

the phase diagram Fig. 2.3 (a) mean the bottom edge and the two upper edges of the hollow triangle have different \mathcal{M} , which should give rise to MZM localized at the two bottom corners if the triangle is large enough so that bulk-edge correspondence holds, and gap closing does not occur at other places along its edges.

To support the above arguments, we directly diagonalize the BdG Hamiltonian of a finite hollow triangle with edge length $L = 50$ and width $W = 1$. Fig. 2.3 (c) shows the spectral flow (BdG eigen-energies evolving with increasing vector potential A) close to zero energy at chemical potential $\mu = 1.6$. Indeed, zero-energy modes appear in the regions of μ and A consistent with the phase diagram. Hollow triangles with larger W also have qualitatively similar behavior, although the phase diagrams are more complex [66]. The eigenfunctions for the zero-energy

666 modes at $A = 2.35$ and $\mu = 1.1$ in Fig. 2.4 (c) also confirm their spatial localization at the bottom
 667 corners of the triangle.

668 We next show that rotating the uniform vector potential in-plane, guided by the phase dia-
 669 gram of the three edges overlapped together [Fig. 2.4 (a)], can manipulate the positions of the
 670 MZM. Specifically, a desired path on the (A, φ) plane, φ being the in-plane azimuthal angle of \mathbf{A}
 671 [Fig. 2.3 (a)], of the phase diagram should make the nontrivial $\mathcal{M} = -1$ phase cycle through the
 672 three edges but without entering any trivial regions, when all edges have the same \mathcal{M} .

673 Fig. 2.4 (b) plots the spectral flow versus φ for a path determined in the above manner,
 674 which clearly shows that the zero-energy modes persist throughout the rotation and the bulk
 675 gap never closes. At a critical point when individual edges change their topology, e.g., near the
 676 middle of the $\varphi \in [0, \pi/6)$ region, gap closing is avoided due to finite-size effects, as discussed
 677 in [9]. Figs. 2.4 (c-f) plot the BdG wavefunctions of the MZM at special values of φ . One can see
 678 that the two MZM appear to cycle through the three vertices by following the rotation of \mathbf{A} . We
 679 note in passing that if the vector potentials on the three edges can be controlled independently
 680 similar to the Kitaev triangle case, a swapping of the two MZM can in principle be achieved as
 681 well.

682 In [66] we also gave an example of a $W = 3$ triangle, for which one has to additionally con-
 683 sider the nontrivial dependence of the bulk gap of the three edges on \mathbf{A} . In general, optimization
 684 of the parameter path can be done by examining the (suitably designed) topological phase dia-
 685 gram together with the bulk gap diagram, and choosing triangles of appropriate sizes.

686 Before ending this section, we present a tentative design for braiding more than two MZM
 687 based on our hollow triangles. The structure, illustrated in Fig. 2.5, consists of four triangles
 688 sharing corners with their neighbors. The critical step of transporting γ_2 to the left vertex of
 689 the rightmost triangle, corresponding to Figs. 2.5 (b,c), can be achieved by rotating the vector
 690 potential of the bottom-middle triangle counterclockwisely from $\varphi = \frac{\pi}{6}$ to $\frac{\pi}{3}$, which swaps the
 691 topological phases of the two side edges as shown in Fig. 2.4. In [66] we show this operation
 692 does not involve gap closing when the parameter path is chosen judiciously.

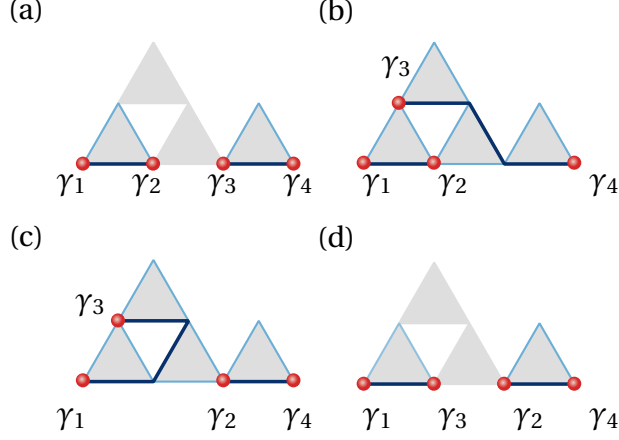


Figure 2.5: Representative steps for braiding four MZM in four triangles sharing corners. (a) Initialization of four MZM $\gamma_1, \gamma_2, \gamma_3, \gamma_4$. All three edges of the bottom-middle and the top triangles are in the trivial phase by e.g. controlling the chemical potential. The bottom-left and bottom-right triangles have $\varphi = 0$ so that their bottom edges are nontrivial. (b) Moving γ_3 by “switching on” the middle triangle by changing the chemical potential under a fixed vector potential at $\varphi = \frac{\pi}{6}$, and then turning on the top triangle with similar means except $\varphi = 0$. (c) Transporting γ_2 to the right triangle through rotating the vector potential in the middle triangle counterclockwise by $\pi/6$. (d) Moving γ_3 to the left triangle by “switching off” the top triangle followed by the middle triangle.

Discussion

The hollow interior of the triangles considered in this work is needed for two reasons: (1) $W \ll L$ is required for bulk-edge correspondence based on 1D topology to hold; (2) A finite W is needed to gap out the chiral edge states of a 2D spinless p -wave superconductor. The latter is not essential if one does not start with a spinless p -wave superconductor but a more realistic model such as the Rashba+Zeeman+s-wave pairing model. On the other hand, the former constraint may also be removed if one uses the Kitaev triangle. Nonetheless, an effective 3-site Kitaev triangle may emerge as the effective theory of triangular structures if a three-orbital low-energy Wannier basis can be isolated, similar to the continuum theory of moiré structures. We also note that the corner MZM in our triangles appear due to different reasons from that in higher-order topological superconductors [47, 57–59].

For possible physical realizations of our triangles, immediate choices are quantum dots forming a Kitaev triangle [53], planar Josephson junctions or cuts on quantum anomalous Hall insulator/superconductor heterostructures [31] that form a hollow triangle, and triangular atomic

chains assembled by an STM tip [24] on a close-packed surface. The quantum-dot platform may be advantageous in the convenience of implementing parity readout by turning the third vertex temporarily into a normal quantum dot [67, 70, 71]. Looking into the future, it is more intriguing to utilize the spontaneously formed triangular islands in epitaxial growth [60] with the center region removed either physically by lithography/ablation, or electrically by gating. To create a staggered vector potential or supercurrent profile for the Kitaev triangle, one can use a uniform magnetic field, corresponding to a constant vector potential gradient, plus a uniform supercurrent that controls the position of the zero. It is also possible to use two parallel superconducting wires with counter-propagating supercurrents proximate to the triangle. Our work provides a versatile platform for manipulating MZM based on currently available candidate MZM systems and for potentially demonstrating the non-Abelian nature of MZM in near-term devices.

2.3 Supplemental material

Analytic solutions of the Kitaev triangle

In this section we present some analytic results related to the 3-site Kitaev triangle.

We start from the 1D Kitaev chain Hamiltonian with complex nearest-neighbor hopping $-te^{i\phi}$ and p -wave pairing $\Delta e^{i\theta}$ in the Kitaev limit ($t = \Delta > 0, \mu = 0$):

$$H = \sum_n \left(-te^{i\phi} c_n^\dagger c_{n+1} + \Delta e^{i\theta} c_n c_{n+1} + \text{h.c.} \right) \quad (2.4)$$

In the Majorana fermion basis $a_n = c_n + c_n^\dagger$, $b_n = -i(c_n - c_n^\dagger)$ the Hamiltonian becomes

$$H = -\frac{it}{2} \sum_n \left[(S_\phi - S_\theta) a_n a_{n+1} + (S_\phi + S_\theta) b_n b_{n+1} + (C_\phi - C_\theta) a_n b_{n+1} - (C_\phi + C_\theta) b_n a_{n+1} \right] \quad (2.5)$$

where $S_\phi \equiv \sin \phi$, $C_\phi \equiv \cos \phi$, etc. Therefore, when $\phi = \theta$, a_n becomes decoupled from a_{n+1} and b_{n+1} , and a_1 drops out from the Hamiltonian. Similarly, when $\phi = \theta + \pi$, b_1 becomes isolated.

To find the other MZM, we note that when $\phi = \theta$, terms involving a_N and b_N in the Hamiltonian

728 are

$$H_N = -itb_{N-1}(S_\phi b_N - C_\phi a_N). \quad (2.6)$$

729 Considering the unitary transformation

$$\begin{pmatrix} a'_N \\ b'_N \end{pmatrix} \equiv \begin{pmatrix} C_\phi & -S_\phi \\ S_\phi & C_\phi \end{pmatrix} \begin{pmatrix} a_N \\ b_N \end{pmatrix} \quad (2.7)$$

730 we have

$$H_N = itb_{N-1}a'_N \quad (2.8)$$

731 Therefore the other MZM is $b'_N = S_\phi a_N + C_\phi b_N$. Similarly, when $\phi = \theta + \pi$ the other MZM is
 732 $a'_N \equiv C_\phi a_N - S_\phi b_N$.

733 For the 3-site Kitaev triangle at the initial configuration ϕ_1 , if the three edges were isolated
 734 from each other, the MZM would have been

$$\begin{aligned} 1-2: & \quad a_1, b_2 \\ 2-3: & \quad b_2, \frac{1}{2}a_3 + \frac{\sqrt{3}}{2}b_3 \\ 3-1: & \quad a_1, \frac{\sqrt{3}}{2}a_3 + \frac{1}{2}b_3 \end{aligned} \quad (2.9)$$

735 One can therefore see that the two MZM at site 3 are not compatible with each other.

736 We next solve for the excited states of the Kitaev triangle at the initial configuration ϕ_1 . The
 737 Hamiltonian in the Majorana basis is

$$H = -\frac{it}{2} \left(-2b_1 a_2 - \sqrt{3} a_2 a_3 + a_2 b_3 + \sqrt{3} b_1 b_3 - b_1 a_3 \right) = \frac{1}{2} \Gamma h \Gamma^T \quad (2.10)$$

$$\Gamma \equiv (b_1, a_2, a_3, b_3)$$

$$h \equiv -it \begin{pmatrix} 0 & -1 & -\frac{1}{2} & \frac{\sqrt{3}}{2} \\ 1 & 0 & -\frac{\sqrt{3}}{2} & \frac{1}{2} \\ \frac{1}{2} & \frac{\sqrt{3}}{2} & 0 & 0 \\ -\frac{\sqrt{3}}{2} & -\frac{1}{2} & 0 & 0 \end{pmatrix} = t \left(-\frac{1}{2} \sigma_0 \tau_y - \frac{1}{2} \sigma_z \tau_y - \frac{1}{2} \sigma_y \tau_z + \frac{\sqrt{3}}{2} \sigma_x \tau_y \right)$$

738 h has the following symmetry:

$$O = \left(\frac{\sqrt{3}}{2} \sigma_x - \frac{1}{2} \sigma_z \right) \tau_y \quad (2.11)$$

739 We therefore rotate the Hamiltonian so that O becomes diagonal using the following unitary
 740 operator

$$U = e^{-\frac{i\pi}{3} \sigma_y} \otimes e^{i\frac{\pi}{4} \tau_x} \quad (2.12)$$

741 which leads to

$$U^\dagger O U = \text{Diag}(1, -1, -1, 1) \quad (2.13)$$

742 U therefore block-diagonalizes h as

$$U^\dagger h U = \frac{t}{2} \begin{pmatrix} 1 & & & -1 \\ & -1 & 1 & \\ & 1 & -3 & \\ -1 & & & 3 \end{pmatrix} \quad (2.14)$$

743 which can then be diagonalized by

$$V = \begin{pmatrix} \frac{1+\sqrt{2}}{\sqrt{4+2\sqrt{2}}} & 0 & \frac{1-\sqrt{2}}{\sqrt{4-2\sqrt{2}}} & 0 \\ 0 & \frac{1+\sqrt{2}}{\sqrt{4+2\sqrt{2}}} & 0 & \frac{1-\sqrt{2}}{\sqrt{4-2\sqrt{2}}} \\ 0 & \frac{1}{\sqrt{4+2\sqrt{2}}} & 0 & \frac{1}{\sqrt{4-2\sqrt{2}}} \\ \frac{1}{\sqrt{4+2\sqrt{2}}} & 0 & \frac{1}{\sqrt{4-2\sqrt{2}}} & 0 \end{pmatrix} \quad (2.15)$$

744 as

$$V^\dagger U^\dagger h U V = t \times \text{Diag} \left(1 - \frac{\sqrt{2}}{2}, -1 + \frac{\sqrt{2}}{2}, 1 + \frac{\sqrt{2}}{2}, -1 - \frac{\sqrt{2}}{2} \right) \quad (2.16)$$

745 We therefore have the two lowest excited states with eigenenergies $\pm t(1 - \frac{\sqrt{2}}{2})$

$$\begin{aligned} \psi_{+1} &= \Gamma U \begin{pmatrix} \frac{1+\sqrt{2}}{\sqrt{4+2\sqrt{2}}} \\ 0 \\ 0 \\ \frac{1}{\sqrt{4+2\sqrt{2}}} \end{pmatrix} = \Gamma \times \frac{1}{4\sqrt{2+\sqrt{2}}} \begin{pmatrix} 1 + \sqrt{2} - \sqrt{3}i \\ (1 + \sqrt{2})i - \sqrt{3} \\ i + \sqrt{3} + \sqrt{6} \\ 1 + (\sqrt{3} + \sqrt{6})i \end{pmatrix} \\ \psi_{-1} &= \Gamma U \begin{pmatrix} 0 \\ \frac{1+\sqrt{2}}{\sqrt{4+2\sqrt{2}}} \\ \frac{1}{\sqrt{4+2\sqrt{2}}} \\ 0 \end{pmatrix} = \Gamma \times \frac{1}{4\sqrt{2+\sqrt{2}}} \begin{pmatrix} (1 + \sqrt{2})i - \sqrt{3} \\ 1 + \sqrt{2} - \sqrt{3}i \\ 1 + (\sqrt{3} + \sqrt{6})i \\ i + \sqrt{3} + \sqrt{6} \end{pmatrix} \end{aligned} \quad (2.17)$$

746 The first excited states can therefore be understood as a hybridization between the “bulk” states
747 of the 1-2 bond and the fermion on site 3. The other two eigenstates can be obtained similarly.

748 We next prove that in the braiding process given in the main text there is always a pair of
749 MZM at exactly zero energy. Without loss of generality we consider the $\phi_1 \rightarrow \phi_2$ step. The

750 Hamiltonian in the fermion basis becomes

$$\begin{aligned}
H = & -e^{ix}c_1^\dagger c_2 + c_1 c_2 + e^{-ix}c_1 c_2^\dagger - c_1^\dagger c_2^\dagger \\
& -e^{-\frac{\pi}{3}i}c_2^\dagger c_3 + e^{\frac{2\pi}{3}i}c_2 c_3 + e^{\frac{\pi}{3}i}c_2 c_3^\dagger - e^{-\frac{2\pi}{3}i}c_2^\dagger c_3^\dagger \\
& + e^{(-\frac{\pi}{3}-x)i}c_1 c_3^\dagger - e^{-\frac{2\pi}{3}i}c_1 c_3 - e^{(\frac{\pi}{3}+x)i}c_1^\dagger c_3 + e^{\frac{2\pi}{3}i}c_1^\dagger c_3^\dagger
\end{aligned} \tag{2.18}$$

751 where we have temporarily omitted the energy unit t . We then have

$$\begin{aligned}
[c_1^\dagger, H] &= c_2 + e^{-ix}c_2^\dagger + e^{(-\frac{\pi}{3}-x)i}c_3^\dagger - e^{-\frac{2\pi}{3}i}c_3 \\
[c_1, H] &= -[c_1^\dagger, H]^\dagger = -e^{ix} \left[c_2 + e^{-ix}c_2^\dagger - e^{-\frac{2\pi}{3}i}c_3 + e^{(-\frac{\pi}{3}-x)i}c_3^\dagger \right]
\end{aligned} \tag{2.19}$$

752 Therefore

$$[e^{\frac{ix}{2}}c_1^\dagger + e^{-\frac{ix}{2}}c_1, H] = 0 \tag{2.20}$$

753 Namely we have an MZM:

$$\tilde{a}_1 \equiv e^{\frac{ix}{2}}c_1^\dagger + e^{-\frac{ix}{2}}c_1 = C_{\frac{x}{2}}a_1 + S_{\frac{x}{2}}b_1 \tag{2.21}$$

754 To find the other MZM, we calculate the commutators between the other fermion operators

755 with the Hamiltonian:

$$\begin{aligned}
[c_2^\dagger, H] &= e^{ix}c_1^\dagger - c_1 - e^{-\frac{i\pi}{3}}c_3 + e^{\frac{i\pi}{3}}c_3^\dagger \\
[c_2, H] &= -e^{-ix}c_1 + c_1^\dagger + e^{\frac{i\pi}{3}}c_3^\dagger - e^{-\frac{i\pi}{3}}c_3 \\
[c_3^\dagger, H] &= e^{-\frac{i\pi}{3}}c_2^\dagger + e^{-\frac{i\pi}{3}}c_2 - e^{\frac{i\pi}{3}}c_1 + e^{i(\frac{\pi}{3}+x)}c_1^\dagger \\
[c_3, H] &= -e^{\frac{i\pi}{3}}c_2 - e^{\frac{i\pi}{3}}c_2^\dagger + e^{-\frac{i\pi}{3}}c_1^\dagger - e^{-i(\frac{\pi}{3}+x)}c_1
\end{aligned} \tag{2.22}$$

756 Therefore

$$[c_2 - c_2^\dagger, H] = (1 - e^{-ix})c_1 + (1 - e^{ix})c_1^\dagger \quad (2.23)$$

$$[\left(e^{\frac{i\pi}{6}}c_3 - e^{-i\frac{\pi}{6}}c_3^\dagger\right), H] = e^{\frac{i\pi}{6}}(1 - e^{-i(\frac{\pi}{3}+x)})c_1 + e^{-\frac{i\pi}{6}}(1 - e^{i(\frac{\pi}{3}+x)})c_1^\dagger$$

757 However, the ratio between the coefficients of c_1 or c_1^\dagger in the two commutators above is purely
758 real:

$$-\frac{1 - e^{-ix}}{e^{\frac{i\pi}{6}}(1 - e^{-i(\frac{\pi}{3}+x)})} = -\frac{2 - 2\cos x}{e^{\frac{i\pi}{6}}(1 - e^{-i(\frac{\pi}{3}+x)})(1 - e^{ix})} = \frac{1 - \cos x}{\cos(x + \frac{\pi}{6}) - \frac{\sqrt{3}}{2}} \quad (2.24)$$

759 Thus the following Majorana operator commutes with the Hamiltonian and is the second MZM:

$$\begin{aligned} \tilde{b}_{23} &\equiv -iN \left(\left[\cos\left(x + \frac{\pi}{6}\right) - \frac{\sqrt{3}}{2} \right] (c_2 - c_2^\dagger) + (1 - \cos x) \left(e^{\frac{i\pi}{6}}c_3 - e^{-\frac{i\pi}{6}}c_3^\dagger \right) \right) \\ &= N \left(\left[\cos\left(x + \frac{\pi}{6}\right) - \frac{\sqrt{3}}{2} \right] b_2 + (1 - \cos x) \left(\frac{1}{2}a_3 + \frac{\sqrt{3}}{2}b_3 \right) \right) \end{aligned} \quad (2.25)$$

760 where N is a normalization factor. When $x = 0$ only the first term survives since

$$\lim_{x \rightarrow 0} \frac{1 - \cos x}{\cos(x + \frac{\pi}{6}) - \frac{\sqrt{3}}{2}} = 0 \quad (2.26)$$

761 while when $x = -\frac{\pi}{3}$ only the second term survives. So \tilde{b}_{23} continuously evolves from b_2 to $\frac{1}{2}a_3 +$
762 $\frac{\sqrt{3}}{2}b_3$ along the path $\phi_1 \rightarrow \phi_2$.

763 Many-body Berry phase calculation for the 3-site Kitaev triangle

764 In this section we provide details for calculating the many-body Berry phase for braiding two
765 MZM in the Kitaev triangle, as shown in Fig. 2 in the main text. To start we use the Hamiltonian

766 Eq. (1) in the main text,

$$\mathcal{H} = \sum_{\langle jl \rangle} (-te^{i\phi_{jl}} c_j^\dagger c_l + \Delta e^{i\theta_{jl}} c_j c_l + \text{h.c.}) - \sum_j \mu c_j^\dagger c_j, \quad (2.27)$$

and write the creation and annihilation operators in the following Fock space basis for three spinless fermions

$$\begin{aligned} (|0\rangle, |1\rangle, \dots, |7\rangle) &\equiv \{|n_1, n_2, n_3\rangle\} \\ &= (|0, 0, 0\rangle, \\ &\quad |1, 0, 0\rangle, |0, 1, 0\rangle, |0, 0, 1\rangle, \\ &\quad |0, 1, 1\rangle, |1, 0, 1\rangle, |1, 1, 0\rangle, \\ &\quad |1, 1, 1\rangle) \end{aligned}$$

767 The creation(annihilation) operators in this space are defined as

$$\begin{aligned} c_j^\dagger |n_1, \dots, n_j, \dots\rangle &= \sqrt{n_j + 1} (-1)^{s_j} |n_1, \dots, n_j + 1, \dots\rangle, \\ c_j |n_1, \dots, n_j, \dots\rangle &= \sqrt{n_j} (-1)^{s_j} |n_1, \dots, n_j - 1, \dots\rangle, \end{aligned} \quad (2.28)$$

768 where

$$s_j = \begin{cases} \sum_{l=1}^{j-1} n_l & j > 1 \\ 0 & j = 1 \end{cases} \quad (2.29)$$

769 For the initial configuration corresponding to ϕ_1 in Eq. (6) of the main text, diagonalizing
770 the 8×8 BdG Hamiltonian in the above basis leads to two degenerate ground states that can be
771 distinguished by the occupation number of the following fermion operator constructed from

772 the two MZM at the two bottom vertices

$$c_M \equiv \frac{1}{2}(a_1 + ib_2), \quad n_M \equiv c_M^\dagger c_M \quad (2.30)$$

773 The two degenerate ground states for the initial configuration, denoted as $|0\rangle_i$ and $|1\rangle_i$, there-
774 fore satisfy

$$n_M|0\rangle_i = 0, \quad (2.31)$$

$$n_M|1\rangle_i = |1\rangle_i$$

775 In practice, we first construct the operator R_{gs} as a 8×2 matrix by combining the two column
776 eigenvectors of the two lowest-energy eigenstates of the initial BdG Hamiltonian:

$$R_{\text{gs}} \equiv (\psi_i, \psi'_i) \quad (2.32)$$

777 and then diagonalize the projected n_M operator:

$$U_n^\dagger (R_{\text{gs}}^\dagger n_M R_{\text{gs}}) U_n \equiv R_i^\dagger n_M R_i = \begin{pmatrix} 0 & \\ & 1 \end{pmatrix} \quad (2.33)$$

778 To carry out the Berry phase calculation we next need to adiabatically “rotate” the vector
779 potential field by following the linearly interpolated closed parameter path described in the
780 main text, which is discretized into $N + 1$ segments. At any given point labeled by j along the
781 path, we diagonalize the corresponding Hamiltonian and construct the projection operator P_j
782 using the two lowest-energy eigenvectors ψ_j, ψ'_j :

$$P_j \equiv \psi_j \otimes \psi_j^\dagger + \psi'_j \otimes \psi'^{\dagger}_j \quad (2.34)$$

where \otimes means tensor product. The 2×2 Berry phase matrix $M_{f \leftarrow i}$ for the given parameter path is then obtained as

$$M_{f \leftarrow i} = \lim_{N \rightarrow \infty} R_f^\dagger P_N P_{N-1} \dots P_1 R_i \quad (2.35)$$

where $R_f = R_i$ since the path is closed.

By using a large enough N we found the converged $M_{f \leftarrow i}$ matrix has only diagonal elements being nonzero, meaning the braiding only changes each ground state by a scalar phase factor. Their values are $(M_{f \leftarrow i})_{00} = e^{i0.118\pi}$ and $(M_{f \leftarrow i})_{11} = e^{-i0.382\pi} = e^{i(0.118-0.5)\pi}$.

We end this section by noting that the parameter path considered for the 3-site Kitaev triangle above is not equivalent to rotating a staggered vector potential but to separately manipulating the Peierls phases along the three edges. We have also done calculations for the latter case and found the two lowest-energy states fail to be degenerate everywhere along the parameter path, leading to non-standard relative Berry phases between the two initial states.

Corner MZM in finite-width hollow triangles

A model that is closer to a realistic hollow triangular island is the finite-width triangular chain or ribbon. An example, illustrated in Figure 2.7 (d), has its edge length $L = 80$ and width $W = 3$. The Hamiltonian for a single ribbon parallel to $\hat{\mathbf{x}}$ is constructed and Fourier transformed in the way described in the main text and has the following block form up to a constant

$$\mathcal{H} = \frac{1}{2} \sum_k \Psi_k^\dagger \begin{pmatrix} h_t(k) & h_\Delta(k) \\ h_\Delta^\dagger(k) & -h_t^*(-k) \end{pmatrix} \Psi_k \quad (2.36)$$

where $\Psi_k \equiv (c_{k,1}, \dots, c_{k,W}, c_{-k,1}^\dagger, \dots, c_{-k,W}^\dagger)^T$. $h_t(k)$ is a $W \times W$ Hermitian tridiagonal matrix with $(h_t)_{n,n} = -2t \cos(k + \mathbf{A} \cdot \mathbf{a}_1) - \mu$ and $(h_t)_{n,n+1} = -t(e^{i(-k + \mathbf{A} \cdot \mathbf{a}_3)} + e^{i\mathbf{A} \cdot \mathbf{a}_2})$ (here $\mathbf{a}_3 \equiv -\mathbf{a}_1 + \mathbf{a}_2$). $h_\Delta(k)$ is a $W \times W$ tridiagonal matrix with $(h_\Delta)_{n,n} = -2i\Delta \sin k$ and $(h_\Delta)_{n,n\pm 1} = \mp \Delta \left[e^{-i(\pm k + \frac{2\pi}{3})} + e^{-i\frac{\pi}{3}} \right]$.

The phase diagram Fig. 2.6 (a) is created in a similar way as that in Fig. 3 (b) of the main text, assuming a constant vector potential along $\hat{\mathbf{y}}$ and infinitely long $W = 3$ ribbons. The spectral

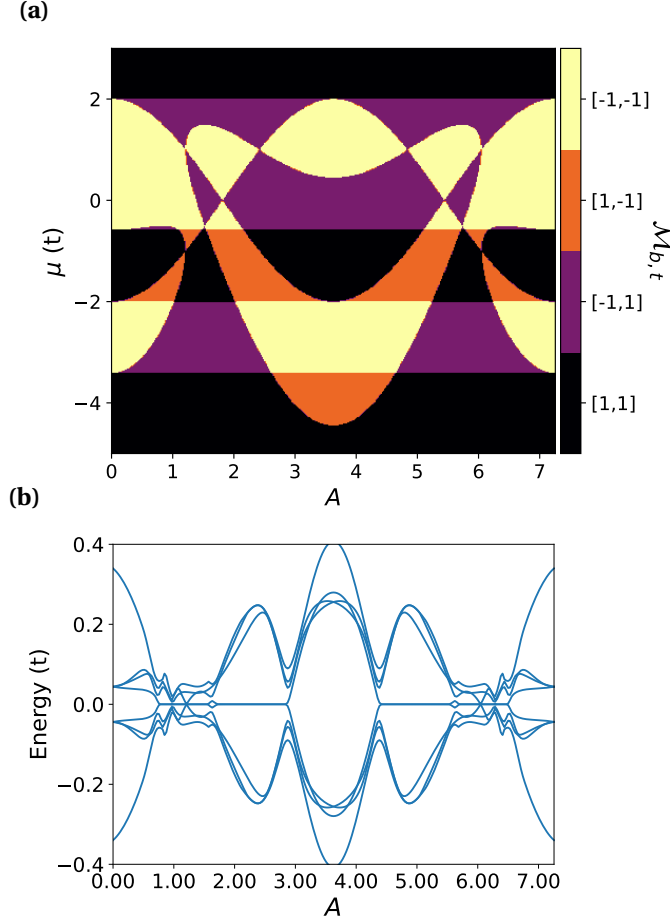


Figure 2.6: (a) Topological phase diagram for a $W = 3$ hollow triangle obtained by overlapping the $\mathcal{M}_{b,t}(A, \mu)$ plots of 1D chains with $\mathbf{A} = A\hat{\mathbf{y}}$ and $\mathbf{A} = A(\frac{\sqrt{3}}{2}\hat{\mathbf{x}} + \frac{1}{2}\hat{\mathbf{y}})$. Color scheme: purple— $[\mathcal{M}_b, \mathcal{M}_t] = [1, 1]$, yellow— $[\mathcal{M}_b, \mathcal{M}_t] = [-1, -1]$, red— $[\mathcal{M}_b, \mathcal{M}_t] = [-1, 1]$, orange— $[\mathcal{M}_b, \mathcal{M}_t] = [1, -1]$ (b) Near-gap BdG eigen-energies vs A for a finite triangle with edge length $L = 80$, $W = 3$, and $\mu = 1.6$.

flow for the actual triangle with $\mu = 1.6$ in Fig. 2.6 (b) shows MZM in the parameter regions in agreement with the phase diagram. Fig. 2.6. The MZM wavefunctions for $A = 0.83$ and $\mu = 1.6$, illustrated in Fig. 2.7 (d), are indeed well localized at the bottom corners.

We next discuss how to move the MZM on a hollow triangle by rotating the vector potential. Due to the Peierls phase accumulated by hopping that is not parallel with the finite-width ribbon edges, the vector potential has a more complex effect on the energy spectrum here than that for the $W = 1$ case. To ensure that the bulk band gap of individual edges only closes at a few isolated topological phase transition points, we plot in Figure 2.7 (b) the smallest gap of the three edges with periodic boundary condition versus (A, φ) when $\mu = 1.6$. A relatively clean

813 region can be identified when $A \in (0.75, 0.8)$. Further taking into account the topological phase
 814 diagram Fig. 2.7 (a) obtained in a similar way as Fig. 4 (a) in the main text, we chose a parameter
 815 path on the (A, φ) plane that linearly interpolates the following points:

$$(A, \varphi) = (0.83, 0) \rightarrow \left(0.77, \frac{\pi}{6}\right) \rightarrow \left(0.83, \frac{\pi}{3}\right) \rightarrow \left(0.77, \frac{\pi}{2}\right) \quad (2.37)$$

816 The phase diagram indicates that along this path, the nontrivial $\mathcal{M} = -1$ phase crawls through
 817 the three edges in a clockwise manner. Such a path ensures that only one edge undergoes a
 818 topological phase transition at a time. Then in the actual triangle the bulk gap will stay open
 819 due to finite size effect as a MZM moves across an edge without hybridizing with the other
 820 MZM.

821 To support this claim, we plot in Fig. 2.7 (c) the spectral flow for a finite triangle with $L = 80$,
 822 $W = 3$, $\mu = 1.6$ and the above parameter path. The bulk gap is indeed open throughout the
 823 path, and the degeneracy of the two MZM also stays intact. The wavefunctions of the MZM
 824 at representative points along the path are plotted in panels (d-g) in the same order as that
 825 marked in panel (c). The locations of the MZM are also consistent with that inferred from the
 826 topological phase diagram.

827 **Braiding MZM in a small network of triangles**

828 In this section we show that one can braid two out of four MZM, a minimal setting for non-
 829 trivial manipulation of the degenerate many-body ground states, by using a small network of
 830 corner-sharing triangles. We focus on the critical step of swapping γ_2 and γ_3 as labeled in Fig. 5
 831 of the main text. This can be done by rotating the vector potential of the triangle in the middle
 832 of the bottom row from $\varphi = \frac{\pi}{6}$ to $\frac{\pi}{3}$. More specifically, when $\varphi = \frac{\pi}{6}$, with the chosen values of μ
 833 and A , only the right edge of the said triangle is topologically nontrivial. The chain that hosts
 834 $\gamma_{3,4}$ thus extends through this nontrivial edge to the top triangle as in Fig. 2.8 (b). On the other
 835 hand, when φ increases to $\frac{\pi}{3}$, the nontrivial edge of the middle triangle changes from right to
 836 left, which leads to γ_2 hopping from its left corner to the right through the top corner, while γ_3

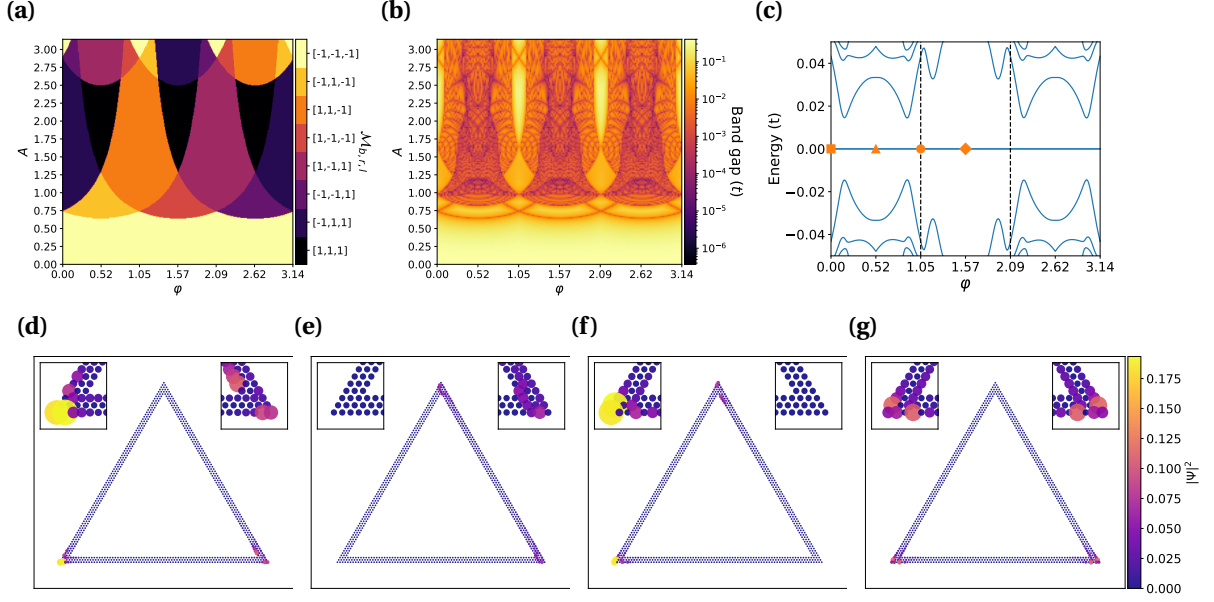


Figure 2.7: (a) Topological phase diagram for three $W = 3$ ribbons corresponding to the three edges of a hollow triangle. ($\mu = 1.6$ in all panels.) (b) Minimum of the bulk gaps of the three ribbons plotted on the (A, φ) plane. (c) Spectral flow of a hollow triangle with $W = 3$, $L = 80$, and the parameter path given in Eq. (2.37). (d-g) BdG eigenfunction $|\Psi|^2$ summed over the two zero modes at $\varphi = 0, \frac{\pi}{6}, \frac{\pi}{3}, \frac{\pi}{2}$, respectively.

is unaffected [Figs. 2.8 (c-g)]. As a result the γ_2, γ_3 swapping is done without closing the bulk gap, as can be seen from the spectral flow in Fig. 2.8 (a).

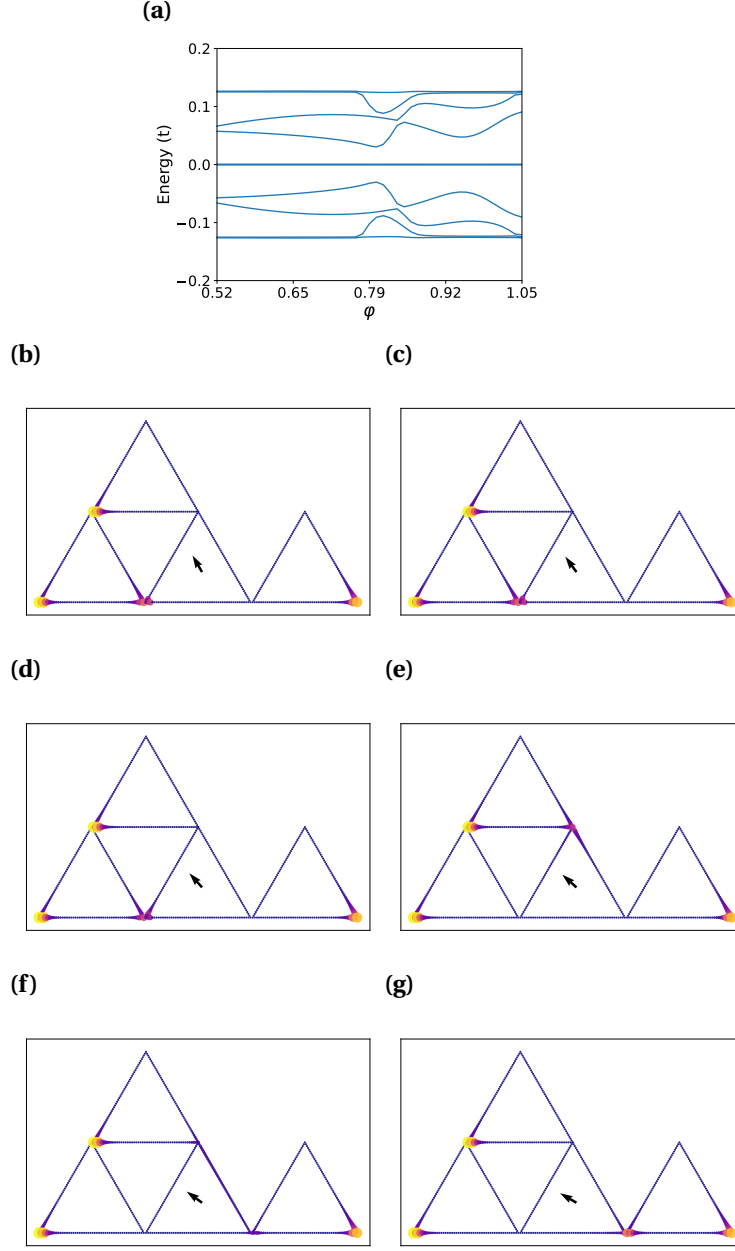


Figure 2.8: (a) Spectral flow for the critical step of swapping γ_2 and γ_3 in the example of Fig. 5 in the main text, calculated using four corner-sharing triangles of $W = 1$ and $L = 50$, with $\mu = 1.6$ and $A = 2.6$. Vector potential for the middle triangle in the bottom row can rotate according to $\mathbf{A} = A(-\sin\phi\hat{\mathbf{x}} + \cos\phi\hat{\mathbf{y}})$ from $\phi = \frac{\pi}{6}$ to $\frac{\pi}{3}$, while the other three have fixed $\phi = 0$. (b)-(g) BdG eigenfunction $|\Psi|^2$ summed over the four zero modes at equally-spaced points along the rotation path. The black arrow indicates the direction of the vector potential for the bottom middle triangle.

Chapter 3

Landau Level-Like Topological Floquet Hamiltonians

3.1 Introduction

The quantum Hall effect (QHE) in conventional two-dimensional electron gas (2DEG) is one of the most remarkable phenomena in condensed matter physics [72]. This effect is indeed associated with a uniform external perpendicular magnetic field, which splits the electron energy spectrum into discrete Landau levels (LLs). Subject to a strong magnetic field, the diagonal (longitudinal) electric conductivity is vanishingly small, while the nondiagonal (Hall) conductivity is quantized. This happens due to the fact that, when the Fermi energy lies in the gap between two LLs, it is referred to as integer QHE as the Hall conductivity takes values of $2(2n + 1)e^2/h$ with an integer n , being the number of bands below the Fermi energy [73]. Recent experimental realization of graphene has stimulated additional interest to explore QHE in two dimensional systems [73–75].

This significant effect is important to explore in Floquet systems [76, 77] because one may observe new phases in an alternative venue that can be experimentally realized [78–83]. Time periodically modulated Floquet theory has been extensively studied and well established for a large class of systems [77, 84–88]. Therefore, one may employ the high frequency expansions [77, 87–94] such as the well known Floquet-Magnus expansion [92–95] and Van Vleck expansion [77, 87]. The significant difference is the latter provides an explicit formula for the time evolution operator starting at initial time $t_0 = 0$ rather than former starting with finite time t_0 B.3. In such nonequilibrium systems, a circularly polarized laser light made topology nontrivial in spite of triviality in equilibrium [96]. This nontrivial topology is similar to the quantum Anomalous Hall effect proposed by Haldane [97]. Further, optical manipulation of matter is emerging as a promising way of exploring novel phases [98, 99]. This leads to Floquet-Bloch states exhibiting emerging physical properties that are otherwise inaccessible in equilib-

rium [100], i.e., the Floquet Chern insulator [101], Floquet topological insulators [102], Floquet notion of magnetic and other strongly-correlated phases [102], manipulation of topological antiferromagnet [103], topological classifications, symmetry-breaking concept, and symmetry protected topological phases in nonequilibrium quantum many-body systems [102, 104]. Furthermore, it is important to note that these studies have been demonstrated in the presence of time-periodic homogeneous laser lights. However, the application of spatially inhomogeneous [105–109] laser lights have not been considered so far to the best of our knowledge.

In this Letter, we unveil that QHE can be observed in Floquet systems without need of uniform magnetic field. We show that two linearly polarized lights are an effective and versatile way of realizing QHE either in graphene-like 2D systems or in conventional 2DEG. Additionally, at least one light needs be spatially inhomogeneous. Employing the Floquet theory, we rely on the standard degenerate perturbation formalism and use the Van Vleck expansion B.3 [77, 87]. Finally, to obtain the effective Hamiltonian and corresponding bandstructure, we employ the long wavelength limit for spatially inhomogeneous modulation, and use high-refractive index materials [110] to enhance the effective magnetic fields and energy bandstructure. We find our work provides new platforms for realizing QHE and related novel phases in nonequilibrium systems.

3.2 Floquet Landau level-like bands in Dirac systems

In this section we demonstrate a Dirac system in the presence of a standing non-uniform circularly polarized light becomes an effective Dirac Hamiltonian with a magnetic field that is composed of the electric field component of light. Dirac electrons can be represented with a generic model 2D Hamiltonian honeycomb monolayer in the presence of a gauge potential as

$$\mathcal{H}(t) = v_F \boldsymbol{\sigma} \cdot (\mathbf{p} + e\mathbf{A}(t)), \quad (3.1)$$

where \mathbf{A} is the gauge potential, \mathbf{p} is the momentum operator, v_F is the Fermi velocity of Dirac fermions, e is electron charge, and $\boldsymbol{\sigma}$ the Pauli matrices vector in 2D. The light is made of three

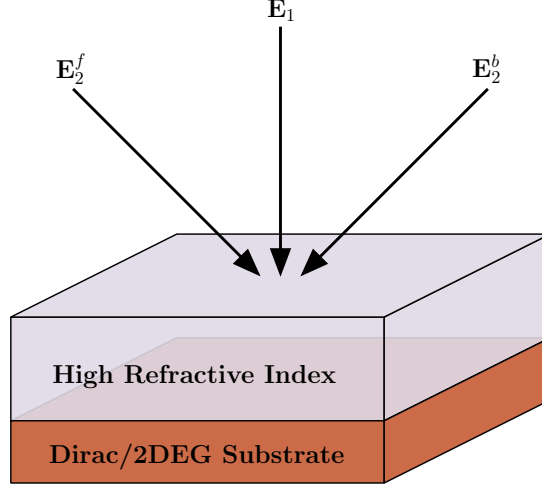


Figure 3.1: Schematic of two oblique (forward and backward) and one normal incident light on graphene or a 2DEG substrate with high refractive index material on top. Oblique lasers have polarization in y -axis and travel in xz -plane and normal incidence laser has polarization in the x -axis and travel in yz -plane. With beam width large enough to cover the device fully.

linearly polarized laser lights, as shown in Fig. 3.1. Where the first is normally incident in the z -axis with polarization in the x -axis. The second and third are of oblique incidence in the xz -plane, to acquire non-uniformity in the x -axis, with polarization in the y -axis, and mirrored about the yz -plane. This is to introduce x -dependence with the p_y term of the Dirac Hamiltonian. The relevant electric field components at the Dirac system interface are

$$\mathbf{E}_1 = E \cos \omega t \hat{\mathbf{x}},$$

$$\mathbf{E}_2 = \mathbf{E}_2^f + \mathbf{E}_2^b = E \sin(Kx) \sin 2\omega t \hat{\mathbf{y}}, \quad (3.2)$$

Where ω is angular frequency of light with time t and $K = \omega \sin(\theta_i)/v_p$, with θ_i as incident angle of oblique light and v_p is phase velocity of light. Notice, the second electric field has twice frequency of the first, this allows for the second gauge potentials σ_y to have non-zero commutation with the first gauge potentials σ_x , and due to the high-frequency expansion used

897 later, allows for the second gauge potential to return to a σ_y , as seen in B.4.1. This form of the
 898 electric field relates to the following gauge potential, via $\mathbf{E} = -\partial_t \mathbf{A}$ as

$$\mathbf{A}(t) = \frac{E}{\omega} \langle -\sin \omega t, \frac{1}{2} \sin(Kx) \cos 2\omega t \rangle, \quad (3.3)$$

899 Substituting Eq. (3.3) into Eq. (3.1), we arrive at

$$\mathcal{H}(t) = \mathcal{H}_0 - \sigma_x \frac{v_F e E}{\omega} \sin \omega t - \sigma_y \frac{v_F e E}{2\omega} \sin(Kx) \cos 2\omega t, \quad (3.4)$$

900 where $\mathcal{H}_0 = v_F \boldsymbol{\sigma} \cdot \mathbf{p}$. Due to the laser light's time-translation symmetry through $A(t+T) = A(t)$
 901 with $T = 2\pi/\omega$, one can apply the Floquet theory [66,77,87] and obtain an effective Hamiltonian
 902 from Eq. (3.4). This introduces the quasienergy matrix $Q_{m,m+n} = H_n + m\hbar\omega\delta_{n0}$ after performing
 903 the Fourier time-transform of the Hamiltonian, given as

$$H_n = \frac{1}{T} \int_0^T \mathcal{H}(t) e^{-in\omega t} dt, \quad (3.5)$$

904 then we are left with modes $m = 0, \pm 1, \pm 2$. To use the high-frequency approximation we require
 905 $\hbar\omega \gg H_{\pm 1, \pm 2}$, the off-diagonal terms. After applying the high-frequency approximation to first
 906 and second order expansion in $\hbar\omega$, it leads to the zeroth-mode effective Hamiltonian in Eq. (3.4)
 907 as

$$H_{\text{eff}} = H_0 - \sigma_y \frac{v_F^3 e^2 E^2 p_y}{\hbar^2 \omega^4} + \sigma_y \frac{v_F^3 e^3 E^3 \sin(Kx)}{4\hbar^2 \omega^5} - \sigma_x \frac{v_F^3 e^2 E^2 \{p_x, \sin^2(Kx)\}}{8\hbar^2 \omega^4}. \quad (3.6)$$

908 The derivation can be found in the Appendix B.4.1. In Eq. (3.6), the first order term in $\hbar\omega$ leads
 909 to gap at the Dirac point in normally incident circularly polarized light experiments [79,81] and
 910 is zero here due to the non-uniformity nature of incident laser lights. This effective Hamiltonian
 911 can be simplified in the long wavelength limit, $Kx \ll 1$ to

$$\mathcal{H}_{\text{eff}}^D = v_F \sigma_x p_x + v_F \sigma_y (C p_y + e B^D x), \quad (3.7)$$

where $C = 1 - \left(\frac{v_F e E}{\hbar \omega^2}\right)^2$ and $B^D = \frac{K v_F^2 e^2 E^3}{4 \hbar^2 \omega^5}$. In accordance with Eqs. (3.6) and (3.7), there is least anisotropy in the Dirac spectrum in addition to zero gap. Diagonalizing the Hamiltonian in Eq. (3.7), we obtained the eigenvalues for Dirac system as

$$\epsilon_n^D = \pm v_F^2 \sqrt{\frac{n K e^3 E^3}{2 \hbar \omega^5}} \quad (3.8)$$

which is similar to graphene LLs spectrum in the limit of equal velocities. The effective magnetic field in the Dirac Hamiltonian achieves a highly degenerate energy spectrum similar to LLs. From a classical point of view we call this a LL-like spectrum, the difference being electrons are not necessarily in cyclotron orbits but orbits, potentially more complicated, due to CPL producing a Coulumb force in the material's 2D plane.

There are several ways to enhance the effective magnetic field and directly LL-like energies for a Dirac system. Electric field strength can be increased within reason as we are limited by the photon energy to ensure the high-frequency expansion holds, $E \ll 2 \hbar \omega^2 / e v_F$, one can reasonably use electric field strengths up to 20% of the limit due to photon energy. The lights wavenumber $K = \omega \sin(\theta_i) / v_p$ has a linear relationship to photon energy, too. Overall, considering the high-frequency limit on the electric field, the effective field $B^D \propto \omega^2 \sin(\theta_i) / (v_F v_p)$. Increasing photon energy is one way to enhance the effective magnetic field. As considered in previous literature, when photon energy and electric field are increased more energy is pumped into the system, shorter pulses are required to prevent damaging the system [79, 81]. Without too much consequence the incident angle can be increased up to $\pi/2$ and decreasing the phase velocity of light would enhance the effective magnetic field.

3.3 Floquet Landau level-like bands in 2DEG systems

In this section show a 2DEG system with a non-uniform circularly polarized light becomes an effective 2DEG Hamiltonian with a magnetic field that is composed of the electric field component of light. We consider the case of Schrodinger charged particles in the presence of a gauge potential as

$$\mathcal{H}(t) = \frac{1}{2m^*} (\mathbf{p} + e\mathbf{A}(t))^2 \quad (3.9)$$

where m^* is the effective charge mass. As before, the light is made of three linearly polarized laser lights. The relevant electric field components at the 2DEG interface are

$$\begin{aligned} \mathbf{E}_1 &= E \cos \omega t \hat{\mathbf{x}}, \\ \mathbf{E}_2 &= \mathbf{E}_2^f + \mathbf{E}_2^b = -E \cos(Kx) \sin \omega t \hat{\mathbf{y}}. \end{aligned} \quad (3.10)$$

In this case both lights have same frequency of light, here there are no pauli matrices to account for, we can get non-zero commutations from the x and p_x terms during the high-frequency expansion. In this case both lights have the same frequency of light, this is a requirement to make the 2DEG Hamiltonian into a Landau level-like Hamiltonian. This form of the electric field relates to the following gauge potential, via $\mathbf{E} = -\partial_t \mathbf{A}$ as

$$\mathbf{A}(t) = \frac{E}{\omega} \langle -\sin \omega t, \cos(Kx) \cos \omega t \rangle. \quad (3.11)$$

Substituting Eq. (3.11) into Eq. (3.9), we arrive at

$$\begin{aligned} \mathcal{H}(t) &= \frac{1}{2m^*} \left[p_x^2 + p_y^2 + \frac{e^2 E^2}{2\omega^2} (1 - \cos 2\omega t) + \frac{e^2 E^2}{2\omega^2} (1 + \cos 2\omega t) \cos^2(Kx) \right. \\ &\quad \left. + \frac{2eE}{\omega} (p_y \cos(Kx) \cos \omega t - p_x \sin \omega t) \right]. \end{aligned} \quad (3.12)$$

Again, due to laser light's time-translation symmetry we can apply the Floquet theory, which includes computing the Fourier time-transform using Eq. (3.5). This leaves us with modes $m = 0, \pm 1, \pm 2$. In the high-frequency expansion we still require $\hbar\omega \gg H_{\pm 1, \pm 2}$. After applying the high-frequency approximation to first order in $\hbar\omega$, it leads to the zeroth-mode effective Hamiltonian as

$$\mathcal{H}_{\text{eff}} = \frac{1}{2m^*} \left[p_x^2 + p_y^2 + \frac{e^2 E^2}{\omega^2} (1 + \cos^2(Kx)) - \frac{2Ke^2 E^2 p_y \sin(Kx)}{m^* \omega^3} \right]$$

$$\mathcal{H}_{\text{eff}} = \frac{1}{2m^*} \left[p_x^2 + \left(p_y - \frac{Ke^2 E^2 \sin(Kx)}{m^* \omega^3} \right)^2 + \frac{e^2 E^2 \cos^2(Kx)}{\omega^2} - \frac{K^2 e^4 E^4 \sin(Kx)}{m^{*2} \omega^6} \right].$$

where we shifted the constant energy out of the effective Hamiltonian and completed the square for the p_y and x terms. Here we can see the high-frequency expansion terms $H^{F(1)}$ and $H^{F(2)}$, as shown in B.3, introduce a periodic potential in the x -direction, this can be cancelled out by applying an external periodic potential of the same strength and wavenumber in the x -direction. Finally, in the long wavelength, $Kx \ll 1$,

$$\mathcal{H}_{\text{eff}}^{2\text{DEG}} = \frac{1}{2m^*} \left[p_x^2 + (p_y - eB^{2\text{DEG}}x)^2 \right], \quad (3.13)$$

with $B^{2\text{DEG}} = \frac{K^2 e E^2}{m^* \omega^3}$. The energy spectrum values are

$$\epsilon_n^{2\text{DEG}} = \frac{\hbar K^2 e^2 E^2}{m^{*2} \omega^3} \left(n + \frac{1}{2} \right), \quad (3.14)$$

which is similar to 2DEG LLs spectrum. This is another highly degenerate LL-like spectrum due to an effective magnetic field induced by the combination of laser lights provided.

The 2DEG system has the same ways to enhance its effective magnetic field and energy spectrum. First, the electric field is limited by the high-frequency expansion, we find $E \ll (8m^* \hbar \omega^3 / e^2)^{1/2}$ to be a reasonable cutoff. The effective field, $B^{2\text{DEG}} \propto \omega^2 \sin^2(\theta_i) / v_p^2$, is similar to the Dirac system. Again, increasing the photon energy is one way to enhance the effective

magnetic field, with the requirement of using shorter pulses as photon energy and electric field increase. In 2DEG systems, the enhancement to effective magnetic field due to incident angle and phase velocity is squared compared to the Dirac case having a product of Fermi velocity and phase velocity.

3.4 Discussion and conclusion

We now examine the topology of both systems. Eqs. (3.7) and (3.13) are in LL Hamiltonian form, and typically would exhibit QHE. The two systems only have translational symmetry in the y -axis, so a Chern number based on periodicity in k_x and k_y is not applicable, though one can relate the center of mass of an electron to the Chern number as shown in Appendix B.7, which is related to the Laughlin pump. Considering the Laughlin pump argument, both systems have quantized Hall conductivity, since both have the same eigenstates as their respective LL Hamiltonian. A key difference to note about both systems is the C term in Eq. (3.7). This term will stay positive for the values of E used in the high-frequency limit for the Dirac case.

Using existing experiments [79, 81] we can provide an estimate for the strength of the effective magnetic field to observe LL-like spectrum and QHE. Analytical structure of Eq. (3.8) and Eq. (3.14) is primarily responsible for the LL-like spectrum in both the Dirac and 2DEG systems, respectively. Although such results are valid for other 2D materials or Schrödinger systems, however, for simplicity, we will consider parameters realized for graphene or topological insulators [79, 81]. We will consider a similar range of mid-IR photon energies (or $\lambda = [3\mu\text{m}, 10\mu\text{m}]$) as seen in graphene or topological insulators [79, 81] to match with recently proposed high refractive index metamaterial composites [110]. In these experiments [79, 81], the strength of the electric field used is 1×10^7 V/m to 1×10^8 V/m, for the parameters used to estimate effective magnetic fields for both systems the largest electric field is around 1.4×10^8 V/m. As should be considered, the larger both photon energy and electric field become ultrafast pulses should be used to prevent thermal damage to materials, on the order of 500 fs. To note, for the following results we assume a high oblique angle to let $\sin(\theta_i) \approx 1$.

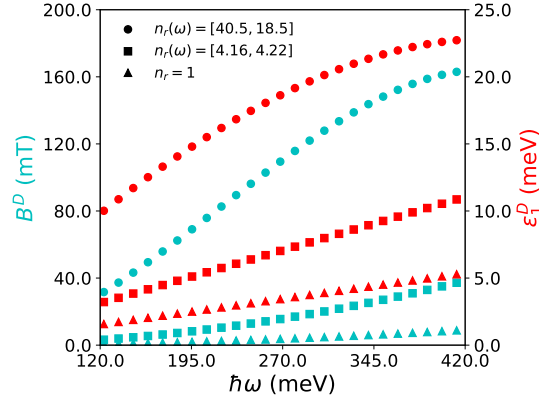


Figure 3.2: Effective magnetic field (cyan) and first quasienergy (red) as a function of photon energy for various refractive materials: vacuum (triangles), germanium (squares), and Al-composite metamaterial (circles).

To enhance the effective magnetic field, aside from using higher photon energy, reducing the photon phase velocity can see a considerable increase for both systems. The refractive index materials can be set above graphene, or any Dirac material, such that the laser light can travel through to reduce its phase velocity. Germanium refractive index increases monotonically with increasing photon energy, we use a linear interpolation of the refractive index due the small change for the range of photon energies used. Al-composite metamaterials are monotonically decreasing with increasing photon energy, the data is roughly linear and we use a linear interpolation for it as well.

In case of a Dirac system Fig. 3.2 shows graphene with various refractive index materials to enhance the effective magnetic field and first order quasienergy of the LL-like spectrum. For mid-IR ranges of laser light, the effective magnetic field (cyan) can get up to 8.8 mT for vacuum, 37.2 mT for germanium, and 163 mT for Al-composite metamaterial for $\hbar\omega = 413$ meV and results in first order quasienergies (red) of 5.3 meV, 11 meV, and 23 meV, respectively. As can be seen in 3.2 as photon energy increases the Al-composite refractive index decreases quite a bit and if we used higher energy we would see the effective magnetic field and quasienergies start to decrease, as will be seen with 2DEG. While the material has higher index of refraction overall, it would be better to find a material that increases refractive index with photon energy,

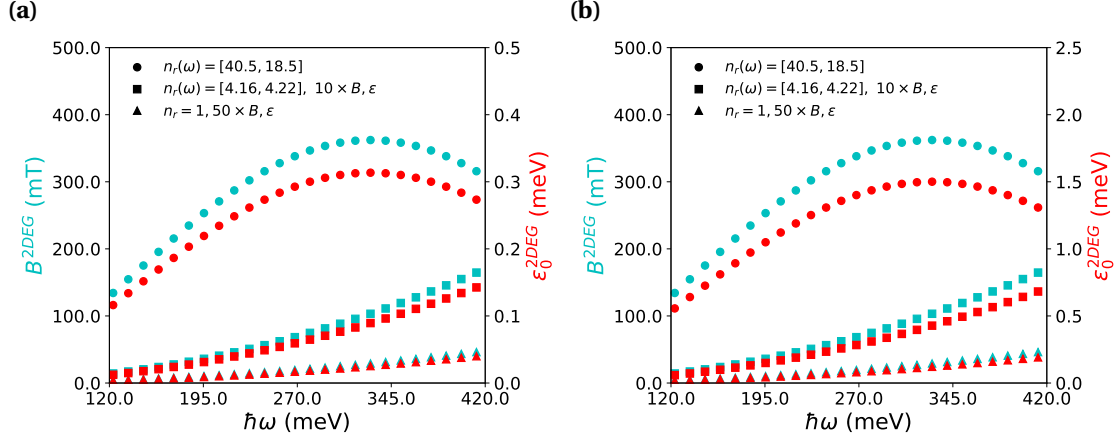


Figure 3.3: Effective magnetic field (cyan) and first quasienergy (red) as a function of photon energy for 2DEGs for various refractive materials: vacuum (triangles) scaled by a factor of 50, germanium (squares) scaled by a factor of 10, and Al-composite metamaterials. The 2DEG materials used are (a) GaAs and (b) InSb.

like germanium can, for it can drastically increase for slightly higher photon energies before effective magnetic field dips [111].

For 2DEG systems Fig. 3.3 shows GaAs and InSb materials with the same refractive materials used for graphene to enhance effective magnetic field and zeroth order quasienergy of the LL-like spectrum. The vacuum and germanium interfaces are scaled up by a factor of 10 and 50, respectively, to visually enhance and compare it to the Al-composite interface. GaAs is used as it is one of the most common 2DEG with relatively small effective electron mass, followed by InSb since it has the smallest effective electron mass found in 2DEG materials. For the GaAs system, effective magnetic field (cyan) can get up to 0.92 mT for vacuum, 16.5 mT for germanium, and 362 mT for Al-composite metamaterial and achieves zeroth order quasienergies (red) of $0.8 \mu\text{eV}$, $14.3 \mu\text{eV}$, and $314 \mu\text{eV}$, respectively. In the InSb system, effective magnetic field is the same as GaAs, since it has no dependence on effective mass, and achieves zeroth order quasienergies (red) of $3.8 \mu\text{eV}$ for vacuum, $68.2 \mu\text{eV}$ for germanium, and 1.5 meV for Al-composite. As alluded to earlier, due to Al-composites large decrease in refractive index for increasing photon energy, it peaks earlier around $\hbar\omega = 328$ mT, for 2DEG. Overall, we see large changes in 2DEG for both

effective magnetic field, due to being proportional to refractive index squared and quasienergies, being inversely proportional to effective electron mass.

There are a few items we did not consider for our calculations. First, we do not consider any effects due to a refractive index material in contact with a Dirac or 2DEG system. Secondly, while the high-frequency expansion limits the electric field applied to the materials one could still go beyond the limit of $\hbar\omega \ll H_{pm1}, H_{\pm 2}$ to enhance the effective magnetic field by a few orders of magnitude with some error. For example, if instead we use $\hbar\omega = H_{\pm 1}, H_{\pm 2}$, this would be multiplying the electric field by a factor of 5 from our calculations presented, Dirac effective magnetic field would increase by a factor of 125 while 2DEG effective magnetic field would increase by a factor of 25. For Dirac systems with higher electric field strengths, if $C = 0$, there would be no QHE as there is no coupling between x and p_y , and if $C < 0$, the direction of chirality flips.

In conclusion, we have shown Floquet LLs and the QHE using two linearly polarized lights for graphene-like 2D and conventional 2DEG systems. While using these laser lights, we need at least one or both polarized lights to be spatially inhomogeneous. We have presented results using frequency space expansion method and degenerate Floquet perturbation theory. While, a tight-binding model capable of using “low-frequency” with a Peierls substitution can be found in appendix B.5 and B.6, the results are difficult to interpret and currently not informative. The results agree well to show Floquet LL-like energies in experimentally accessible parameters range. Also, it is vital to note we are flexible to use different values of the electric field strength, photon energy, or phase velocity to realize QHE and control the strength of the effective magnetic field. Therefore, we believe that Floquet LL-like and QHE can be observed in the experiments for moderate strength of the spatially inhomogeneous lights. Moreover, we expect the potential to host new nano-electronics in nonequilibrium systems.

Chapter 4

Conclusion

In this dissertation, we focused on using gauge potentials as a key mechanism for tuning systems from trivial topology to non-trivial topology. One can either use minimal coupling to introduce a gauge potential in a continuum model or a Peierls substitution which is more commonly used in a tight-binding model. Both approaches are equivalent for slowly varying gauge potentials. This lends a lot of flexibility in tackling a Hamiltonian in either form, continuum or tight-binding. Another key aspect of gauge potentials is gauge invariance under a gauge transform. This allows us to transform a Hamiltonian into a basis that is easier to spot the physics we are interested in and determine its eigenmodes.

In Chapter 2, we showed through a Peierls substitution of a gauge potential in a superconducting tight-binding model in Majorana basis allows one to achieve non-trivial topology. We showed for a three lattice superconducting equilateral triangle one can apply a gauge potential as a step function exactly solves the Hamiltonian to have two Majorana fermions on two of the triangles three vertices. With a rotation of the gauge potential via a linear interpolation, we can keep the band gap from closing and rotate one Majorana fermion at a time to the next vertex. Then, for larger triangular islands, as a chain or with finite thick edges, we can use bulk-edge correspondence to inform us which edge is trivial and non-trivial. Using a uniform gauge potential across the triangle showed due to geometry and gauge potentials contribution through a Peierls phase individuals edges topology could be tuned on and off. The phase diagrams showed there are swaths of tunable parameters to then make the topology crawl cw or ccw, without band gap closing, around the triangular island, effectively rotating two Majorana fermions around a triangle. With two options for hosting and rotating Majorana fermions we finally showed a minimal network of triangles to host and braid 4 Majorana fermions, and can be upscaled from there. This opens up new routes to achieve fault-tolerant (topological) quantum computing.

1067 In Chapter 3, we showed through minimal coupling of a gauge potential, created from laser
1068 light, to both a Dirac system and 2DEG system one can induce LL-like spectrum and QHE. This
1069 used Floquet theory and high-frequency expansion, and allows us to approximate an effective
1070 magnetic field as a function of electric field and arrive a LL-like Hamiltonians, to which we
1071 know the physics of in equilibrium systems. There are many tunable parameters to enhance
1072 the LL-like spectrum and QHE, from photon energy, electric field, phase velocity, incidence
1073 angle, to Fermi velocity or effective electron mass. The estimated values are achievable with
1074 current setups found in previous literature and comparable with classic magnetic field QHE.
1075 This avenue opens up new frontiers in nonequilibrium physics.

1076 **Appendix A**

1077 **Superconducting Triangular Islands**

1078 **A.1 Kitaev chain**

1079 A pair of Majorana fermions can be defined in terms of spinless operators a_j, a_j^\dagger , where j
1080 labels general quantum numbers, as

$$c_{2j-1} = a_j + a_j^\dagger \tag{A.1}$$

$$c_{2j} = -i(a_j - a_j^\dagger)$$

1081 which are hermitian conjugates of themselves. Conversely,

$$a_j = \frac{1}{2}(c_{2j-1} + i c_{2j}), \tag{A.2}$$

$$a_j^\dagger = \frac{1}{2}(c_{2j-1} - i c_{2j})$$

1082 For a general mean-field Hamiltonian

$$H = \sum_{jl} h_{jl} a_j^\dagger a_l \tag{A.3}$$

1083 where h is a Hermitian matrix, it can be transformed to the Majorana fermion representation
 1084 as follows:

$$\begin{aligned}
 H &= \frac{1}{4} \sum_{jl} h_{jl} (c_{2j-1} - i c_{2j}) (c_{2l-1} + i c_{2l}) \\
 &= \frac{1}{4} \sum_{jl} (h_{jl} c_{2j-1} c_{2l-1} - i h_{jl} c_{2j} c_{2l-1} + i h_{jl} c_{2j-1} c_{2l} + h_{jl} c_{2j} c_{2l}) \\
 &= \frac{i}{4} \sum_{jl} (c_{2j-1}, c_{2j}) \begin{pmatrix} -i h_{jl} & h_{jl} \\ -h_{jl} & -i h_{jl} \end{pmatrix} \begin{pmatrix} c_{2l-1} \\ c_{2l} \end{pmatrix} \\
 &\equiv \frac{i}{4} \sum_{mn} A_{mn} c_m c_n
 \end{aligned} \tag{A.4}$$

1085 where the matrix A anti-Hermitian since

$$H^\dagger = -\frac{i}{4} \sum_{mn} A_{mn}^* c_n c_m = H \tag{A.5}$$

1086 which leads to $A_{mn}^* = -A_{nm}$. If the Hamiltonian does not preserve particle number, i.e., it is a
 1087 BdG Hamiltonian, we have, similarly

$$H = \sum_{jl} \left(h_{jl} a_j^\dagger a_l + \Delta_{jl} a_j a_l + \Delta_{jl}^\dagger a_j^\dagger a_l^\dagger \right) \tag{A.6}$$

1088 supposing we do not double count the terms in the normal part of the Hamiltonian. Then

$$H = \frac{i}{4} \sum_{jl} (c_{2j-1}, c_{2j}) \begin{pmatrix} -i h - i(\Delta + \Delta^\dagger) & h + (\Delta - \Delta^\dagger) \\ -h + (\Delta - \Delta^\dagger) & -i h + i(\Delta + \Delta^\dagger) \end{pmatrix}_{jl} \begin{pmatrix} c_{2l-1} \\ c_{2l} \end{pmatrix} \tag{A.7}$$

1089 On the other hand, the BdG Hamiltonian can be written as

$$\begin{aligned}
H &= \frac{1}{2} \sum_j h_{jj} + \sum_{jl} \left(\frac{1}{2} h_{jl} a_j^\dagger a_l - \frac{1}{2} h_{lj} a_j a_l^\dagger + \Delta_{jl} a_j a_l + \Delta_{jl}^\dagger a_j^\dagger a_l^\dagger \right) \\
&= \frac{1}{2} \text{Tr}(h) + \sum_{jl} (a_j^\dagger, a_j) \begin{pmatrix} \frac{1}{2} h & \Delta^\dagger \\ \Delta & -\frac{1}{2} h^T \end{pmatrix}_{jl} \begin{pmatrix} a_l \\ a_l^\dagger \end{pmatrix} \\
&\equiv \frac{1}{2} \text{Tr}(h) + a^\dagger \begin{pmatrix} \frac{1}{2} h & \Delta^\dagger \\ \Delta & -\frac{1}{2} h^T \end{pmatrix} a
\end{aligned} \tag{A.8}$$

1090 where $a \equiv (a_1, a_2, \dots, a_1^\dagger, a_2^\dagger, \dots)^T$. Suppose the BdG Hamiltonian can be diagonalized by a Bo-
1091 goliubov transformation:

$$\begin{aligned}
\tilde{a}_j^\dagger &= a_l^\dagger U_{1,lj} + a_k U_{2,kj} \\
\tilde{a}_j &= a_l U_{1,lj}^* + a_k^\dagger U_{2,kj}^*
\end{aligned} \tag{A.9}$$

1092 Preserving the anticommutation relation suggests

$$\begin{aligned}
\delta_{ij} &= \{\tilde{a}_i, \tilde{a}_j^\dagger\} = \{a_l U_{1,li}^* + a_k^\dagger U_{2,ki}^*, a_{l'}^\dagger U_{1,l'j} + a_{k'} U_{2,k'j}\} \\
&= U_{1,li}^* U_{1,l'j} + U_{2,ki}^* U_{2,k'j} = (U_1^\dagger U_1 + U_2^\dagger U_2)_{ij} \\
0 &= \{\tilde{a}_i, \tilde{a}_j\} = \{a_l U_{1,li}^* + a_k^\dagger U_{2,ki}^*, a_{l'} U_{1,l'j} + a_{k'}^\dagger U_{2,k'j}^*\} \\
&= U_{1,li}^* U_{2,l'j} + U_{2,ki}^* U_{1,k'j} = (U_1^\dagger U_2^* + U_2^\dagger U_1^*)_{ij} \\
0 &= \{\tilde{a}_i^\dagger, \tilde{a}_j^\dagger\} = \{a_l^\dagger U_{1,li} + a_k U_{2,ki}, a_{l'}^\dagger U_{1,l'j} + a_{k'} U_{2,k'j}\} \\
&= U_{1,li} U_{2,l'j} + U_{2,ki} U_{1,k'j} = (U_1^\dagger U_2^* + U_2^\dagger U_1^*)_{ij}^*
\end{aligned} \tag{A.10}$$

1093 The above identities simply indicate

$$\mathcal{U} \equiv \begin{pmatrix} U_1 & U_2 \\ U_2^* & U_1^* \end{pmatrix} \quad (\text{A.11})$$

1094 is a unitary matrix. Therefore one can diagonalize the BdG Hamiltonian using usual unitary
1095 matrices obtained from the eigenvectors of the matrix in the last line of Eq. A.75:

$$\begin{aligned} H &= \frac{1}{2} \text{Tr}(h) + \tilde{a}^\dagger U^\dagger \begin{pmatrix} \frac{1}{2}h & \Delta^\dagger \\ \Delta & -\frac{1}{2}h^T \end{pmatrix} U \tilde{a} \\ &\equiv \frac{1}{2} \text{Tr}(h) + \frac{1}{2} \tilde{a}^\dagger \begin{pmatrix} \epsilon & 0 \\ 0 & -\epsilon \end{pmatrix} \tilde{a} \\ &= \frac{1}{2} \sum_j h_{jj} + \frac{1}{2} \sum_j (\epsilon_j \tilde{a}_j^\dagger \tilde{a}_j - \epsilon_j \tilde{a}_j \tilde{a}_j^\dagger) \\ &= \frac{1}{2} \sum_j h_{jj} + \sum_j \epsilon_j (\tilde{a}_j^\dagger \tilde{a}_j - \frac{1}{2}) \end{aligned} \quad (\text{A.12})$$

1096 where $\epsilon \equiv \text{Diag}[\epsilon_1, \epsilon_2, \dots]$. To see why U can transform the BdG Hamiltonian into such a diag-
1097 onal matrix with opposite eigenvalues at the same positions in the upper-left and lower-right
1098 blocks, we check these two terms explicitly

$$\begin{aligned} &\frac{1}{2} (\epsilon_1 \tilde{a}_j^\dagger \tilde{a}_j - \epsilon_2 \tilde{a}_j \tilde{a}_j^\dagger) \\ &= \frac{\epsilon_1}{2} (a_l^\dagger U_{1,lj} + a_k U_{2,kj}) (a_{l'} U_{1,l'j}^* + a_{k'}^\dagger U_{2,k'j}^*) - \frac{\epsilon_2}{2} (a_{l'} U_{1,l'j}^* + a_{k'}^\dagger U_{2,k'j}^*) (a_l^\dagger U_{1,lj} + a_k U_{2,kj}) \\ &= \frac{1}{2} (\epsilon_1 U_{1,lj} U_{1,l'j}^* - \epsilon_2 U_{2,lj}^* U_{2,l'j}) a_l^\dagger a_{l'} + \frac{1}{2} (\epsilon_1 U_{2,kj} U_{2,k'j}^* - \epsilon_2 U_{1,kj}^* U_{1,k'j}) a_k a_{k'}^\dagger \\ &+ \frac{1}{2} (\epsilon_1 U_{1,lj} U_{2,k'j}^* - \epsilon_2 U_{2,lj}^* U_{1,k'j}) a_l^\dagger a_{k'}^\dagger + \frac{1}{2} (\epsilon_1 U_{2,kj} U_{1,l'j}^* - \epsilon_2 U_{1,kj}^* U_{2,l'j}) a_k a_{l'} \end{aligned} \quad (\text{A.13})$$

1099 Comparing them with the original BdG Hamiltonian Eq. A.75, we can conclude that

$$\epsilon_1 U_{1,lj} U_{1,l'j}^* - \epsilon_2 U_{2,lj}^* U_{2,l'j} = -(\epsilon_1 U_{2,l'j} U_{2,lj}^* - \epsilon_2 U_{1,l'j}^* U_{1,lj}) \quad (\text{A.14})$$

$$\epsilon_1 U_{1,lj} U_{2,k'j}^* - \epsilon_2 U_{2,lj}^* U_{1,k'j} = (\epsilon_1 U_{2,k'j} U_{1,lj}^* - \epsilon_2 U_{1,k'j}^* U_{2,lj})^*$$

1100 or equivalently

$$(\epsilon_1 - \epsilon_2)(U_{1,lj} U_{1,l'j}^* + U_{2,l'j} U_{2,lj}^*) = 0 \quad (\text{A.15})$$

$$0 = 0$$

1101 The first equation therefore dictates $\epsilon_1 = \epsilon_2$. However, note that ϵ_j does not have to be all posi-
1102 tive. If the original normal state Hamiltonian can be diagonalized into a form

$$H = \sum_j \tilde{\epsilon}_j b_j^\dagger b_j \quad (\text{A.16})$$

1103 where $\tilde{\epsilon}_j$ can be either positive or negative, the state with the lowest possible energy from the
1104 system is

$$|\Omega\rangle = \prod_{\tilde{\epsilon}_k < 0} b_k^\dagger |0\rangle \quad (\text{A.17})$$

1105 where $|0\rangle$ is the true vacuum with no particles in any sense. This is the ground state, and its
1106 parity is therefore determined by the number of single-particle eigenstates that have negative
1107 energies.

1108 From the same perspective, one can define the ground state of the BdG Hamiltonian Eq. A.12
1109 for a specific set of Fermion operators \tilde{a}_j , as

$$|\Omega_{\text{BdG}}\rangle = \prod_{\epsilon_j < 0} \tilde{a}_j^\dagger |0_{\text{BdG}}\rangle \quad (\text{A.18})$$

1110 where $|0_{\text{BdG}}\rangle$ is certain “vacuum state” for the given set of \tilde{a}_j :

$$\tilde{a}_j |0_{\text{BdG}}\rangle = 0, \forall j \quad (\text{A.19})$$

1111 The number of particles in the ground state is therefore determined by the number of negative
 1112 ϵ_j . However, the sign of ϵ_j in the present case does not have absolute meaning. For example,
 1113 supposing $\epsilon_{j_0} < 0$, the following Bogoliubov transformation

$$\tilde{a}'_{j_0} = \tilde{a}_{j_0}^\dagger \quad (\text{A.20})$$

$$\tilde{a}_{j_0}'^\dagger = \tilde{a}_{j_0}$$

1114 that only interchanges the creation and annihilation operators for a single j_0 and keeps the
 1115 others unchanged, leads to a different ground state

$$|\Omega'_{\text{BdG}}\rangle = \prod_{\epsilon_j < 0, j \neq j_0} \tilde{a}_j^\dagger |0_{\text{BdG}}\rangle \quad (\text{A.21})$$

1116 since the number of negative energy eigenstates decreases by one. The transformation in Eq. A.20
 1117 therefore neither preserves particle number nor particle parity. This can be explicitly checked.
 1118 The particle number operator in the \tilde{a}_j representation is

$$N = \sum_j \tilde{a}_j^\dagger \tilde{a}_j \quad (\text{A.22})$$

1119 Therefore

$$N' = \sum_{j \neq j_0} \tilde{a}_j^\dagger \tilde{a}_j + \tilde{a}_{j_0} \tilde{a}_{j_0}^\dagger = N + (1 - 2\tilde{a}_{j_0}^\dagger \tilde{a}_{j_0}) \quad (\text{A.23})$$

1120 The latter equation also means that when the j_0 state is occupied in Ω_{BdG} , i.e., $\tilde{a}_{j_0}^\dagger \tilde{a}_{j_0} |\Omega_{\text{BdG}}\rangle =$
 1121 $|\Omega_{\text{BdG}}\rangle$, the transformation decreases the total number of particles by 1. Conversely, if it is un-

1122 occupied ($\epsilon_{j_0} > 0$), or $\tilde{a}_{j_0}^\dagger \tilde{a}_{j_0} |\Omega_{\text{BdG}}\rangle = 0$, the transformation increases the particle number by
 1123 one.

1124 The fermion parity operator can be defined by

$$P = \prod_j (1 - 2a_j^\dagger a_j) \quad (\text{A.24})$$

1125 so that $P = 1$ if the number of occupied states is even, and -1 otherwise. Alternatively, since

$$a_j^\dagger a_j = \frac{1}{4} (c_{2j-1} - i c_{2j}) (c_{2j-1} + i c_{2j}) = \frac{1}{2} (1 + i c_{2j-1} c_{2j}) \quad (\text{A.25})$$

1126 P can be written in the Majorana representation as

$$P = \prod_j (-i c_{2j-1} c_{2j}). \quad (\text{A.26})$$

1127 Eq. [A.20](#) transforms P by changing

$$1 - 2\tilde{a}_{j_0}^\dagger \tilde{a}_{j_0} \rightarrow 1 - 2\tilde{a}'_{j_0} \tilde{a}'_{j_0}{}^\dagger = -(1 - \tilde{a}_{j_0}^\dagger \tilde{a}'_{j_0}) \quad (\text{A.27})$$

1128 and hence indeed changes P .

1129

We can also understand why the BdG Hamiltonian preserves P but not N . Due to the fol-

1130

lowing commutation relations:

$$[a_j^\dagger a_l, a_j^\dagger a_j] = a_j^\dagger a_l a_j^\dagger a_j - a_j^\dagger a_j a_j^\dagger a_l = -a_j^\dagger a_l \quad (\text{A.28})$$

$$[a_j^\dagger a_l, a_l^\dagger a_l] = a_j^\dagger a_l a_l^\dagger a_l - a_l^\dagger a_l a_j^\dagger a_l = a_j^\dagger a_l$$

$$[a_j^\dagger a_l^\dagger, a_j^\dagger a_j] = a_j^\dagger a_l^\dagger a_j^\dagger a_j - a_j^\dagger a_j a_j^\dagger a_l^\dagger = -a_j^\dagger a_l^\dagger$$

$$[a_j^\dagger a_l^\dagger, a_l^\dagger a_l] = a_j^\dagger a_l^\dagger a_l^\dagger a_l - a_l^\dagger a_l a_j^\dagger a_l^\dagger = -a_j^\dagger a_l^\dagger$$

$$[a_j a_l, a_j^\dagger a_j] = a_j a_l a_j^\dagger a_j - a_j^\dagger a_j a_j a_l = a_j a_l$$

$$[a_j a_l, a_l^\dagger a_l] = a_j a_l a_l^\dagger a_l - a_l^\dagger a_l a_j a_l = a_j a_l$$

1131

and

$$[a_j^\dagger a_l, (1 - 2a_j^\dagger a_j)(1 - 2a_l^\dagger a_l)] = (1 - 2a_j^\dagger a_j)[a_j^\dagger a_l, (1 - 2a_l^\dagger a_l)] + [a_j^\dagger a_l, (1 - 2a_j^\dagger a_j)](1 - 2a_l^\dagger a_l) \quad (\text{A.29})$$

$$= -2(1 - 2a_j^\dagger a_j)a_j^\dagger a_l + 2a_j^\dagger a_l(1 - 2a_l^\dagger a_l)$$

$$= -2a_j^\dagger a_l + 4a_j^\dagger a_l + 2a_j^\dagger a_l - 4a_j^\dagger a_l = 0$$

$$[a_j a_l, (1 - 2a_j^\dagger a_j)(1 - 2a_l^\dagger a_l)] = (1 - 2a_j^\dagger a_j)[a_j a_l, (1 - 2a_l^\dagger a_l)] + [a_j a_l, (1 - 2a_j^\dagger a_j)](1 - 2a_l^\dagger a_l)$$

$$= -2(1 - 2a_j^\dagger a_j)a_j a_l - 2a_j a_l(1 - 2a_l^\dagger a_l)$$

$$= -2a_j a_l - 2a_j a_l + 4a_j a_l = 0$$

1132

we have

$$[H, N] = 2 \sum_{jl} (\Delta_{jl} a_j a_l - \Delta_{jl}^\dagger a_j^\dagger a_l^\dagger) \quad (\text{A.30})$$

$$[H, P] = 0$$

1133 Since $[H, P] = 0$, there are common eigenstates of H and P , or that they can be simultane-
 1134 ously diagonalized by some unitary transformation. However, since P is not a one-body op-
 1135 erator, its unitary transformation in general cannot be written as multiplications of $2N \times 2N$
 1136 matrices as the BdG Hamiltonian. We therefore need to understand how the Bogoliubov trans-
 1137 formation Eq. A.9 transforms P . To this end we first write Eq. A.9 into a block form

$$(\tilde{a}^\dagger, \tilde{a}) = (a^\dagger, a)\mathcal{U} \quad (\text{A.31})$$

1138 where $a \equiv (a_1, a_2, \dots, a_N)$ and so on. On the other hand, Eqs. A.2 and A.1 can be written as

$$(c_o, c_e) = (a^\dagger, a) \begin{pmatrix} 1 & i \\ 1 & -i \end{pmatrix}, \quad (a^\dagger, a) = (c_o, c_e) \begin{pmatrix} \frac{1}{2} & \frac{1}{2} \\ -\frac{i}{2} & \frac{i}{2} \end{pmatrix} \quad (\text{A.32})$$

1139 where $c_o \equiv (c_1, c_3, \dots, c_{2N-1})$ and $c_e \equiv (c_2, c_4, \dots, c_{2N})$. The above equations then lead to

$$\begin{aligned} (\tilde{c}_o, \tilde{c}_e) &= (c_o, c_e) \begin{pmatrix} \frac{1}{2} & \frac{1}{2} \\ -\frac{i}{2} & \frac{i}{2} \end{pmatrix} \mathcal{U} \begin{pmatrix} 1 & i \\ 1 & -i \end{pmatrix} \\ &= (c_o, c_e) \begin{pmatrix} \text{Re}(U_1 + U_2) & -\text{Im}(U_1 - U_2) \\ \text{Im}(U_1 + U_2) & \text{Re}(U_1 - U_2) \end{pmatrix} \\ &= (c_o, c_e)\mathcal{O} \end{aligned} \quad (\text{A.33})$$

1140 or equivalently

$$\tilde{c}_{2j-1} = c_{2k-1}\mathcal{O}_{k,j} + c_{2k}\mathcal{O}_{N+k,j} \quad (\text{A.34})$$

$$\tilde{c}_{2j} = c_{2k-1}\mathcal{O}_{k,N+j} + c_{2k}\mathcal{O}_{N+k,N+j}$$

1141

Since all elements of \mathcal{O} are real,

$$\mathcal{O}^T \mathcal{O} = \mathcal{O}^\dagger \mathcal{O} = \begin{pmatrix} \frac{1}{2} & \frac{1}{2} \\ -\frac{i}{2} & \frac{i}{2} \end{pmatrix} \mathcal{U}^\dagger \mathcal{U} \begin{pmatrix} 1 & i \\ 1 & -i \end{pmatrix} = \mathbb{I} \quad (\text{A.35})$$

1142

Namely, \mathcal{O} is a real orthogonal matrix. As a result we have

$$1 = \det(\mathcal{O}^T \mathcal{O}) = (\det\{\mathcal{O}\})^2 \quad (\text{A.36})$$

1143

which necessarily means $\det\{\mathcal{O}\} = \pm 1$. From linear algebra we know that an arbitrary special

1144

orthogonal matrix, i.e., $\det\{\mathcal{O}\} = +1$, can always be written as

$$\mathcal{O} = e^A \quad (\text{A.37})$$

1145

where $A = -A^T$ is a real skew-symmetric matrix. But no such general expressions exist for those

1146

\mathcal{O} with $\det \mathcal{O} = -1$. For later convenience we reorganize the elements of \mathcal{O} so that they are

1147

labeled in the same way as the Majorana operators. Namely

$$\mathcal{O}_{k,j} \rightarrow \mathcal{O}_{2k-1,2j-1} \quad (\text{A.38})$$

$$\mathcal{O}_{N+k,j} \rightarrow \mathcal{O}_{2k,2j-1}$$

$$\mathcal{O}_{k,N+j} \rightarrow \mathcal{O}_{2k-1,2j}$$

$$\mathcal{O}_{N+k,N+j} \rightarrow \mathcal{O}_{2k,2j}$$

1148

This does not affect the orthogonality of \mathcal{O} .

1149

To see how \mathcal{O} transforms P , we start from Eq. A.26 and note that it can be written as

$$P = (-i)^N \prod_{j=1}^N (c_{2j-1} c_{2j}) = \text{pf}(\mathbb{C}) \quad (\text{A.39})$$

1150 where

$$\mathcal{C} \equiv \begin{pmatrix} C_1 & & \\ & \ddots & \\ & & C_N \end{pmatrix}, C_j \equiv \begin{pmatrix} 0 & -ic_{2j-1}c_{2j} \\ ic_{2j-1}c_{2j} & 0 \end{pmatrix} \quad (\text{A.40})$$

1151 The pfaffian pf for an arbitrary skew-symmetric matrix is defined as

$$\text{pf}(A) = \frac{1}{2^n n!} \sum_{\sigma \in S_{2n}} \text{sgn}(\sigma) \prod_{i=1}^n a_{\sigma(2i-1), \sigma(2i)} \quad (\text{A.41})$$

1152 where A is a $2n \times 2n$ skew-symmetric matrix, S_{2n} is the permutation group of order $2n$. For skew-
 1153 symmetric tridiagonal A with $A_{2j-1, 2j} = -A_{2j, 2j-1} = b_j$ and all other elements zero, $\text{pf}(A) =$
 1154 $\prod_{j=1}^n b_j$. Eq. A.39 is valid since all the $-ic_{2j-1}c_{2j}$ commute with one another and can be viewed
 1155 as c-numbers.

1156 Our goal is to convert the complicated transformation rule of P under \mathcal{O} to something that
 1157 is more manageable. To this end we generalize the \mathcal{C} matrix above to the following:

$$\mathcal{C}_{mn} = \begin{cases} 0 & m = n \\ -ic_m c_n & m \neq n \end{cases} \quad (\text{A.42})$$

1158 Apparently $\mathcal{C} = -\mathcal{C}^T$ and one can still calculate its pfaffian. To simplify the calculation we use
 1159 the following equivalent definition of the pfaffian:

$$\text{pf}(A) = \sum_{\alpha \in \Pi} A_\alpha \quad (\text{A.43})$$

1160 where A_α is

$$A_\alpha = \text{sgn}(\pi_\alpha) a_{i_1, j_1} a_{i_2, j_2} \cdots a_{i_n, j_n} \quad (\text{A.44})$$

1161 and the permutation π_α and its set Π are constructed in the following way: Consider a partition
 1162 of $\{1, 2, \dots, 2n\}$ into unordered pairs and define α as such a partition

$$\alpha = \{(i_1, j_1), (i_2, j_2), \dots, (i_n, j_n)\} \quad (\text{A.45})$$

1163 so that there are $(2n)!/(2^n n!)$ such partitions. The permutation π_α is defined as

$$\pi_\alpha \equiv \begin{pmatrix} 1 & 2 & 3 & 4 & \dots & 2n-1 & 2n \\ i_1 & j_1 & i_2 & j_2 & \dots & i_n & j_n \end{pmatrix} \quad (\text{A.46})$$

1164 For our \mathcal{C} this means the counterpart of A_α is

$$\text{sgn}(\pi_\alpha)(-i)^N c_{m_1} c_{n_1} c_{m_2} c_{n_2} \dots c_{m_N} c_{n_N} = \prod_{j=1}^N (-i c_{2j-1} c_{2j}) \quad (\text{A.47})$$

1165 since $\text{sgn}(\pi_\alpha)$ is exactly compensated by the anticommutation relation of the Majorana fermions.

1166 We therefore have

$$P = \frac{2^N N!}{(2N)!} \text{pf}(\mathcal{C}) \quad (\text{A.48})$$

1167 We next consider the transformation of \mathcal{C} by \mathcal{O} :

$$\tilde{\mathcal{C}}_{mn} = -i \tilde{c}_m \tilde{c}_n = -i \sum_{i \neq j} \mathcal{O}_{mi} \mathcal{O}_{nj} c_i c_j = (\mathcal{O}^T \mathcal{C} \mathcal{O})_{mn} \quad (\text{A.49})$$

1168 which is nothing but the usual similarity transformation of the matrix \mathcal{C} . We therefore immedi-

1169 ately get

$$\begin{aligned} \tilde{P} &= \frac{2^N N!}{(2N)!} \text{pf}(\tilde{\mathcal{C}}) = \frac{2^N N!}{(2N)!} \text{pf}(\mathcal{O}^T \mathcal{C} \mathcal{O}) = \frac{2^N N!}{(2N)!} \text{pf}(\mathcal{C}) \det(\mathcal{O}) \\ &= \det(\mathcal{O}) P \end{aligned} \quad (\text{A.50})$$

1170 Therefore the Bogoliubov transformation \mathcal{O} preserves the parity if $\det(\mathcal{O}) = +1$, and changes the
 1171 parity if $\det(\mathcal{O}) = -1$.

1172 Using the above transformation rule of P under a general Bogoliubov transformation we can
 1173 now understand the meaning of ground state parity in [8]. Start from an arbitrary state that is
 1174 an eigenstate of P with even parity, we have

$$P|\psi\rangle = |\psi\rangle \quad (\text{A.51})$$

1175 Under a Bogoliubov transformation, the state itself is unchanged, but $P \rightarrow \tilde{P}$, since the meaning
 1176 of particles is different. We then have

$$\tilde{P}|\psi\rangle = \det(\mathcal{O})P|\psi\rangle = \det(\mathcal{O})|\psi\rangle \quad (\text{A.52})$$

1177 Namely, because the Bogoliubov transformation redefines particles and hence the parity op-
 1178 erator, an even-parity state can become an odd-parity state in the new definition of the parity
 1179 operator. Therefore for a given BdG Hamiltonian, the meaning of its ground state parity must
 1180 be relative, and we need to choose a reference in order to discuss the parity. Such a reference is
 1181 the ground state of the “canonical form” of the BdG Hamiltonian:

$$\begin{aligned} H_{\text{canonical}} &= \sum_m \epsilon_m (\tilde{a}_m^\dagger \tilde{a}_m - \frac{1}{2}) = \frac{i}{2} \sum_m \tilde{c}_{2m-1} \tilde{c}_{2m} \\ &\equiv \frac{i}{2} \sum_m \epsilon_m b'_m b''_m, \quad \epsilon_m \geq 0 \end{aligned} \quad (\text{A.53})$$

1182 where the crucial requirement is that all the eigenenergies are non-negative. For a given BdG
 1183 Hamiltonian such a canonical form is uniquely fixed, and we can use its ground state as a refer-
 1184 ence for the parity and the parity operator. The ground state of $H_{\text{canonical}}$ is defined by

$$\tilde{a}_m |\Omega_{\text{canonical}}\rangle = 0 \quad \forall m \in [1, N]. \quad (\text{A.54})$$

1185 and the “reference” or canonical parity operator is

$$P_{\text{canonical}} \equiv \prod_{m=1}^N (-i b'_m b''_m). \quad (\text{A.55})$$

1186 Since there are no \tilde{a} particles in $|\Omega_{\text{canonical}}\rangle$, we must have

$$P_{\text{canonical}}|\Omega_{\text{canonical}}\rangle = |\Omega_{\text{canonical}}\rangle \quad (\text{A.56})$$

1187 Namely $|\Omega_{\text{canonical}}\rangle$ has even parity. We can then ask the following question: What is the parity
 1188 of $|\Omega_{\text{canonical}}\rangle$ in the sense of particles in the original BdG Hamiltonian, i.e., a_j ? This requires us
 1189 to evaluate

$$\begin{aligned} P_{\text{BdG}}|\Omega_{\text{canonical}}\rangle &\equiv \prod_j (-i c_{2j-1} c_{2j}) |\Omega_{\text{canonical}}\rangle = \det(\mathcal{O}) P_{\text{canonical}}|\Omega_{\text{canonical}}\rangle \quad (\text{A.57}) \\ &= \det(\mathcal{O}) |\Omega_{\text{canonical}}\rangle \end{aligned}$$

1190 Namely, the parity is equal to the determinant of the orthogonal transformation that transforms
 1191 c to b' and b'' . More precisely,

$$\begin{pmatrix} b'_1 \\ b''_1 \\ \vdots \\ b'_N \\ b''_N \end{pmatrix} = \mathcal{O} \begin{pmatrix} c_1 \\ c_2 \\ \vdots \\ c_{2N-1} \\ c_{2N} \end{pmatrix} \quad (\text{A.58})$$

1192 and

$$\mathcal{O}A\mathcal{O}^T = \begin{pmatrix} 0 & \epsilon_1 & & \\ -\epsilon_1 & 0 & & \\ & & \ddots & \\ & & & 0 & \epsilon_N \\ & & & -\epsilon_N & 0 \end{pmatrix} \quad (\text{A.59})$$

1193 where A is introduced in Eq. A.4, and our \mathcal{O} is the matrix W in [8]. Eq. A.59 therefore leads to a
 1194 convenient formula for calculating $\det(\mathcal{O})$:

$$\text{pf}(\mathcal{O}A\mathcal{O}^T) = \det(\mathcal{O})\text{pf}(A) = \text{pf} \begin{pmatrix} 0 & \epsilon_1 & & \\ -\epsilon_1 & 0 & & \\ & & \ddots & \\ & & & 0 & \epsilon_N \\ & & & -\epsilon_N & 0 \end{pmatrix} = \prod_m \epsilon_m \geq 0 \quad (\text{A.60})$$

1195 Therefore

$$\det(\mathcal{O}) = \left(\prod_m \epsilon_m \right) [\text{pf}(A)]^{-1} \quad (\text{A.61})$$

1196 Since $\det(\mathcal{O}) = \pm 1$ we only need the signs of the two quantities on the right hand side of the
 1197 above equation. If none of the ϵ_m vanishes, $(\prod_m \epsilon_m) > 0$, we finally arrive at

$$\det(\mathcal{O}) = \text{sgn}[\text{pf}(A)] \quad (\text{A.62})$$

1198 Namely,

$$\begin{aligned} P_{\text{BdG}}|\Omega_{\text{canonical}}\rangle &= \det(\mathcal{O})|\Omega_{\text{canonical}}\rangle \\ &= \text{sgn}[\text{pf}(A)]|\Omega_{\text{canonical}}\rangle \end{aligned} \quad (\text{A.63})$$

1199 **A.2 Gauge potential and gauge invariance**

1200 In this section we address the question of how to understand the Peierls substitution in BdG
1201 Hamiltonian.

1202 Although the superconductivity order parameter appears to break the U(1) gauge symme-
1203 try, all physical observables are still gauge invariant. More explicitly, consider a general tight-
1204 binding BdG Hamiltonian

$$H = \sum_{ij,\alpha\beta} \left(t_{ij}^{\alpha\beta} c_{i\alpha}^\dagger c_{j\beta} + \Delta_{ij,\alpha\beta} c_{i\alpha} c_{j\beta} - \frac{\mu}{2} c_{i\alpha}^\dagger c_{i\alpha} + \text{h.c.} \right) \equiv \frac{1}{2} C^\dagger h C \quad (\text{A.64})$$

1205 where i, j label position, α, β label any internal degrees of freedom, and $C = (\{c_{i\alpha}\}, \{c_{i\alpha}^\dagger\})^T$. H
1206 has the eigensolutions

$$H|\psi_n\rangle = \epsilon_n|\psi_n\rangle \quad (\text{A.65})$$

$$|\psi_n\rangle = d_{\psi_n}^\dagger |\Omega\rangle = \sum_{i\alpha\sigma} c_{i\alpha}^\sigma |\Omega\rangle U_{i\alpha\sigma,n}$$

1207 where $|\Omega\rangle$ is the BCS ground state, $\sigma = \pm$ distinguishes the creation (particle) and annihilation
1208 (creation for hole) operators, and U is a Bogoliubov transformation matrix which is unitary for
1209 fermions. Substituting $|\psi\rangle$ into the eigenequation leads to

$$U^\dagger h U = \text{Diag}[\{\epsilon_n\}] \quad (\text{A.66})$$

1210 where the pairing potential satisfies the gap equation

$$\begin{aligned}\Delta_{ij,\alpha\beta} &= Z^{-1} \text{Tr}[V_{j\beta,i\alpha} c_{j\beta}^\dagger c_{i\alpha}^\dagger e^{-\frac{1}{k_B T} H}] \\ &= \sum_n f(\epsilon_n) (U^\dagger \mathbb{V} U)_{nn}\end{aligned}\tag{A.67}$$

1211 where \mathbb{V} is a matrix with the only nonzero element being $\mathbb{V}_{j\beta+,i\alpha-} = V_{j\beta,i\alpha}$, f is the Fermi-Dirac
1212 distribution function.

1213 We now show that physical observables are gauge invariant. A gauge transformation corre-
1214 sponds to

$$\mathbf{A} \rightarrow \mathbf{A}' = \mathbf{A} + \nabla \chi\tag{A.68}$$

1215 where \mathbf{A} is the gauge potential. \mathbf{A} enters the tight-binding Hamiltonian implicitly through the
1216 Peierls substitution:

$$c_{i\alpha}^\dagger \rightarrow \tilde{c}_{i\alpha}^\dagger = e^{-\frac{ie}{\hbar} \int_0^{\mathbf{r}_i} \mathbf{A} \cdot d\mathbf{l}} c_{i\alpha}^\dagger\tag{A.69}$$

1217 and we can understand Eq. (A.64) as that written for certain \mathbf{A} already absorbed into the defini-
1218 tions of t and Δ . The gauge transformation leads to

$$c_{i\alpha}^\dagger \rightarrow c_{i\alpha}^\dagger e^{-\frac{ie}{\hbar} \chi_i}\tag{A.70}$$

1219 The Hamiltonian therefore becomes

$$\begin{aligned}H \rightarrow H' &= \sum_{ij,\alpha\beta} \left[t_{ij}^{\alpha\beta} e^{-\frac{ie}{\hbar}(\chi_i - \chi_j)} c_{i\alpha}^\dagger c_{j\beta} + \Delta_{ij,\alpha\beta} e^{\frac{ie}{\hbar}(\chi_i + \chi_j)} c_{i\alpha} c_{j\beta} - \frac{\mu}{2} c_{i\alpha}^\dagger c_{i\alpha} + \text{h.c.} \right] \\ &= \frac{1}{2} C^\dagger U_\chi h U_\chi^\dagger C\end{aligned}\tag{A.71}$$

1220 where

$$U_\chi = \text{Diag}[\{e^{-\frac{ie}{\hbar}\chi_i}\}, \{e^{\frac{ie}{\hbar}\chi_i}\}] \quad (\text{A.72})$$

1221 As a result, the BdG eigenvalues as well as all other physical observables represented in terms
 1222 of Bogoliubov quasiparticles are invariant under the gauge transformation.

1223 The above derivation includes, however, an assumption. Namely the pairing potential $\Delta_{ij,\alpha\beta}$
 1224 stays unchanged. This is indeed the case, since

$$\begin{aligned} \Delta'_{ij,\alpha\beta} &= Z'^{-1} \text{Tr}[V_{j\beta,i\alpha} c_{j\beta}^\dagger c_{i\alpha}^\dagger e^{-\frac{ie}{\hbar}(\chi_i + \chi_j)} e^{-\frac{1}{k_B T} H'}] \\ &= \sum_n f(\epsilon_n) (U^\dagger U_\chi^\dagger U_\chi \mathbb{V} U_\chi^\dagger U_\chi U) \\ &= \Delta_{ij,\alpha\beta} \end{aligned} \quad (\text{A.73})$$

1225 **A.3 Kitaev Triangle and Peierls substitution**

1226 We start with a spinless or spin-polarized p -wave superconductor

$$\mathcal{H} = \sum_{\langle j,l \rangle} (-t c_j^\dagger c_l + \Delta e^{i\theta_{jl}} c_j c_l + h.c.) - \sum_j \mu c_j^\dagger c_j, \quad (\text{A.74})$$

1227 where t is the hopping amplitude, Δ is the amplitude of (2D) p -wave pairing, μ is the chemical
 1228 potential, θ_{jl} is the polar angle of $\mathbf{r}_{jl} = \mathbf{r}_l - \mathbf{r}_j$, consistent with $\{c_l^\dagger, c_j^\dagger\} = 0$.

We will now include a gauge potential via a Peierls substitution as

$$\begin{aligned}
c_j^\dagger &\rightarrow c_j^\dagger \exp\left(-\frac{ie}{\hbar} \int_0^{\mathbf{r}_j} \mathbf{A} \cdot d\mathbf{l}\right), \\
c_j^\dagger c_l &\rightarrow c_j^\dagger c_l \exp\left(\frac{ie}{\hbar} \int_{\mathbf{r}_j}^{\mathbf{r}_l} \mathbf{A} \cdot d\mathbf{l}\right) \\
&\rightarrow c_l^\dagger c_j e^{i\phi_{j,l}}, \\
\phi_{jl} &= \frac{e}{\hbar} \int_{\mathbf{r}_j}^{\mathbf{r}_l} \mathbf{A} \cdot d\mathbf{l} = -\phi_{lj}
\end{aligned} \tag{A.75}$$

1229 The modified Hamiltonian is then

$$\mathcal{H} = \sum_{\langle j,l \rangle} (-te^{i\phi_{jl}} c_j^\dagger c_l + \Delta e^{i\theta_{jl}} c_j c_l + h.c.) - \sum_j \mu c_j^\dagger c_j, \tag{A.76}$$

1230 The complex fermion operator can be written in the Majorana Fermion basis, a superposi-
1231 tion of two Majorana fermions $c_j = \frac{1}{2}(a_j + ib_j)$. Due to the nature of Majorana fermions, $a_j^\dagger = a_j$,
1232 the creation operator is $c_j^\dagger = \frac{1}{2}(a_j - ib_j)$. It is quickly seen after substitution we arrive at

$$c_j^\dagger c_j = \frac{1}{2}(1 + ia_j b_j), \tag{A.77}$$

$$c_j^\dagger c_l = \frac{1}{4}(a_j a_l + b_j b_l + ia_j b_l - ib_j a_l), \tag{A.78}$$

$$c_j c_l = \frac{1}{4}(a_j a_l - b_j b_l + ia_j b_l + ib_j a_l). \tag{A.79}$$

1233 The hopping term in MF basis are

$$-t(e^{i\phi_{jl}} c_j^\dagger c_l + e^{-i\phi_{jl}} c_l^\dagger c_j) = -\frac{it}{2}(\sin \phi_{jl}(a_j a_l + b_j b_l) + \cos \phi_{jl}(a_j b_l - b_j a_l)), \tag{A.80}$$

1234 the order parameter terms are

$$\Delta(e^{i\theta_{jl}}c_j^\dagger c_l^\dagger + e^{-i\theta_{jl}}c_j c_l) = \frac{i\Delta}{2}(\sin\theta_{jl}(a_l a_j - b_l b_j) + \cos\theta_{jl}(a_l b_j + b_l a_j)). \quad (\text{A.81})$$

1235 Our Hamiltonian in MF basis is then

$$\begin{aligned} \mathcal{H} = & -\frac{i}{2} \sum_{\langle j,l \rangle} [(t \sin\phi_{jl} - \Delta \sin\theta_{jl}) a_j a_l + (t \sin\phi_{jl} + \Delta \sin\theta_{jl}) b_j b_l \\ & + (t \cos\phi_{jl} - \Delta \cos\theta_{jl}) a_j b_l - (t \cos\phi_{jl} + \Delta \cos\theta_{jl}) b_j a_l] \\ & - \frac{i\mu}{2} \sum_j a_j b_j \end{aligned} \quad (\text{A.82})$$

1236 For concreteness we consider a 1-D chain in the Kitaev limit $t = \Delta$, $\mu = 0$, and choose
 1237 $\phi_{jl} = 0$ (either zero or a perpendicular gauge potential). The Kitaev chain is resultant with
 1238 $\mathcal{H} = -\sum_{j,j+1} i t b_j a_{j+1}$ and hosting MZM a_1 and b_N .

Appendix B

Landau Level-Like Topological Floquet Hamiltonians

B.1 Quantum harmonic oscillator

We will quickly derive this energy solution and derive ladder operators. Rewrite the quantum harmonic oscillator as (and dropping the operator hat)

$$H = \frac{1}{2m} (p_x^2 + m^2 \omega^2 x^2),$$

then complete the square by adding "zero"

$$\begin{aligned} H &= \frac{1}{2m} ([m\omega x - i p_x][m\omega x + i p_x] - i m\omega [x p_x - p_x x]) \\ &= \frac{1}{2m} ([m\omega x - i p_x][m\omega + i p_x] + m\hbar\omega) \\ &= \frac{1}{2m} (\tilde{a}^\dagger \tilde{a} + m\hbar\omega) \\ &= \hbar\omega \left(\frac{\tilde{a}^\dagger \tilde{a}}{2m\hbar\omega} + \frac{1}{2} \right) \\ &= \hbar\omega \left(a^\dagger a + \frac{1}{2} \right), \end{aligned} \tag{B.1}$$

where $a = \frac{1}{\sqrt{2}} \left(\sqrt{\frac{m\omega}{\hbar}} x + i \frac{p_x}{\sqrt{m\hbar\omega}} \right)$. We have simplified the Hamiltonian into new creation and annihilation operators, called ladder operators, which we will now show how they work. Also note $[a, a^\dagger] = 1$. Let looks at how the operator commutes with the Hamiltonian

$$\begin{aligned}
[H, a] &= Ha - aH = \hbar\omega \left(a^\dagger aa + \frac{a}{2} - aa^\dagger a - \frac{a}{2} \right) \\
&= \hbar\omega (a^\dagger a - (1 + a^\dagger a))a \\
&= -\hbar\omega a, \quad \text{and}
\end{aligned} \tag{B.2}$$

$$\begin{aligned}
[H, a^\dagger] &= Ha^\dagger - a^\dagger H = \hbar\omega \left(a^\dagger aa^\dagger + \frac{a^\dagger}{2} - a^\dagger a^\dagger a - \frac{a^\dagger}{2} \right) \\
&= \hbar\omega a^\dagger (aa^\dagger - a^\dagger a) \\
&= \hbar\omega a^\dagger.
\end{aligned} \tag{B.3}$$

1248 SOME TRANSITION TO ACTING Ha on Psi.

$$\begin{aligned}
H|\psi_n\rangle &= E_n|\psi_n\rangle. \\
Ha^\dagger|\psi_n\rangle &= (a^\dagger H + \hbar\omega a^\dagger)|\psi_n\rangle \\
Ha^\dagger|\psi_n\rangle &= (E_n + \hbar\omega)a^\dagger|\psi_n\rangle. \\
Ha|\psi_n\rangle &= (E_n - \hbar\omega)a|\psi_n\rangle.
\end{aligned} \tag{B.4}$$

1249 Being careful notice

$$\begin{aligned}
H|\psi_0\rangle &= E_0|\psi_0\rangle \\
Ha|\psi_0\rangle &= (E_0 - \hbar\omega)a|\psi_0\rangle,
\end{aligned} \tag{B.5}$$

1250 however, E_0 is the minimum so $E_0 - \hbar\omega$ cannot exist and thus

$$a|\psi_0\rangle = 0 \quad (\text{B.6})$$

1251 Again we look at the ground state energy

$$\begin{aligned} \langle\psi_0|H|\psi_0\rangle &= \langle\psi_0|\hbar\omega(a^\dagger a + 1/2)|\psi_0\rangle \\ E_0 &= \hbar\omega\langle\psi_0|a^\dagger a|\psi_0\rangle + \frac{\hbar\omega}{2}\langle\psi_0|\psi_0\rangle \\ E_0 &= \frac{\hbar\omega}{2}. \end{aligned} \quad (\text{B.7})$$

1252 Then for the given eigenstates

$$a^\dagger|\psi_0\rangle, \quad a^\dagger a^\dagger|\psi_0\rangle, \quad a^\dagger a^\dagger a^\dagger|\psi_0\rangle, \quad \dots$$

with eigenvalues

$$\frac{3}{2}\hbar\omega, \quad \frac{5}{2}\hbar\omega, \quad \frac{7}{2}\hbar\omega, \quad \dots$$

1253 Which we can generalize to

$$|\psi_n\rangle \propto (a^\dagger)^n|\psi_0\rangle,$$

1254 with the eigenenergy

$$E_n = \hbar\omega\left(n + \frac{1}{2}\right).$$

1255 With our goal complete we continue on to determine how the ladder operators evolve the state.

1256 We can now renormalize our proportional expression

$$|\psi_{n+1}\rangle = c a^\dagger |\psi_n\rangle$$

$$1 = \langle \psi_{n+1} | \psi_{n+1} \rangle = |c|^2 (\langle \psi_n | a^\dagger) (a^\dagger | \psi_n \rangle)$$

$$= |c|^2 \langle \psi_n | a a^\dagger | \psi_n \rangle$$

$$= |c|^2 \langle \psi_n | \frac{H}{\hbar\omega} + \frac{1}{2} | \psi_n \rangle$$

$$= |c|^2 \left(\frac{E_n}{\hbar\omega} + \frac{1}{2} \right)$$

$$= |c|^2 (n+1)$$

$$|c| = \frac{1}{\sqrt{n+1}}$$

1257 which give the following relation

$$|\psi_{n+1}\rangle = \frac{a^\dagger}{\sqrt{n+1}} |\psi_n\rangle. \quad (\text{B.8})$$

1258 Similarly we find

$$|\psi_{n-1}\rangle = \frac{a}{\sqrt{n}} |\psi_n\rangle. \quad (\text{B.9})$$

1259 Thus $a^\dagger a |\psi_n\rangle = n |\psi_n\rangle$. The energy of the system is definitively

$$E_n = \hbar\omega \left(n + \frac{1}{2} \right) \quad (\text{B.10})$$

1260 **B.2 Dirac equation in the presence of a magnetic field**

1261 We now focus on how the presence of a magnetic field affects the Dirac equation. The Dirac

1262 Hamiltonian with vector potential

$$\mathcal{H} = v_f \boldsymbol{\sigma} \cdot (\hat{\mathbf{p}} - q \hat{\mathbf{A}}) \quad (\text{B.11})$$

1263 Using the previous definition, $\mathbf{A} = Bx\hat{\mathbf{y}}$, the Hamiltonian becomes

$$\mathcal{H} = v_f \sigma_x \hat{p}_x + v_f \sigma_y (\hat{p}_y - qB\hat{x}) \quad (\text{B.12})$$

1264 Like Schrodinger's equation we use the same ansatz wavefunction and arrive at

$$\begin{aligned} \mathcal{H} &= v_f \sigma_x \hat{p}_x - v_f \sigma_y (qB\hat{x} - \hbar k_y) \\ \mathcal{H} &= v_f \sigma_x \hat{p}_x - v_f \sigma_y qB\hat{x}, \end{aligned} \quad (\text{B.13})$$

1265 where we recognize the x term is just shifted by a constant like earlier. In matrix form the Hamil-
1266 tonian looks like

$$\begin{aligned} \mathcal{H} &= i v_f q B \begin{bmatrix} 0 & \hat{p}_x + i q B \hat{x} \\ \hat{p}_x - i q B \hat{x} & 0 \end{bmatrix} \\ \mathcal{H} &= i v_f \sqrt{2 \hbar q B} \begin{bmatrix} 0 & a^\dagger \\ -a & 0 \end{bmatrix} \end{aligned}$$

1267 The form of the Hamiltonian can be quickly solved by squaring then acting on a wavefunction

$$\mathcal{H}^2 = 2 \hbar q B v_f^2 \begin{bmatrix} a^\dagger a & 0 \\ 0 & a a^\dagger \end{bmatrix}$$

1268 We focus on the first element of the matrix

$$\begin{aligned}
\langle \psi_n | \mathcal{H}_{11}^2 | \psi_n \rangle &= \langle \psi_n | E_n^2 | \psi_n \rangle \\
&= 2\hbar q B v_f^2 \langle \psi_n | a^\dagger a | \psi_n \rangle \\
&= 2\hbar q B v_f^2 \langle \psi_n | n | \psi_n \rangle \\
E_n^2 &= 2\hbar q B n v_f^2 \\
E_n &= \pm v_f \sqrt{2\hbar q B n}
\end{aligned} \tag{B.14}$$

B.3 General framework of Floquet theory

In this section we review the basic results of the Floquet theory and how to recast it into a matrix diagonalization problem. The discussion in this section is mostly following [77].

For a time-periodic Hamiltonian $H(t) = H(t + T)$ with period T , the time evolution of a wavefunction governed by it is described by the Schrödinger equation

$$i\hbar \partial_t \psi(t) = H(t) \psi(t). \tag{B.15}$$

Floquet theorem states that $\psi(t)$ must satisfy

$$\psi(t + T) = \psi(t) e^{-i \frac{\epsilon T}{\hbar}}, \tag{B.16}$$

where ϵ is a real number of energy units, or equivalently

$$\psi(t) = e^{-i \frac{\epsilon t}{\hbar}} u_\epsilon(t), \tag{B.17}$$

where $u_\epsilon(t) = u_\epsilon(t + T)$.

1277 Here we give a proof that is closely analogous to that of the Bloch theorem, based on plane
 1278 wave expansion. An arbitrary wavefunction can be expanded into plane waves

$$\psi(t) = \sum_{\epsilon} c_{\epsilon} e^{-i \frac{\epsilon t}{\hbar}}, \quad (\text{B.18})$$

1279 where $\epsilon \in \mathbb{R}$, while a time-periodic function $H(t)$ can only be written as a discrete Fourier series

$$H(t) = \sum_n H_n e^{in\omega t}, \quad (\text{B.19})$$

1280 where $\omega = 2\pi/T$, and $H_n = \frac{1}{T} \int_0^T H(t) e^{-in\omega t} dt$. Substituting the two expansions above into
 1281 Eq. B.15 gives

$$\begin{aligned} 0 &= \sum_{\epsilon} \left[\sum_n H_n e^{-i \frac{(\epsilon - n\hbar\omega)t}{\hbar}} c_{\epsilon} - \epsilon c_{\epsilon} e^{-i \frac{\epsilon t}{\hbar}} \right] \\ &= \sum_{\epsilon} \left[\sum_n H_n c_{\epsilon + n\hbar\omega} - \epsilon c_{\epsilon} \right] e^{-i \frac{\epsilon t}{\hbar}}, \end{aligned} \quad (\text{B.20})$$

1282 which leads to

$$\sum_n H_n c_{\epsilon + n\hbar\omega} - \epsilon c_{\epsilon} = 0. \quad (\text{B.21})$$

1283 For an arbitrary $\epsilon \in \mathbb{R}$ we can define $\tilde{\epsilon} \in [-\hbar\omega/2, \hbar\omega/2)$ so that $\epsilon = \tilde{\epsilon} + m\hbar\omega$. It is apparent that
 1284 Eq. B.21 only couples $c_{\tilde{\epsilon} + m\hbar\omega}$ belonging to the same $\tilde{\epsilon}$. We thus define

$$c_{\tilde{\epsilon} + m\hbar\omega} \equiv c_{m\tilde{\epsilon}}, \quad (\text{B.22})$$

1285 so that Eq. B.21 becomes a set of coupled equations for $c_{m\tilde{\epsilon}}$, $m \in \mathbb{Z}$:

$$\sum_n (H_n - m\hbar\omega \delta_{n0}) c_{m+n, \tilde{\epsilon}} = \tilde{\epsilon} c_{m\tilde{\epsilon}}. \quad (\text{B.23})$$

Eq. B.21 is the eigenvalue problem of the infinite-dimensional matrix \bar{Q} with the matrix elements

$$\bar{Q}_{m,m+n} = H_n - m\hbar\omega\delta_{n0}, \quad (\text{B.24})$$

which is also the quasienergy operator in [77]. In practice the number of eigenvalues $\tilde{\epsilon}$ is determined by the dimension of $H(t)$. The solutions of Eq. B.15 are therefore

$$\psi_{\tilde{\epsilon}}(t) = \sum_m c_{m\tilde{\epsilon}} e^{-i\frac{(\tilde{\epsilon}+m\hbar\omega)t}{\hbar}} = e^{-i\frac{\tilde{\epsilon}t}{\hbar}} \sum_m c_{m\tilde{\epsilon}} e^{-im\omega t} \equiv e^{-i\frac{\tilde{\epsilon}t}{\hbar}} u_{\tilde{\epsilon}}(t). \quad (\text{B.25})$$

The proof above also gives a useful device for calculating the Floquet states $\psi_{\tilde{\epsilon}}(t)$ based on plane wave expansion. In general H_n can be a complicated operator depending on, e.g. position, spin, etc., and $c_{m\tilde{\epsilon}}$ is a function depending on these quantum numbers. One can choose a representation that makes H_0 diagonal, such as the Bloch representation, leading to the eigenvalues $\epsilon_{n\mathbf{k}}$ of the time-averaged Hamiltonian (H_0). When H_n is 0 for all $n \neq 0$, we have $\tilde{\epsilon} = \epsilon_{n\mathbf{k}} - m\hbar\omega$, $m \in \mathbb{Z}$. When H_n is nonzero for any $n \neq 0$ there is in general no simple relationship between $\tilde{\epsilon}$ and $\epsilon_{n\mathbf{k}}$. Nonetheless, when H_n , $n \neq 0$ can be viewed as perturbation the spectrum of $\tilde{\epsilon}$ is similar to that of $\epsilon_{n\mathbf{k}} - m\hbar\omega$, i.e., the eigenenergies $\epsilon_{n\mathbf{k}}$ together with infinite number of its copies shifted vertically by $m\hbar\omega$.

The importance of $\tilde{\epsilon}$ is that it completely determines the stroboscopic motion of an arbitrary Floquet wavefunction, i.e.,

$$\psi_{\tilde{\epsilon}}(t + mT) = e^{-i\frac{\tilde{\epsilon}mT}{\hbar}} \psi_{\tilde{\epsilon}}(t), \quad \forall m \in \mathbb{Z}. \quad (\text{B.26})$$

Since $\{\psi_{\tilde{\epsilon}}(t)\}$ is a complete set at time t , the stroboscopic evolution of an arbitrary wavefunction governed by $H(t)$ is

$$\Psi(t + mT) = \sum_{\tilde{\epsilon}} C_{\tilde{\epsilon}} e^{-i\frac{\tilde{\epsilon}mT}{\hbar}} \psi_{\tilde{\epsilon}}(t), \quad (\text{B.27})$$

1303 where $\Psi(t) = \sum_{\tilde{\epsilon}} C_{\tilde{\epsilon}} \psi_{\tilde{\epsilon}}(t)$. The full time-evolution operator $\hat{\mathbf{U}}(t_1, t_0)$ is therefore

$$\hat{\mathbf{U}}(t_1, t_0) = \sum_{\tilde{\epsilon}} |\psi_{\tilde{\epsilon}}(t_1)\rangle \langle \psi_{\tilde{\epsilon}}(t_0)| = \sum_{\tilde{\epsilon}} |u_{\tilde{\epsilon}}(t_1)\rangle \langle u_{\tilde{\epsilon}}(t_0)| e^{-i \frac{\tilde{\epsilon}(t_1 - t_0)}{\hbar}}. \quad (\text{B.28})$$

1304 Now we introduce two operators

$$\hat{\mathbf{U}}^F(t_1, t_0) \equiv \sum_{\tilde{\epsilon}} |u_{\tilde{\epsilon}}(t_1)\rangle \langle u_{\tilde{\epsilon}}(t_0)|, \quad (\text{B.29})$$

1305 and

$$\hat{\mathbf{H}}_{t_0}^F \equiv \sum_{\tilde{\epsilon}} |u_{\tilde{\epsilon}}(t_0)\rangle \tilde{\epsilon} \langle u_{\tilde{\epsilon}}(t_0)|, \quad (\text{B.30})$$

1306 which allows us to rewrite Eq. B.28 as

$$\hat{\mathbf{U}}(t_1, t_0) = \hat{\mathbf{U}}_F(t_1, t_0) \exp \left[-i \frac{(t_1 - t_0) \hat{\mathbf{H}}_{t_0}^F}{\hbar} \right] = \exp \left[-i \frac{(t_1 - t_0) \hat{\mathbf{H}}_{t_1}^F}{\hbar} \right] \hat{\mathbf{U}}_F(t_1, t_0). \quad (\text{B.31})$$

1307 Namely, the full time evolution is separated into two parts: $\hat{\mathbf{H}}_{t_0}^F$ governs the stroboscopic evolu-
1308 tion *with the starting time* t_0 , since

$$\exp \left[-i \frac{m T \hat{\mathbf{H}}_{t_0}^F}{\hbar} \right] \psi_{\tilde{\epsilon}}(t_0) = e^{-i \frac{m T \tilde{\epsilon}}{\hbar}} \psi_{\tilde{\epsilon}}(t_0) = \psi_{\tilde{\epsilon}}(t_0 + m T), \quad (\text{B.32})$$

1309 while $\hat{\mathbf{U}}_F(t_1, t_0)$ evolves the periodic part of the Floquet wavefunctions. $\hat{\mathbf{H}}_{t_0}^F$ and $\hat{\mathbf{U}}_F(t_1, t_0)$ are
1310 respectively called the Floquet Hamiltonian and the micromotion operator.

1311 The most unsettling property of $\hat{\mathbf{H}}_{t_0}^F$ is its dependence on t_0 . To get rid of it we note that
1312 Eq. B.25 implies

$$|u_{\tilde{\epsilon}}(t)\rangle = \sum_{\alpha} \left(\sum_m c_{m\tilde{\epsilon}}^{\alpha} e^{-i m \omega t} \right) |\alpha\rangle \equiv \sum_{\alpha} |\alpha\rangle U_{\alpha, \tilde{\epsilon}}(t), \quad (\text{B.33})$$

1313 where the time-independent basis $|\alpha\rangle$ spans the Hilbert space of $H(t)$, and $U(t)$ is a time-
 1314 dependent unitary matrix satisfying $U(t+T) = U(t)$. Substituting this $|u_{\tilde{\epsilon}}(t)\rangle$ into Eq. B.15 gives

$$\text{Diag}[\{\tilde{\epsilon}\}] = U^\dagger H(t) U - i\hbar U^\dagger \partial_t U = U^\dagger \tilde{Q} U, \quad (\text{B.34})$$

1315 where $\text{Diag}[\{\tilde{\epsilon}\}]$ is a diagonal matrix with its eigenvalues being $\tilde{\epsilon}$. Comparing this with the effect
 1316 of a time-dependent unitary transformation of the wavefunction $\psi' = U^\dagger \psi$ in the Schrödinger
 1317 equation:

$$i\hbar \partial_t \psi' = (U^\dagger H U - i\hbar U^\dagger \partial_t U) \psi' \equiv H' \psi', \quad (\text{B.35})$$

1318 we can see that U essentially transforms $H(t)$ to an effective Hamiltonian $H' = U^\dagger \tilde{Q} U$ which is
 1319 time independent. The time evolution of ψ can thus obtained as

$$\begin{aligned} \psi(t_1) &= U(t_1) \psi'(t_1) = U(t_1) \exp \left[-i \frac{H'(t_1 - t_0)}{\hbar} \right] \psi'(t_0) \\ &= U(t_1) \exp \left[-i \frac{H'(t_1 - t_0)}{\hbar} \right] U^\dagger(t_0) \psi(t_0) \\ &= \hat{\mathbf{U}}(t_1, t_0) \psi(t_0). \end{aligned} \quad (\text{B.36})$$

1320 We therefore define

$$\hat{\mathbf{H}}_F \equiv U^\dagger \tilde{Q} U = H' \quad (\text{B.37})$$

1321 as the Floquet effective Hamiltonian, which gives the time-evolution operator

$$\hat{\mathbf{U}}(t_1, t_0) = U(t_1) \exp \left[-i \frac{\hat{\mathbf{H}}_F(t_1 - t_0)}{\hbar} \right] U^\dagger(t_0). \quad (\text{B.38})$$

Intuitively, this means that the time evolution is obtained by first doing a gauge transformation to the time-independent gauge, evolving the system, and finally gauge-transforming back to the original gauge.

Although we have been assuming that $U(t)$ diagonalizes \bar{Q} , this is not necessary. Any time-independent unitary transformation multiplied to $U(t)$ can still make $\hat{\mathbf{H}}_F$ time independent. To make connection between the t_0 dependent Floquet Hamiltonian $\hat{\mathbf{H}}_{t_0}^F$ in Eq. B.30 and the effective Hamiltonian $\hat{\mathbf{H}}_F$, we use a minimal $U(t)$ that is independent of the basis of $\hat{\mathbf{H}}(t)$:

$$U_F(t) = \sum_m c_m e^{-im\omega t}, \quad (\text{B.39})$$

which is a time-dependent scalar function. In the matrix form of \bar{Q} , this $U_F(t)$ block-diagonalizes \bar{Q} . All the diagonal blocks have the form $H_F - m\hbar\omega \mathbf{1}$. Here we removed the hat of H_F to indicate that it is a matrix written in certain representation instead of an operator. In this particular representation or gauge, $|\alpha(t)\rangle = |\alpha\rangle U_F(t)$. We thus have

$$\hat{\mathbf{H}}_{t_0}^F = \sum_{\tilde{\epsilon}} |u_{\tilde{\epsilon}}(t_0)\rangle \tilde{\epsilon} \langle u_{\tilde{\epsilon}}(t_0)| = \sum_{\alpha\beta} U_F(t_0) |\alpha\rangle (H_F)_{\alpha\beta} \langle \beta| U_F^\dagger(t_0). \quad (\text{B.40})$$

Or loosely speaking $\hat{\mathbf{H}}_{t_0}^F = U_F(t_0) \hat{\mathbf{H}}_F U_F^\dagger(t_0)$. Therefore the t_0 dependence in $\hat{\mathbf{H}}_{t_0}^F$ is only due to a gauge transformation and is not physical. The complete information of time evolution can be obtained from H_F and U_F according to Eq. B.38.

In practice, to obtain the quasienergy spectrum or H_F we simply start from the eigenvalue problem Eq. B.21 for $\bar{Q} \equiv \bar{H} + \bar{Q}_0$, where $\bar{H}_{m,m+n} = H_n$ and $(\bar{Q}_0)_{m,m+n} = -m\hbar\omega \delta_{n0}$. We can either use perturbation theory and treat \bar{H} as perturbation, which is accurate in the high-frequency limit, or directly diagonalize \bar{Q} with a large enough cutoff. The first several terms in the perturbation series of H_F are given in Eqs. 86-89 in [77] (m there should be $-m$ in our notation).

B.4 High Frequency (Van Vleck) expansion from degenerate perturbation theory

In order to understand the effects of coherent time-periodic modulation of quantum systems, we need an efficient method to obtain the Floquet Hamiltonian $\hat{\mathbf{H}}^F$ for a given time-dependent Hamiltonian $\hat{\mathbf{H}}(\tau)$. Generally, for the Floquet systems, one would like to obtain a suitable Hamiltonian $\hat{\mathbf{H}}(\tau)$ given a desired static Hamiltonian $\hat{\mathbf{H}}_{\text{eff}}$. Usually the formal approach in making use of the full eigenstates of a time-dependent model Hamiltonian is not feasible in practice. Therefore, one requires an approximate scheme that still provides a valid description at least on the time-scales and energy-scales. Such an approach is provided by high-frequency approximations [77, 84–88]. Using the Van Vleck expansion within the degenerate perturbation theory as shown in Ref. [77], we can write the explicit expressions for the first few terms with $n = 0, 1, 2$ as required;

$$\begin{aligned}\hat{\mathbf{H}}^{F(0)} &= \hat{\mathbf{H}}_0, \\ \hat{\mathbf{H}}^{F(1)} &= \sum_{m \neq 0} \frac{[\hat{\mathbf{H}}_m, \hat{\mathbf{H}}_{-m}]}{m\hbar\omega}, \\ \hat{\mathbf{H}}^{F(2)} &= \sum_{m \neq 0} \left(\frac{[\hat{\mathbf{H}}_{-m}, [\hat{\mathbf{H}}_0, \hat{\mathbf{H}}_m]]}{2(m\hbar\omega)^2} + \sum_{m' \neq 0, m} \frac{[\hat{\mathbf{H}}_{-m'}, [\hat{\mathbf{H}}_{m'-m}, \hat{\mathbf{H}}_m]]}{3mm'(\hbar\omega)^2} \right).\end{aligned}\tag{B.41}$$

Expressions for higher orders can be found in the above equations and refs. [77, 84–88]. From a practical point of view, and in the cases which we will be considering, one often engineers the time-dependent Hamiltonian in such a way that the approximate Floquet Hamiltonian $\hat{\mathbf{H}}_{\text{eff}} = \sum_{n=0}^m H^{F(n)}$ corresponds to the desired model Hamiltonian of the effective systems.

Some of the commutators are related by transpose or Hermitian conjugate. As an example in $H^{F(2)}$ the transpose reduces the sum down by

$$\frac{[H_m, H_{-m}]}{m\hbar\omega} + \frac{[H_{-m}, H_m]}{-m\hbar\omega} = \frac{[H_m, H_{-m}]}{m\hbar\omega} + \frac{[H_m, H_{-m}]}{m\hbar\omega} \quad (\text{B.42})$$

$$= 2 \frac{[H_m, H_{-m}]}{m\hbar\omega} \quad (\text{B.43})$$

1359 Additionally, an example in $H^{F(3)}$ the Hermitian conjugate reduces the sum down by

$$\begin{aligned} [H_{-m'}, [H_{m'-m}, H_m]]^\dagger &= [[H_{m'-m}, H_m]^\dagger, H_{-m'}^\dagger] \\ &= [[H_m^\dagger, H_{m'-m}^\dagger], H_{m'}] \\ &= [[H_{-m}, H_{m-m'}], H_{m'}] \\ &= [H_{m'}, [H_{m-m'}, H_{-m}]] \end{aligned} \quad (\text{B.44})$$

1360 or in general the following identity

$$[A, [B, C]]^\dagger = [A^\dagger, [B^\dagger, C^\dagger]]. \quad (\text{B.45})$$

1361 With the symmetry in modes we have the following simplification

$$\frac{[H_{-m'}, [H_{m'-m}, H_m]]}{mm'(\hbar\omega)^2} + \frac{[H_{m'}, [H_{m-m'}, H_{-m}]]}{(-m)(-m')(\hbar\omega)^2} = \frac{[H_{-m'}, [H_{m'-m}, H_m]] + h.c.}{mm'(\hbar\omega)^2} \quad (\text{B.46})$$

We can reduce the second and third perturbation summation terms to

$$H^{F(2)} = \sum_{m>0} \frac{2[H_m, H_{-m}]}{m\hbar\omega} \quad (\text{B.47})$$

$$H^{F(3)} = \sum_{m>0} \left(\frac{[H_{-m}, [H_0, H_m]] + h.c.}{2(m\hbar\omega)^2} + \sum_{m' \neq m} \frac{[H_{-m'}, [H_{m'-m}, H_m]] + h.c.}{3mm'(\hbar\omega)^2} \right) \quad (\text{B.48})$$

1362 **B.4.1 Non-uniform circularly polarized light on Dirac**

1363 We start with the Dirac equation in 2D with a gauge potential

$$\mathcal{H}(t) = v_F \boldsymbol{\sigma} \cdot (\mathbf{p} + e\mathbf{A}(t)) \quad (\text{B.49})$$

1364 where $\mathbf{A}(t) = \frac{E}{\omega} \langle -\sin \omega t, \frac{1}{2} \sin(Kx) \cos(2\omega t) \rangle$. Which is made up of two electromagnetic wave
1365 sources. The time dependent Hamiltonian becomes

$$\mathcal{H}(t) = v_F \left(\sigma_x \left(p_x - \frac{eE}{\omega} \sin \omega t \right) + \sigma_y \left(p_y + \frac{eE}{2\omega} \sin(Kx) \cos(2\omega t) \right) \right), \quad (\text{B.50})$$

1366 Performing the Fourier time-transform from

$$H_n = \frac{1}{T} \int_0^T \mathcal{H}(t) e^{-in\omega t} dt \quad (\text{B.51})$$

1367 gives the following terms

$$H_0 = v_F \boldsymbol{\sigma} \cdot \mathbf{p} \quad (\text{B.52})$$

$$H_{\pm 1} = \pm \sigma_x \frac{i v_F e E}{2\omega} \quad (\text{B.53})$$

$$H_{\pm 2} = \sigma_y \frac{v_F e E}{4\omega} \sin(Kx). \quad (\text{B.54})$$

1368 We compute the following Hermitian commutators for the high-frequency expansion

$$[H_1, H_{-1}] \tag{B.55}$$

$$[H_2, H_{-2}] \tag{B.56}$$

$$[H_{-1}, [H_0, H_1]] \tag{B.57}$$

$$[H_{-2}, [H_0, H_2]] \tag{B.58}$$

$$[H_1, [H_{-2}, H_1]] \tag{B.59}$$

$$[H_{-1}, [H_{-1}, H_2]]. \tag{B.60}$$

1369 We find each term to be

$$[H_1, H_{-1}] = [H_2, H_{-2}] = 0 \tag{B.61}$$

$$H^{F(2)} = 0. \tag{B.62}$$

$$\begin{aligned}
[H_0, H_{\pm 1}] &= \pm \sigma_z \frac{v_F^2 e E}{\omega} p_y \\
[H_1, [H_0, H_{-1}]] &= -\sigma_y \frac{v_F^3 e^2 E^2}{\omega^2} p_y
\end{aligned} \tag{B.63}$$

$$\begin{aligned}
[H_0, H_{\pm 2}] &= \pm i \sigma_z \frac{v_F^2 e E}{4\omega} (p_x \sin(Kx) + \sin(Kx) p_x) \\
[H_2, [H_0, H_{-2}]] &= -\sigma_x \frac{v_F^3 e^2 E^2}{2\omega^2} (p_x \sin^2(Kx) + \sin^2(Kx) p_x)
\end{aligned} \tag{B.64}$$

$$\begin{aligned}
[H_{\pm 1}, H_2] &= \mp \sigma_z \left(\frac{v_F e E}{2\omega} \right)^2 \sin(Kx) \\
[H_1, [H_{-2}, H_{-1}]] &= -\sigma_y \frac{v_F^3 e^3 E^3}{4\omega^3} \sin(Kx)
\end{aligned} \tag{B.65}$$

$$[H_{-1}, [H_{-1}, H_2]] = \sigma_y \frac{v_F^3 e^3 E^3}{4\omega^3} \sin(Kx) \tag{B.66}$$

1370 Piecing each term together

$$\begin{aligned}
H^{F(3)} &= \frac{[H_1, [H_0, H_{-1}]]}{2\hbar^2 \omega^2} + \frac{[H_{-2}, [H_0, H_2]]}{8\hbar^2 \omega^2} - \frac{[H_1, [H_{-2}, H_1]]}{3\hbar^2 \omega^2} + \frac{[H_{-1}, [H_{-1}, H_2]]}{6\hbar^2 \omega^2} + h.c. \\
&= -\sigma_y \frac{v_F^3 e^2 E^2}{\hbar^2 \omega^4} p_y - \sigma_x \frac{v_F^3 e^2 E^2}{8\hbar^2 \omega^4} \{p_x, \sin^2(Kx)\} + \sigma_y \frac{v_F^3 e^3 E^3}{4\hbar^2 \omega^5} \sin(Kx).
\end{aligned} \tag{B.67}$$

1371 The full Hamiltonian to second order in $\hbar\omega$ becomes

$$H_{\text{eff}} = v_F \boldsymbol{\sigma} \cdot \mathbf{p} - \sigma_y \frac{v_F^3 e^2 E^2}{\hbar^2 \omega^4} p_y - \sigma_x \frac{v_F^3 e^2 E^2}{8\hbar^2 \omega^4} \{p_x, \sin^2(Kx)\} + \sigma_y \frac{v_F^3 e^3 E^3}{4\hbar^2 \omega^5} \sin(Kx). \tag{B.68}$$

1372 **B.4.2 Non-uniform circularly polarized light on 2DEG**

1373 We start with the Schrodinger equation in 2D with a gauge potential field

$$\mathcal{H}(t) = \frac{(\mathbf{p} + e\mathbf{A}(t))^2}{2m^*} \quad (\text{B.69})$$

1374 where $\mathbf{A}(t) = \frac{E}{\omega} \langle -\sin \omega t, \cos(Kx) \cos \omega t \rangle$. Which is made up of two electromagnetic wave sources.

1375 The time dependent Hamiltonian becomes

$$\begin{aligned} \mathcal{H}(t) = \frac{1}{2m^*} & \left[p_x^2 + p_y^2 + \frac{e^2 E^2}{2\omega^2} (1 + \cos^2(Kx)) + \frac{e^2 E^2}{2\omega^2} \sin^2(Kx) \cos 2\omega t \right. \\ & \left. + \frac{2eE}{\omega} p_y \cos(Kx) \cos \omega t - \frac{2eE}{\omega} p_x \sin \omega t \right] \end{aligned} \quad (\text{B.70})$$

1376 Performing the Fourier time-transform from

$$H_n = \frac{1}{T} \int_0^T \mathcal{H}(t) e^{-in\omega t} dt \quad (\text{B.71})$$

1377 gives the following terms

$$H_0 = \frac{1}{2m^*} \left(p_x^2 + p_y^2 + \frac{e^2 E^2}{2\omega^2} (1 + \cos^2(Kx)) \right) \quad (\text{B.72})$$

$$H_{\pm 1} = \frac{1}{2m^*} \frac{eE}{\omega} (\pm i p_x + p_y \cos(Kx)) \quad (\text{B.73})$$

$$H_{\pm 2} = -\frac{1}{2m^*} \frac{e^2 E^2}{4\omega^2} \sin^2(Kx) \quad (\text{B.74})$$

1378 We compute the following Hermitian commutators for the high-frequency expansion

$$[H_1, H_{-1}] = -\frac{1}{2m^*} \frac{\hbar K e^2 E^2}{\omega^2} p_y \sin(Kx) \quad (\text{B.75})$$

$$[H_2, H_{-2}] = 0 \quad (\text{B.76})$$

1379 then

$$H^{F(2)} = \frac{2[H_1, H_{-1}]}{\hbar\omega} = -\frac{1}{2m^*} \frac{2Ke^2E^2}{\omega^3} p_y \sin(Kx) \quad (\text{B.77})$$

1380 The full Hamiltonian to first order in $\hbar\omega$ becomes

$$H_{\text{eff}} = \frac{1}{2m^*} \left(p_x^2 + p_y^2 + \frac{e^2E^2}{2\omega^2} (1 + \cos^2(Kx)) - \frac{2Ke^2E^2}{\omega^3} p_y \sin(Kx) \right). \quad (\text{B.78})$$

1381 We can further manipulate by shifting the energy by a constant and completing the square w.r.t.

1382 p_y and $\sin(Kx)$ terms to get

$$H_{\text{eff}} = \frac{1}{2m^*} \left(p_x^2 + \left(p_y - \frac{Ke^2E^2}{m^*\omega^3} \sin(Kx) \right)^2 + \frac{e^2E^2}{2\omega^2} \cos^2(Kx) - \frac{K^2e^4E^4}{m^{*2}\omega^6} \sin^2(Kx) \right). \quad (\text{B.79})$$

1383 **B.5 Tight-binding model Dirac**

1384 We start with a nearest-neighbor single-orbital tight-binding Hamiltonian

$$\mathcal{H} = - \sum_{jl\alpha, j'l'\beta} hc_{jl\alpha}^\dagger c_{j'l'\beta} + h.c. \quad (\text{B.80})$$

1385 The incident laser beam in vector potential forms looks like

$$\mathbf{A}(\mathbf{r}, t) = \frac{E}{\omega} \langle -\sin\omega t, \frac{1}{2} \sin(Kx) \cos 2\omega t \rangle. \quad (\text{B.81})$$

1386 Using the following approximation for smoothly varying vector potential fields

$$\int_{\mathbf{r}_{j,l}^\alpha}^{\mathbf{r}_{j',l'}^\beta} \mathbf{A}(\mathbf{r}, t) \cdot d\mathbf{l} \approx \mathbf{A} \left(\frac{\mathbf{r}_{j',l'}^\beta + \mathbf{r}_{j,l}^\alpha}{2}, t \right) \cdot (\mathbf{r}_{j',l'}^\beta - \mathbf{r}_{j,l}^\alpha) \quad (\text{B.82})$$

1387 where

$$\mathbf{a}_1 = \sqrt{3}a\hat{\mathbf{x}} \quad (\text{B.83})$$

$$\mathbf{a}_2 = 3a\hat{\mathbf{y}} \quad (\text{B.84})$$

$$\mathbf{r}_{jl}^{A_1} = j\mathbf{a}_1 + l\mathbf{a}_2 \quad (\text{B.85})$$

$$\mathbf{r}_{jl}^{B_1} = (j + \frac{1}{2})\mathbf{a}_1 + (l + \frac{1}{6})\mathbf{a}_2 \quad (\text{B.86})$$

$$\mathbf{r}_{jl}^{A_2} = (j + \frac{1}{2})\mathbf{a}_1 + (l + \frac{1}{2})\mathbf{a}_2 \quad (\text{B.87})$$

$$\mathbf{r}_{jl}^{B_2} = (j + 1)\mathbf{a}_1 + (l + \frac{2}{3})\mathbf{a}_2. \quad (\text{B.88})$$

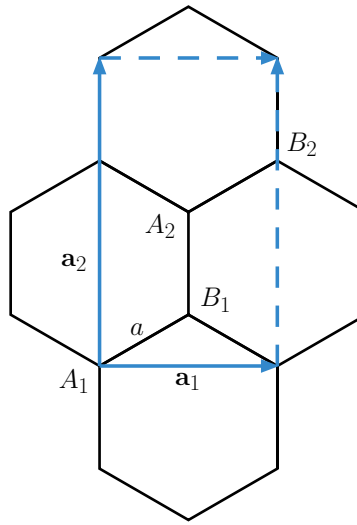


Figure B.1: Unit cell for dirac system with gauge potential with translation symmetry in the y - axis described by Eq. (B.81).

$$\begin{aligned}
\mathcal{H}(t) = & - \sum_{jl} h_{jlA_1}^{j l B_1}(t) c_{jlA_1}^\dagger c_{jlB_1} + h_{jlB_1}^{j l A_2}(t) c_{jlB_1}^\dagger c_{jlA_2} + h_{jlA_2}^{j l B_2}(t) c_{jlA_2}^\dagger c_{jlB_2} \\
& + h_{jlB_1}^{j+1, l A_1}(t) c_{jlB_1}^\dagger c_{j+1, l A_1} + h_{jlB_2}^{j+1, l, A_2}(t) c_{jlB_2}^\dagger c_{j+1, l A_2}(t) \\
& + h_{jlB_2}^{j+1, l+1, A_1}(t) c_{jlB_2}^\dagger c_{j+1, l+1, A_1} + h.c.
\end{aligned} \tag{B.89}$$

1389 where in general

$$h_{jl\alpha}^{j'l'\beta}(t) \approx h \exp \left[i\phi_0 \left(-\frac{x_{j'l'}^\beta - x_{jl}^\alpha}{a} \sin \omega t + \frac{y_{j'l'}^\beta - y_{jl}^\alpha}{2a} \cos \left(K \frac{x_{j'l'}^\beta + x_{jl}^\alpha}{2} \right) \cos 2\omega t \right) \right], \tag{B.90}$$

1390 where $\phi_0 = eE/(\hbar\omega)$. More explicitly for each term

$$h_{jlA_1}^{j l B_1}(t) \approx h \exp \left[i\phi_0 \left(-\frac{\sqrt{3}}{2} \sin \omega t + \frac{1}{4} \sin \left(\sqrt{3} K a (j + \frac{1}{4}) \right) \cos 2\omega t \right) \right] \tag{B.91}$$

$$h_{jlB_1}^{j l A_2}(t) \approx h \exp \left[i\phi_0 \left(\frac{1}{2} \sin \left(\sqrt{3} K a (j + \frac{1}{2}) \right) \cos 2\omega t \right) \right] \tag{B.92}$$

$$h_{jlA_2}^{j l B_2}(t) \approx h \exp \left[i\phi_0 \left(-\frac{\sqrt{3}}{2} \sin \omega t + \frac{1}{4} \sin \left(\sqrt{3} K a (j + \frac{3}{4}) \right) \cos 2\omega t \right) \right] \tag{B.93}$$

$$h_{jlB_1}^{j+1, l A_1}(t) \approx h \exp \left[i\phi_0 \left(-\frac{\sqrt{3}}{2} \sin \omega t - \frac{1}{4} \sin \left(\sqrt{3} K a (j + \frac{3}{4}) \right) \cos 2\omega t \right) \right] \tag{B.94}$$

$$h_{jlB_2}^{j+1, l A_2}(t) \approx h \exp \left[i\phi_0 \left(-\frac{\sqrt{3}}{2} \sin \omega t - \frac{1}{4} \sin \left(\sqrt{3} K a (j + \frac{5}{4}) \right) \cos 2\omega t \right) \right] \tag{B.95}$$

$$h_{jlB_2}^{j+1, l+1, A_1}(t) \approx h \exp \left[i\phi_0 \left(\frac{1}{2} \sin \left(\sqrt{3} K a (j + 1) \right) \cos 2\omega t \right) \right] \tag{B.96}$$

1391 The incident laser beam allows for translation symmetry along the y-axis, so we can reduce
 1392 the dimension of the Hamiltonian with the following Fourier transform

$$c_{jl\alpha}^\dagger = \frac{1}{N_y} \sum_k c_{jk\alpha}^\dagger e^{ik\hat{y} \cdot \mathbf{R}_l} = \frac{1}{N_y} \sum_k c_{jk\alpha}^\dagger e^{ik(3la)} \quad (\text{B.97})$$

1393 The Hamiltonian then becomes

$$\begin{aligned} \mathcal{H}(t) = & - \sum_{jk} h_{jlA_1}^{jLB_1}(t) c_{jkA_1}^\dagger c_{jkB_1} + h_{jlB_1}^{jLA_2}(t) c_{jkB_1}^\dagger c_{jkA_2} + h_{jlA_2}^{jLB_2}(t) c_{jkA_2}^\dagger c_{jkB_2} \\ & + h_{jlB_1}^{j+1,LA_1}(t) c_{jkB_1}^\dagger c_{j+1,kA_1} + h_{jlB_2}^{j+1,L,A_2}(t) c_{jkB_2}^\dagger c_{j+1,kA_2}(t) \\ & + h_{jlB_2}^{j+1,l+1,A_1}(t) e^{-i3ka} c_{jkB_2}^\dagger c_{j+1,kA_1} + h.c. \end{aligned} \quad (\text{B.98})$$

1394 Making use of Floquet theory we can make the Hamiltonian time-independent with the
 1395 following time domain Fourier transform

$$H_{ab,n,k} = \frac{1}{2\pi} \int_0^{2\pi} \mathcal{H}_{ab}(k, t) e^{-in\tau} d\tau \quad (\text{B.99})$$

1396 where a, b represent the matrix indes of the previous Hamiltonian and n is the n -th order mode
 1397 of light. Each term has the general following form

$$H_{ab,n,k} = \frac{1}{2\pi} \int_0^{2\pi} e^{iZ_1 \sin \tau + iZ_2 \cos 2\tau - in\tau} d\tau \quad (\text{B.100})$$

1398 which looks a lot like the Hansen-Bessel integral function. However, because of the linear com-
 1399 bination of $\sin \tau$ and $\cos 2\tau$, there is no elementary solution to the integral as currently defined.
 1400 We thus solve the integral numerically for each given n . After the time domain Fourier trans-
 1401 form the Hamiltonian can be reduced to the following matrix form

$$H_n = - \sum_{jk} \left[\Psi_{jk}^\dagger H_{jj} \Psi_{jk} + \Psi_{jk}^\dagger H'_{j,j+1,k} \Psi_{j+1,k} + h.c. \right] \quad (\text{B.101})$$

$$H_{j,j} = \begin{bmatrix} 0 & 0 & 0 & 0 \\ h_{jlB_1}^{jLA_1} & 0 & 0 & 0 \\ 0 & h_{jlA_2}^{jLB_1} & 0 & 0 \\ 0 & 0 & h_{jlB_2}^{jLA_2} & 0 \end{bmatrix}$$

1402 and

$$H'_{j,j+,k} = \begin{bmatrix} 0 & h_{jlB_1}^{j+1,LA_1} & 0 & h_{jlB_2}^{j+1,L+1,A_1} e^{i\mathbf{k} \cdot \mathbf{a}_2} \\ 0 & 0 & 0 & 0 \\ 0 & 0 & 0 & h_{jlB_2}^{j+1,LA_2} \\ 0 & 0 & 0 & 0 \end{bmatrix},$$

1403 with $\mathbf{k} = k\hat{\mathbf{y}}$ and $\Psi_{jk} = [c_{jkA_1}, c_{jkB_1}, c_{jkA_2}, c_{jkB_2}]^T$.

1404 The quasienergy energy matrix has elements $Q_{m,m+n} = H_n - m\hbar\omega\delta_{n0}$. We choose a cutoff
 1405 for mode m , $|m| \leq m_c$, where m_c is a positive integer. This cuts the matrix down to have $N_m =$
 1406 $2m_c + 1$ diagonal blocks, where each block is of size a $N_S = 2r_c + 1$ square matrix, H_n , and r_c is
 1407 the cutoff radius of unit cells. The matrix can be solved using an eigenvalue solver, producing
 1408 $N_m N_S$ eigenenergies and eigenvectors for a given electric field strength E . It is difficult to glean
 1409 any information from looking at all the energies but one can do a projection to the $m = 0$ mode
 1410 to highlight which energies belong to it. This is still not all that imformative because when using
 1411 a finite system we discretize the brillouin zone uniformly and it does not necessarily mean we
 1412 are picking energy values close to the folded in Dirac point, since the unperturbed brillouin
 1413 zone gets folded into the perturbed smaller brillouin zone.

1414 B.6 Tight-binding model 2DEG

1415 We start with a nearest-neighbor single-orbital tight-binding Hamiltonian on a square lat-
 1416 tice

$$\mathcal{H} = \sum_{j,l} -h(c_{j,l}^\dagger c_{j+1,l} + c_{j,l}^\dagger c_{j,l+1} + h.c.) \quad (\text{B.102})$$

1417 The incident laser beam as a vector potential is as follows

$$\mathbf{A}(\mathbf{r}, t) = \frac{E}{\omega} \langle -\sin \omega t, \cos(Kx) \cos \omega t \rangle. \quad (\text{B.103})$$

1418 Using the following approximation for smoothly varying vector potential fields

$$\int_{\mathbf{r}_a}^{\mathbf{r}_b} \mathbf{A}(\mathbf{r}, t) \cdot d\mathbf{l} \approx \mathbf{A}\left(\frac{\mathbf{r}_b + \mathbf{r}_a}{2}, t\right) \cdot (\mathbf{r}_b - \mathbf{r}_a) \quad (\text{B.104})$$

1419 and using Peierls substitution the Hamiltonian becomes

$$\mathcal{H}(t) = - \sum_{j,l} (h_{j,j+1}(t) c_{j,l}^\dagger c_{j+1,l} + h_{l,l+1}(t) c_{j,l}^\dagger c_{j,l+1} + h.c.), \quad (\text{B.105})$$

1420 where

$$\begin{aligned} h_{j,j+1}(t) &\approx h \exp\left(-i \frac{eEa}{\hbar\omega} \frac{x_{j+1} - x_j}{a} \sin \omega t\right) \\ &= h \exp(-i\phi_0 \sin \omega t) \end{aligned} \quad (\text{B.106})$$

$$\begin{aligned} h_{l,l+1}(t) &\approx h \exp\left(i \frac{eEa}{\hbar\omega} \frac{y_{l+1} - y_l}{a} \cos(Kx_j) \cos \omega t\right) \\ &= h \exp(i\phi_0 \cos(Kx_j) \cos \omega t). \end{aligned} \quad (\text{B.107})$$

1421 The incident laser beam allows for translation symmetry along the y-axis, so we can reduce
1422 the dimension of the Hamiltonian with the following Fourier transform

$$c_{j,l}^\dagger = \frac{1}{\sqrt{N_y}} \sum_k c_{j,k}^\dagger e^{ik\hat{\mathbf{y}} \cdot \mathbf{r}_l} = \frac{1}{\sqrt{N_y}} \sum_k c_{j,k}^\dagger e^{ikla}. \quad (\text{B.108})$$

1423 The Hamiltonian then becomes

$$\mathcal{H}(t) = \sum_{j,k} (h_{l,l+1}(t)e^{-ika} + h_{l,l+1}^*(t)e^{ika})c_{j,k}^\dagger c_{j,k} + (h_{j,j+1}(t)c_{j,k}^\dagger c_{j+1,k} + h.c.) \quad (\text{B.109})$$

$$= \sum_{j,k} 2h \cos(\phi_0 \cos(Kx_j) \cos \omega t - ka) c_{j,k}^\dagger c_{j,k} + (he^{i\phi_0 \sin \omega t} c_{j,k}^\dagger c_{j+1,k} + h.c.). \quad (\text{B.110})$$

1424 Making use of Floquet theory we can make the Hamiltonian time-independent with the follow-
1425 ing time Fourier transform

$$\mathcal{H}_{ab,n}(k) = \frac{1}{T} \int_0^T \mathcal{H}_{ab}(k, t) e^{-in\omega t} dt \quad (\text{B.111})$$

$$= \frac{1}{2\pi} \int_0^{2\pi} \mathcal{H}_{ab}(k, t) e^{-in\tau} d\tau \quad (\text{B.112})$$

1426 where a, b represent the matrix index of the previous Hamiltonian and n is the n -th order mode
1427 of light. We will make use of the following Hansen-Bessel integral formulas

$$J_n(z) = \frac{1}{2\pi} \int_0^{2\pi} e^{in\tau - z \sin \tau} d\tau = \frac{1}{2\pi} \int_0^{2\pi} e^{in\tau - in\pi/2 + z \cos \tau} d\tau, \quad (\text{B.113})$$

1428 note that the integral bound can be the same due to the integrand being periodic from $[0, 2\pi]$.
1429 Recall, Bessel function identities for $n \in \mathbb{Z}$

$$J_n(-z) = (-1)^n J_n(z) \quad (\text{B.114})$$

$$J_{-n}(z) = (-1)^n J_n(z) \quad (\text{B.115})$$

1430 The terms for given k become the following time Fourier transforms

$$\begin{aligned}
\mathcal{H}_{j,j,n}(k) &= -\frac{h}{2\pi} \int_0^{2\pi} \left(e^{i\phi_0 \cos(Kx_j) \cos \tau - ika - in\tau} + e^{-i\phi_0 \cos(Kx_j) \cos \tau + ika - in\tau} \right) d\tau \\
&= -h \left(\frac{e^{-ika}}{2\pi} \int_0^{2\pi} e^{iz \cos \tau - in\tau} d\tau + \frac{e^{ika}}{2\pi} \int_0^{2\pi} e^{-iz \cos \tau - in\tau} d\tau \right) \\
&= -h \left(\frac{e^{-ika - in\pi/2}}{2\pi} \int_0^{2\pi} e^{iz \cos \tau - in\tau + in\pi/2} d\tau + \frac{e^{ika - in\pi/2}}{2\pi} \int_0^{2\pi} e^{-iz \cos \tau - in\tau + in\pi/2} d\tau \right) \\
&= -he^{-in\pi/2} \left(J_{-n}(z) e^{-ika} + J_{-n}(-z) e^{ika} \right) \\
&= -hJ_n(z) e^{-in\pi/2} (e^{ika} + e^{-ika + in\pi}) \\
&= -hJ_n(z) (e^{i(ka - n\pi/2)} + e^{-i(ka - n\pi/2)}) \\
&= -2hJ_n(\phi_0 \cos(Kx_j)) \cos(ka - n\pi/2)
\end{aligned} \tag{B.116}$$

1431 and

$$\begin{aligned}
\mathcal{H}_{j,j+1,n} &= -\frac{h}{2\pi} \int_0^{2\pi} e^{-i\phi_0 \sin \tau - in\tau} d\tau \\
&= -hJ_{-n}(\phi_0) \\
&= -h(-1)^n J_n(\phi_0)
\end{aligned} \tag{B.117}$$

$$\begin{aligned}
\mathcal{H}_{j+1,j,n} &= -\frac{h}{2\pi} \int_0^{2\pi} e^{i\phi_0 \sin \tau - in\tau} d\tau \\
&= -hJ_{-n}(-\phi_0) \\
&= -hJ_n(\phi_0)
\end{aligned} \tag{B.118}$$

1432 This completes finding all the matrix terms for the quasienergy matrix \bar{Q} for a 2DEG tight
1433 binding model with incident inhomogeneous laser light.

B.7 Chern number of Landau levels

In this section we discuss how to understand the Chern number of Landau levels. For two-dimensional periodic systems, the 2D Brillouin zone is a closed manifold, and one can define the Chern number as a topological invariant for the mapping between complex functions (ground state wavefunctions) and this manifold. However, for Landau levels the system does not have translational symmetry which causes a conceptual difficulty in defining Chern numbers.

To address this difficulty, let us start from the Chern number of typical 2D Bloch Hamiltonians. The Berry curvature of band n at crystal momentum \mathbf{k} is defined as

$$\Omega_{n\mathbf{k}} = \hat{\mathbf{z}} \cdot (\nabla_{\mathbf{k}} \times \mathbf{A}_{n\mathbf{k}}) = \hat{\mathbf{z}} \cdot (\nabla_{\mathbf{k}} \times \langle u_{n\mathbf{k}} | i \nabla_{\mathbf{k}} | u_{n\mathbf{k}} \rangle) \quad (\text{B.119})$$

The Chern number for band n , which must not touch other bands throughout the Brillouin zone, is defined as

$$C_n = \int \frac{d^2\mathbf{k}}{2\pi} \Omega_{n\mathbf{k}} \quad (\text{B.120})$$

However, according to Eq. (B.119), C_n can be rewritten into

$$\begin{aligned} C_n &= \int \frac{d^2\mathbf{k}}{2\pi} \partial_{k_x} \langle u_{n\mathbf{k}} | i \partial_{k_y} | u_{n\mathbf{k}} \rangle - \int \frac{d^2\mathbf{k}}{2\pi} \partial_{k_y} \langle u_{n\mathbf{k}} | i \partial_{k_x} | u_{n\mathbf{k}} \rangle \\ &= \frac{1}{2\pi} \int dk_x \partial_{k_x} \int dk_y \langle u_{n\mathbf{k}} | i \partial_{k_y} | u_{n\mathbf{k}} \rangle - \frac{1}{2\pi} \int dk_y \partial_{k_y} \int dk_x \langle u_{n\mathbf{k}} | i \partial_{k_x} | u_{n\mathbf{k}} \rangle \end{aligned} \quad (\text{B.121})$$

1446 It is worth noting that the last result is related to the expectation value of polarization (or posi-
 1447 tion operator) in a Bloch state:

$$\begin{aligned}
 \langle n\mathbf{k}|\mathbf{r}|n'\mathbf{k}'\rangle &= \int d^2\mathbf{r} \psi_{n'\mathbf{k}'}^\dagger(\mathbf{r}) \mathbf{r} \psi_{n\mathbf{k}}(\mathbf{r}) \\
 &= \int d^2\mathbf{r} u_{n\mathbf{k}}^\dagger(\mathbf{r}) e^{-i\mathbf{k}\cdot\mathbf{r}} \mathbf{r} e^{i\mathbf{k}'\cdot\mathbf{r}} u_{n'\mathbf{k}'}(\mathbf{r}) \\
 &= \int d^2\mathbf{r} u_{n\mathbf{k}}^\dagger(\mathbf{r}) e^{-i\mathbf{k}\cdot\mathbf{r}} (-i\partial_{\mathbf{k}'} e^{i\mathbf{k}'\cdot\mathbf{r}}) u_{n'\mathbf{k}'}(\mathbf{r}) \\
 &= -i\partial_{\mathbf{k}'} \langle n\mathbf{k}|n'\mathbf{k}'\rangle + \int d^2\mathbf{r} u_{n\mathbf{k}}^\dagger(\mathbf{r}) e^{-i\mathbf{k}\cdot\mathbf{r}} e^{i\mathbf{k}'\cdot\mathbf{r}} [i\partial_{\mathbf{k}'} u_{n'\mathbf{k}'}(\mathbf{r})] \\
 &= -i\delta_{nn'} \frac{(2\pi)^2}{V_{\text{uc}}} \partial_{\mathbf{k}'} \delta(\mathbf{k}-\mathbf{k}') + \int d^2\mathbf{r} u_{n\mathbf{k}}^\dagger(\mathbf{r}) e^{-i\mathbf{k}\cdot\mathbf{r}} e^{i\mathbf{k}'\cdot\mathbf{r}} [i\partial_{\mathbf{k}'} u_{n'\mathbf{k}'}(\mathbf{r})] \\
 &= -i\delta_{nn'} \frac{(2\pi)^2}{V_{\text{uc}}} \partial_{\mathbf{k}'} \delta(\mathbf{k}-\mathbf{k}') + \sum_{\mathbf{R}} \int_{\text{uc}} d^2\mathbf{r} u_{n\mathbf{k}}^\dagger(\mathbf{r}) e^{i(\mathbf{k}'-\mathbf{k})\cdot\mathbf{r}} [i\partial_{\mathbf{k}'} u_{n'\mathbf{k}'}(\mathbf{r})] e^{i(\mathbf{k}'-\mathbf{k})\cdot\mathbf{R}} \\
 &= -i\delta_{nn'} \frac{(2\pi)^2}{V_{\text{uc}}} \partial_{\mathbf{k}'} \delta(\mathbf{k}-\mathbf{k}') + \frac{(2\pi)^2}{V_{\text{uc}}} \delta(\mathbf{k}-\mathbf{k}') \int_{\text{uc}} d^2\mathbf{r} u_{n\mathbf{k}}^\dagger(\mathbf{r}) [i\partial_{\mathbf{k}'} u_{n'\mathbf{k}'}(\mathbf{r})] e^{i(\mathbf{k}'-\mathbf{k})\cdot\mathbf{R}} \\
 &= \frac{(2\pi)^2}{V_{\text{uc}}} [i\delta_{nn'} \partial_{\mathbf{k}} \delta(\mathbf{k}-\mathbf{k}') + \langle u_{n\mathbf{k}}|i\partial_{\mathbf{k}}|u_{n'\mathbf{k}'}\rangle \delta(\mathbf{k}-\mathbf{k}')]
 \end{aligned} \tag{B.122}$$

1448 where we have used the normalization condition of 2D Bloch states $\langle n\mathbf{k}|n'\mathbf{k}'\rangle = \delta_{nn'} \frac{(2\pi)^2}{V_{\text{uc}}} \delta(\mathbf{k}-\mathbf{k}')$
 1449 with V_{uc} the unit cell volume or area. The above result means that

$$\begin{aligned}
 \frac{a_y}{2\pi} \int dk_y \langle n\mathbf{k}|\mathbf{r}|n\mathbf{k}\rangle &\equiv N \mathbf{r}_n(k_x) = \frac{a_y}{2\pi} \int dk_y \lim_{\mathbf{k}' \rightarrow \mathbf{k}} \langle n\mathbf{k}|\mathbf{r}|n\mathbf{k}'\rangle \\
 &= \frac{a_y}{2\pi} N \int dk_y \langle u_{n\mathbf{k}}|i\partial_{\mathbf{k}}|u_{n\mathbf{k}}\rangle
 \end{aligned} \tag{B.123}$$

1450 where a_y is the lattice constant along y . Namely

$$\frac{1}{2\pi} \int dk_y \langle u_{n\mathbf{k}}|i\partial_{\mathbf{k}}|u_{n\mathbf{k}}\rangle = \frac{\mathbf{r}_n(k_x)}{a_y}. \tag{B.124}$$

1451 Therefore

$$\begin{aligned}
C_n &= \frac{1}{a_y} \int dk_x \partial_{k_x} y_n(k_x) - \frac{1}{a_x} \int dk_y \partial_{k_y} x_n(k_y) \\
&= \frac{1}{a_y} \left[y_n|_{k_x=\frac{2\pi}{a_x}} - y_n|_{k_x=0} \right] - \frac{1}{a_x} \left[x_n|_{k_y=\frac{2\pi}{a_x}} - x_n|_{k_y=0} \right] \\
&\equiv \frac{\Delta y_n}{a_y} - \frac{\Delta x_n}{a_x}
\end{aligned} \tag{B.125}$$

1452 In other words, the Chern number can be understood as an effect of adiabatic pumping. The
1453 parameter defining the pump is k_x (1st term in the above equation) or k_y (2nd term in the above
1454 equation). When the pumping parameter increases by a period, the expectation value of the
1455 position operator y_n (or x_n) for the given band does not necessarily return to itself. A nonzero
1456 change leads to the finite Chern number. A caveat that is not mentioned in many references
1457 or textbooks is that since $\mathbf{A}_{n\mathbf{k}}$ is not a gauge invariant quantity, the two individual terms in the
1458 last line of Eq. (B.125) are not separately well defined. Instead, one can choose a gauge so that
1459 $A_x(k_y=0) = A_x(k_y=\frac{2\pi}{a_y})$ [but $A_y(k_x=0) \neq A_y(k_x=\frac{2\pi}{a_x})$, since otherwise C_n always vanishes], so
1460 that

$$C_n = \frac{\Delta y_n}{a_y}, \quad A_x\left(k_y + \frac{2\pi}{a_y}\right) = A_x(k_y) \tag{B.126}$$

1461 In this manner, the Chern number is equivalent to the change of the y -component of the center-
1462 of-mass position of the given Bloch state, when k_x changes by $2\pi/a_x$.

1463 The above adiabatic pumping understanding of the Chern number can now be used to de-
1464 fine the Chern number of Landau levels, for which the Hamiltonian can only be made transla-
1465 tion invariant along one direction. The Landau level Hamiltonian for a uniform magnetic field
1466 $B\hat{\mathbf{z}} = \nabla \times (Bx\hat{\mathbf{y}}) = \nabla \times \mathbf{A}$ is

$$H = \frac{p_x^2}{2m} + \frac{(p_y + eBx)^2}{2m} \tag{B.127}$$

1467 Assuming the eigenfunctions are $\psi(x, y)$, we can first make use of the translation symmetry
 1468 along y to define

$$\psi(x, y) = \frac{1}{2\pi} \int dk \phi(x, k) e^{iky} \quad (\text{B.128})$$

1469 The inverse transform is

$$\psi(x, k) = \int dy \psi(x, y) e^{-iky} \quad (\text{B.129})$$

1470 which is consistent with the direct transform since

$$\begin{aligned} \psi(x, k) &= \int dy \frac{1}{2\pi} \int dk' \phi(x, k') e^{i(k'-k)y} \\ &= \int dk' \phi(x, k') \delta(k' - k) = \phi(x, k) \end{aligned} \quad (\text{B.130})$$

1471 Here we assume the wave functions are normalized as

$$\int d^2\mathbf{r} \psi^\dagger(x, y) \psi(x, y) = 1 \quad (\text{B.131})$$

1472 which means

$$\begin{aligned} 1 &= \frac{1}{(2\pi)^2} \int d^2\mathbf{r} \int dk \int dk' \phi^\dagger(x, k) \phi(x, k') e^{i(k'-k)y} \\ &= \frac{1}{(2\pi)^2} \int dx \int dk \int dk' \phi^\dagger(x, k) \phi(x, k') 2\pi \delta(k' - k) \\ &= \frac{1}{2\pi} \int dx \int dk \phi^\dagger(x, k) \phi(x, k) \\ &= \int \frac{dk}{2\pi} \langle \phi(k) | \phi(k) \rangle \end{aligned} \quad (\text{B.132})$$

The k -dependent Hamiltonian is

$$\begin{aligned} H_k = e^{-iky} H e^{iky} &= \frac{p_x^2}{2m} + \frac{(\hbar k + eBx)^2}{2m} \\ &= \frac{p_x^2}{2m} + \frac{1}{2} m \left(\frac{eB}{m} \right)^2 \left(x + \frac{\hbar k}{eB} \right)^2 \end{aligned} \quad (\text{B.133})$$

1474 which is a quantum harmonic oscillator with $\omega = eB/m \equiv \omega_c$. The eigensolutions are

$$\begin{aligned} H_k \phi_n(x, k) &= \hbar \omega \left(n + \frac{1}{2} \right) \phi_n(x, k), \\ \phi_n(x, k) &= \frac{1}{\sqrt{2^n n!}} \left(\frac{m\omega_c}{\hbar\pi} \right)^{\frac{1}{4}} e^{-\frac{m\omega_c(x-x_k)^2}{2\hbar}} H_n \left[\sqrt{\frac{m\omega}{\hbar}} (x - x_k) \right] \end{aligned} \quad (\text{B.134})$$

1475 where H_n are the Hermite polynomials and $x_k \equiv -\frac{\hbar k}{eB}$. However, the above ϕ_n are normalized as

$$\int dx \phi_n^*(x, k) \phi_n(x, k) = 1 \quad (\text{B.135})$$

1476 incompatible with our earlier definition in Eq. (B.132). To this end we choose a cutoff for the k

1477 integral and replace the normalization condition in Eq. (B.132) as

$$1 = \frac{1}{2\pi} \int_{-\frac{\pi}{a_y}}^{\frac{\pi}{a_y}} dk \langle \phi(k) | \phi(k) \rangle \quad (\text{B.136})$$

1478 Since $\phi_n(x, k)$ depends on k only through a shift of x , we have

$$\frac{1}{2\pi} \int_{-\frac{\pi}{a_y}}^{\frac{\pi}{a_y}} dk \langle \phi_n(k) | \phi_n(k) \rangle = \frac{1}{a_y} \langle \phi_n(k=0) | \phi_n(k=0) \rangle \equiv \frac{1}{a_y} \langle \phi_n | \phi_n \rangle = \frac{1}{a_y} \quad (\text{B.137})$$

1479 This means that the ϕ_n should be redefined so that Eq. (B.136) is satisfied:

$$\begin{aligned} \phi_n(x, k) &= \frac{\sqrt{a_y}}{\sqrt{2^n n!}} \left(\frac{m\omega_c}{\hbar\pi} \right)^{\frac{1}{4}} e^{-\frac{m\omega_c(x-x_k)^2}{2\hbar}} H_n \left[\sqrt{\frac{m\omega}{\hbar}} (x - x_k) \right] \\ \langle \phi_n | \phi_n \rangle &= a_y \end{aligned} \quad (\text{B.138})$$

1480 We can now try to use the above interpretation of the Chern number to check if Landau
 1481 levels indeed have $C = 1$. To this end we would rewrite Eq. (B.125) assuming k as a pumping pa-
 1482 rameter. But this requires us to re-interpret Eq. (B.124) \mathbf{r}_n defined there is for Bloch waves with
 1483 a different normalization condition from that in Eq. (B.136). Regarding $|n\mathbf{k}\rangle$ as an eigenstate of
 1484 the Hamiltonian playing the same role as $|\phi_n\rangle$, we have

$$\frac{a_x a_y}{(2\pi)^2} \int dk_x \int dk_y \langle n\mathbf{k} | n\mathbf{k} \rangle = \frac{a_x a_y}{(2\pi)^2} \int d^2\mathbf{k} \frac{(2\pi)^2}{a_x a_y} \delta(\mathbf{k}) = 1 \quad (\text{B.139})$$

1485 In other words,

$$\frac{a_y}{2\pi} \int dk_y \langle n\mathbf{k} | \mathbf{r} | n\mathbf{k} \rangle = \frac{1}{N_y} \sum_{k_y} \langle n\mathbf{k} | \mathbf{r} | n\mathbf{k} \rangle \rightarrow \frac{1}{a_y} \langle \phi_n(k) | x | \phi_n(k) \rangle \equiv x_{nk} \quad (\text{B.140})$$

1486 which corresponds to taking the expectation value of x in a given normalized eigenstate. There-
 1487 fore Eq. (B.125) applicable to the present case should be

$$\begin{aligned} C_n &= -\frac{1}{2\pi} \int dk \partial_k \left(\frac{2\pi}{L_x} x_{nk} \right) \\ &= \frac{1}{L_x} \left(x_{nk=\frac{\pi}{a_y}} - x_{nk=-\frac{\pi}{a_y}} \right) \end{aligned} \quad (\text{B.141})$$

1488 Due to the symmetry of $\phi_n(x, k) = \langle x | \phi_n(k) \rangle = \phi_n(x - x_k, k = 0)$, we have

$$\langle \phi_{nk} | x | \phi_{nk} \rangle = a_y x_k \quad (\text{B.142})$$

1489 As a result

$$\begin{aligned} C_n &= \frac{1}{L_x} \frac{\hbar}{eB} \left(\frac{\pi}{a_y} + \frac{\pi}{a_y} \right) \\ &= \frac{\hbar}{e} \frac{1}{B a_y L_x} \equiv \frac{\Phi_0}{\Phi} N_y \end{aligned} \quad (\text{B.143})$$

1490 where $N_y \equiv L_y/a_y$. However, this result is obtained by assuming that the period of k is $2\pi/a_y$. If
 1491 one wraps the 2D system into a cylinder parallel to $\hat{\mathbf{x}}$ so that k is quantized into

$$k = \frac{2\pi}{L_y} m \quad (\text{B.144})$$

1492 where m can be any integer. Then imagining that one inserts a flux (or phase) through the
 1493 cylinder defined by

$$\Phi_x \equiv \frac{e}{\hbar} AL_y \quad (\text{B.145})$$

1494 so that Φ_x enters the Landau level Hamiltonian as

$$H(\Phi_x) = \frac{p_x^2}{2m} + \frac{(p_y + \frac{\hbar}{L_y} \Phi_x + eBx)^2}{2m} \quad (\text{B.146})$$

1495 Then apparently the Hamiltonian is symmetric under $\Phi_x \rightarrow \Phi_x + 2\pi$, so that Φ_x can be viewed as
 1496 a pumping parameter. In the above language, this is equivalent to choosing k as the pumping
 1497 parameter but defining its period as

$$\frac{2\pi}{a_y} \rightarrow \frac{2\pi}{L_y} \quad (\text{B.147})$$

1498 The Chern number is thus defined as

$$\begin{aligned} C_n &= -\frac{1}{2\pi} \oint d\Phi_x \partial_{\Phi_x} \left(\frac{2\pi}{L_x} x_{nk} \right) \\ &= \frac{1}{L_x} \left(x_{nk=\frac{2\pi}{L_y}} - x_{nk=0} \right) \\ &= \frac{\Phi_0}{\Phi} \end{aligned} \quad (\text{B.148})$$

1499 The final result above is, however, not necessarily an integer. To see what is wrong with it, let
 1500 us now use the above cylinder picture to understand what is really going on when the flux Φ_x

1501 changes by 2π . Since the cylinder has periodic boundary condition along y , k is quantized as
 1502 mentioned above, which restricts the eigenstates $|\phi_n(k)\rangle$. This further constrains the values of
 1503 x_k , i.e., the center-of-mass of the wave functions $\phi_n(x, k) = \langle x | \phi_n(k) \rangle$:

$$\langle \phi_{nk} | x | \phi_{nk} \rangle = -\frac{2\pi m}{L_y} \frac{\hbar}{eB} = -\frac{\Phi_0}{BL_y} m \equiv -m\Delta x \quad (\text{B.149})$$

1504 where we recover the original normalization of the Landau level wavefunctions Eq. (B.135).
 1505 Note that from this we can also obtain the total number of electrons within a Landau level:

$$N = \frac{L_x}{\Delta x} = \frac{\Phi}{\Phi_0}. \quad (\text{B.150})$$

1506 When Φ_x changes by a period, which is equivalent to k changing by $\frac{2\pi}{L_y}$ or m changes by 1, the
 1507 center-of-mass of the Landau level wavefunction shifts along $\hat{\mathbf{x}}$ for all k by the same quantity
 1508 $\Phi_0/(BL_y)$, which is the same as their nearest neighbor spacing. Thus increasing Φ_x by 2π is
 1509 equivalent to removing a Landau level wavefunction at the boundary of $x = -L_x/2$ and adding
 1510 another one at $x = L_x/2$. That one electron is transported from one edge to the other edge is the
 1511 Chern number. However, Eq. (B.148) does not describe this integer directly. A modification that
 1512 leads to the direct correspondence is to multiply Eq. (B.148) by the total number of electrons N :

$$\begin{aligned} C_n &= -\frac{N}{2\pi} \oint d\Phi_x \partial_{\Phi_x} \left(\frac{2\pi}{L_x} x_{nk}(\Phi_x) \right) \\ &= -\frac{1}{2\pi} \sum_k \oint d\Phi_x \partial_{\Phi_x} \left(\frac{2\pi}{L_x} x_{nk}(\Phi_x) \right) \\ &\equiv -\frac{1}{2\pi} \oint d\Phi_x \partial_{\Phi_x} \left(\frac{2\pi}{L_x} X_n(\Phi_x) \right) \\ &= \frac{1}{L_x} [X_n(2\pi) - X_n(0)] \end{aligned} \quad (\text{B.151})$$

1513 where $X_n \equiv \sum_k x_{nk}$ is the X coordinate of the center of mass of *all* electrons multiplied by the
 1514 number of electrons within a Landau level. The above formula can be generally applied to other
 1515 systems that has translation symmetry only along one direction.

1516 More specifically, suppose we have a Hamiltonian H with eigenstates labeled by discrete
 1517 band indices n and some other quantum numbers q characterizing the degenerate states within
 1518 a band, and the eigenstates are simply normalized as $\langle nq|nq \rangle = 1$, then

$$X_n = \sum_q \langle nq|x|nq \rangle \quad (\text{B.152})$$

1519 One can get C_n by diagonalizing the Hamiltonian so that $H|nq \rangle = \epsilon_n|nq \rangle$, adding the flux so
 1520 that

$$H(\Phi_x)|nq(\Phi_x) \rangle = \epsilon_n(\Phi_x)|nq(\Phi_x) \rangle \quad (\text{B.153})$$

1521 and making sure that $\epsilon_n(\Phi_x)$ does not intersect with other bands as Φ_x increases by 2π . After
 1522 that, calculate

$$X_n(\Phi_x = 2\pi) - X_n(\Phi_x = 0) \quad (\text{B.154})$$

1523 and divide the above result by the finite length of the system along x . The result, if nonzero,
 1524 means the system has a finite Chern number despite the absence of translation symmetry.

1525 If, however, that ϵ_n depends on q as well. Namely $\epsilon_n \rightarrow \epsilon_n(q)$, one can still define the Chern
 1526 number by making sure that all eigenenergies $\epsilon_{nq}(\Phi_x)$ do not touch other bands as Φ_x increases
 1527 by 2π . The final step of calculating the Chern number stays unchanged.

Bibliography

- [1] David J. Griffiths. *Introduction to Electrodynamics*. Cambridge University Press, Cambridge New York Port Melbourne New Delhi Singapore, fifth edition edition, 2024.
- [2] Alexander Altland and Ben Simons. *Condensed Matter Field Theory*. Cambridge University Press, Cambridge, United Kingdom ; New York, NY, third edition edition, 2023.
- [3] Charles Kittel. *Introduction to Solid State Physics*. Wiley, Hoboken, NJ, global edition, [9th edition] edition, 2018.
- [4] Xiangang Wan, Ari M. Turner, Ashvin Vishwanath, and Sergey Y. Savrasov. Topological semimetal and Fermi-arc surface states in the electronic structure of pyrochlore iridates. *Phys. Rev. B*, 83(20):205101, May 2011.
- [5] Su-Yang Xu, Ilya Belopolski, Nasser Alidoust, Madhab Neupane, Guang Bian, Chenglong Zhang, Raman Sankar, Guoqing Chang, Zhujun Yuan, Chi-Cheng Lee, Shin-Ming Huang, Hao Zheng, Jie Ma, Daniel S. Sanchez, BaoKai Wang, Arun Bansil, Fangcheng Chou, Pavel P. Shibayev, Hsin Lin, Shuang Jia, and M. Zahid Hasan. Discovery of a Weyl fermion semimetal and topological Fermi arcs. *Science*, 349(6248):613–617, August 2015.
- [6] Zhilin Li, Hongxiang Chen, Shifeng Jin, Di Gan, Wenjun Wang, Liwei Guo, and Xiaolong Chen. Weyl Semimetal TaAs: Crystal Growth, Morphology, and Thermodynamics. *Crystal Growth & Design*, 16(3):1172–1175, March 2016.
- [7] D. A. Ivanov. Non-Abelian Statistics of Half-Quantum Vortices in p -Wave Superconductors. *Phys. Rev. Lett.*, 86(2):268–271, January 2001.
- [8] A. Yu Kitaev. Unpaired Majorana fermions in quantum wires. *Phys.-Usp.*, 44(10S):131, October 2001.

- [9] Jason Alicea, Yuval Oreg, Gil Refael, Felix von Oppen, and Matthew P. A. Fisher. Non-Abelian statistics and topological quantum information processing in 1D wire networks. *Nature Phys*, 7(5):412–417, May 2011.
- [10] Jay D. Sau, Roman M. Lutchyn, Sumanta Tewari, and S. Das Sarma. Generic New Platform for Topological Quantum Computation Using Semiconductor Heterostructures. *Phys. Rev. Lett.*, 104(4):040502, January 2010.
- [11] A. Yu. Kitaev. Fault-tolerant quantum computation by anyons. *Annals of Physics*, 303(1):2–30, January 2003.
- [12] Chetan Nayak, Steven H. Simon, Ady Stern, Michael Freedman, and Sankar Das Sarma. Non-Abelian anyons and topological quantum computation. *Rev. Mod. Phys.*, 80(3):1083–1159, September 2008.
- [13] David Aasen, Michael Hell, Ryan V. Mishmash, Andrew Higginbotham, Jeroen Danon, Martin Leijnse, Thomas S. Jespersen, Joshua A. Folk, Charles M. Marcus, Karsten Flensberg, and Jason Alicea. Milestones Toward Majorana-Based Quantum Computing. *Phys. Rev. X*, 6(3):031016, August 2016.
- [14] N. Read and Dmitry Green. Paired states of fermions in two dimensions with breaking of parity and time-reversal symmetries and the fractional quantum Hall effect. *Phys. Rev. B*, 61(15):10267–10297, April 2000.
- [15] Jean-Pascal Brison. P-Wave Superconductivity and d-Vector Representation. In Hervé Bulou, Loïc Joly, Jean-Michel Mariot, and Fabrice Scheurer, editors, *Magnetism and Accelerator-Based Light Sources*, Springer Proceedings in Physics, pages 165–204, Cham, 2021. Springer International Publishing.
- [16] V. Mourik, K. Zuo, S. M. Frolov, S. R. Plissard, E. P. A. M. Bakkers, and L. P. Kouwenhoven. Signatures of Majorana Fermions in Hybrid Superconductor-Semiconductor Nanowire Devices. *Science*, 336(6084):1003–1007, May 2012.

- 1575 [17] Leonid P. Rokhinson, Xinyu Liu, and Jacek K. Furdyna. The fractional a.c. Josephson ef-
1576 fect in a semiconductor–superconductor nanowire as a signature of Majorana particles.
1577 *Nature Phys*, 8(11):795–799, November 2012.
- 1578 [18] M. T. Deng, C. L. Yu, G. Y. Huang, M. Larsson, P. Caroff, and H. Q. Xu. Anomalous Zero-Bias
1579 Conductance Peak in a Nb–InSb Nanowire–Nb Hybrid Device. *Nano Lett.*, 12(12):6414–
1580 6419, December 2012.
- 1581 [19] T.-P. Choy, J. M. Edge, A. R. Akhmerov, and C. W. J. Beenakker. Majorana fermions emerg-
1582 ing from magnetic nanoparticles on a superconductor without spin-orbit coupling. *Phys.*
1583 *Rev. B*, 84(19):195442, November 2011.
- 1584 [20] Bernd Braunecker and Pascal Simon. Interplay between Classical Magnetic Moments and
1585 Superconductivity in Quantum One-Dimensional Conductors: Toward a Self-Sustained
1586 Topological Majorana Phase. *Phys. Rev. Lett.*, 111(14):147202, October 2013.
- 1587 [21] Jelena Klinovaja, Peter Stano, Ali Yazdani, and Daniel Loss. Topological Superconductivity
1588 and Majorana Fermions in RKKY Systems. *Phys. Rev. Lett.*, 111(18):186805, November
1589 2013.
- 1590 [22] S. Nadj-Perge, I. K. Drozdov, B. A. Bernevig, and Ali Yazdani. Proposal for realizing
1591 Majorana fermions in chains of magnetic atoms on a superconductor. *Phys. Rev. B*,
1592 88(2):020407, July 2013.
- 1593 [23] Stevan Nadj-Perge, Ilya K. Drozdov, Jian Li, Hua Chen, Sangjun Jeon, Jungpil Seo, Allan H.
1594 MacDonald, B. Andrei Bernevig, and Ali Yazdani. Observation of Majorana fermions in
1595 ferromagnetic atomic chains on a superconductor. *Science*, 346(6209):602–607, October
1596 2014.
- 1597 [24] Lucas Schneider, Philip Beck, Jannis Neuhaus-Steinmetz, Levente Rózsa, Thore Posske,
1598 Jens Wiebe, and Roland Wiesendanger. Precursors of Majorana modes and their length-

1599 dependent energy oscillations probed at both ends of atomic Shiba chains. *Nat. Nan-*
1600 *otechnol.*, 17(4):384–389, April 2022.

1601 [25] Liang Fu and C. L. Kane. Superconducting proximity effect and Majorana fermions at the
1602 surface of a topological insulator. *Phys. Rev. Lett.*, 100(9):096407, March 2008.

1603 [26] Pavan Hosur, Pouyan Ghaemi, Roger S. K. Mong, and Ashvin Vishwanath. Majorana
1604 Modes at the Ends of Superconductor Vortices in Doped Topological Insulators. *Phys.*
1605 *Rev. Lett.*, 107(9):097001, August 2011.

1606 [27] Andrew C. Potter and Patrick A. Lee. Engineering a $p+\text{ip}$ superconductor:
1607 Comparison of topological insulator and Rashba spin-orbit-coupled materials. *Phys. Rev.*
1608 *B*, 83(18):184520, May 2011.

1609 [28] M. Veldhorst, M. Snelder, M. Hoek, C. G. Molenaar, D. P. Leusink, A. A. Golubov,
1610 H. Hilgenkamp, and A. Brinkman. Magnetotransport and induced superconductivity in
1611 Bi based three-dimensional topological insulators. *physica status solidi (RRL) – Rapid*
1612 *Research Letters*, 7(1-2):26–38, 2013.

1613 [29] Chui-Zhen Chen, Ying-Ming Xie, Jie Liu, Patrick A. Lee, and K. T. Law. Quasi-one-
1614 dimensional quantum anomalous Hall systems as new platforms for scalable topological
1615 quantum computation. *Phys. Rev. B*, 97(10):104504, March 2018.

1616 [30] Yongxin Zeng, Chao Lei, Gaurav Chaudhary, and Allan H. MacDonald. Quantum anoma-
1617 lous Hall Majorana platform. *Phys. Rev. B*, 97(8):081102, February 2018.

1618 [31] Ying-Ming Xie, Xue-Jian Gao, Tai-Kai Ng, and K. T. Law. Creating Localized Majorana Zero
1619 Modes in Quantum Anomalous Hall Insulator/Superconductor Heterostructures with a
1620 Scissor, June 2021.

1621 [32] Yuval Oreg, Gil Refael, and Felix von Oppen. Helical Liquids and Majorana Bound States
1622 in Quantum Wires. *Phys. Rev. Lett.*, 105(17):177002, October 2010.

- 1623 [33] Roman M. Lutchyn, Tudor D. Stanescu, and S. Das Sarma. Search for Majorana Fermions
1624 in Multiband Semiconducting Nanowires. *Phys. Rev. Lett.*, 106(12):127001, March 2011.
- 1625 [34] Andrew C. Potter and Patrick A. Lee. Topological superconductivity and Majorana
1626 fermions in metallic surface states. *Phys. Rev. B*, 85(9):094516, March 2012.
- 1627 [35] Jian Li, Titus Neupert, Zhijun Wang, A. H. MacDonald, A. Yazdani, and B. Andrei Bernevig.
1628 Two-dimensional chiral topological superconductivity in Shiba lattices. *Nat Commun*,
1629 7(1):12297, July 2016.
- 1630 [36] Chao Lei, Hua Chen, and Allan H. MacDonald. Ultrathin Films of Superconducting
1631 Metals as a Platform for Topological Superconductivity. *Phys. Rev. Lett.*, 121(22):227701,
1632 November 2018.
- 1633 [37] Annica M. Black-Schaffer and Jacob Linder. Majorana fermions in spin-orbit-coupled
1634 ferromagnetic Josephson junctions. *Phys. Rev. B*, 84(18):180509, November 2011.
- 1635 [38] Falko Pientka, Alessandro Romito, Mathias Duckheim, Yuval Oreg, and Felix von Oppen.
1636 Signatures of topological phase transitions in mesoscopic superconducting rings. *New J.*
1637 *Phys.*, 15(2):025001, February 2013.
- 1638 [39] Michael Hell, Martin Leijnse, and Karsten Flensberg. Two-Dimensional Platform for Net-
1639 works of Majorana Bound States. *Phys. Rev. Lett.*, 118(10):107701, March 2017.
- 1640 [40] Antonio Fornieri, Alexander M. Whiticar, F. Setiawan, Elías Portolés, Asbjørn C. C. Drach-
1641 mann, Anna Keselman, Sergei Gronin, Candice Thomas, Tian Wang, Ray Kallagher, Geof-
1642 frey C. Gardner, Erez Berg, Michael J. Manfra, Ady Stern, Charles M. Marcus, and Fabrizio
1643 Nichele. Evidence of topological superconductivity in planar Josephson junctions. *Na-*
1644 *ture*, 569(7754):89–92, May 2019.
- 1645 [41] Hechen Ren, Falko Pientka, Sean Hart, Andrew T. Pierce, Michael Kosowsky, Lukas
1646 Lunczer, Raimund Schlereth, Benedikt Scharf, Ewelina M. Hankiewicz, Laurens W.

Molenkamp, Bertrand I. Halperin, and Amir Yacoby. Topological superconductivity in a phase-controlled Josephson junction. *Nature*, 569(7754):93–98, May 2019.

[42] Benedikt Scharf, Falko Pientka, Hechen Ren, Amir Yacoby, and Ewelina M. Hankiewicz. Tuning topological superconductivity in phase-controlled Josephson junctions with Rashba and Dresselhaus spin-orbit coupling. *Phys. Rev. B*, 99(21):214503, June 2019.

[43] Tong Zhou, Matthieu C. Dartiailh, William Mayer, Jong E. Han, Alex Matos-Abiague, Javad Shabani, and Igor Žutić. Phase Control of Majorana Bound States in a Topological X Junction. *Phys. Rev. Lett.*, 124(13):137001, April 2020.

[44] Jin-Peng Xu, Mei-Xiao Wang, Zhi Long Liu, Jian-Feng Ge, Xiaojun Yang, Canhua Liu, Zhu An Xu, Dandan Guan, Chun Lei Gao, Dong Qian, Ying Liu, Qiang-Hua Wang, Fu-Chun Zhang, Qi-Kun Xue, and Jin-Feng Jia. Experimental Detection of a Majorana Mode in the core of a Magnetic Vortex inside a Topological Insulator-Superconductor Bi_2Te_3 / NbSe_2 Heterostructure. *Phys. Rev. Lett.*, 114(1):017001, January 2015.

[45] S. M. Albrecht, A. P. Higginbotham, M. Madsen, F. Kuemmeth, T. S. Jespersen, J. Nygård, P. Krogstrup, and C. M. Marcus. Exponential protection of zero modes in Majorana islands. *Nature*, 531(7593):206–209, March 2016.

[46] Hao-Hua Sun, Kai-Wen Zhang, Lun-Hui Hu, Chuang Li, Guan-Yong Wang, Hai-Yang Ma, Zhu-An Xu, Chun-Lei Gao, Dan-Dan Guan, Yao-Yi Li, Canhua Liu, Dong Qian, Yi Zhou, Liang Fu, Shao-Chun Li, Fu-Chun Zhang, and Jin-Feng Jia. Majorana Zero Mode Detected with Spin Selective Andreev Reflection in the Vortex of a Topological Superconductor. *Phys. Rev. Lett.*, 116(25):257003, June 2016.

[47] Dongfei Wang, Lingyuan Kong, Peng Fan, Hui Chen, Shiyu Zhu, Wen Yao Liu, Lu Cao, Yujie Sun, Shixuan Du, John Schneeloch, Ruidan Zhong, Genda Gu, Liang Fu, Hong Ding, and Hong-Jun Gao. Evidence for Majorana bound states in an iron-based superconductor. *Science*, 362(6412):333–335, October 2018.

- [48] Berthold Jäck, Yonglong Xie, Jian Li, Sangjun Jeon, B. Andrei Bernevig, and Ali Yazdani. Observation of a Majorana zero mode in a topologically protected edge channel. *Science*, 364(6447):1255–1259, June 2019.
- [49] Sujit Manna, Peng Wei, Yingming Xie, Kam Tuen Law, Patrick A. Lee, and Jagadeesh S. Moodera. Signature of a pair of Majorana zero modes in superconducting gold surface states. *Proceedings of the National Academy of Sciences*, 117(16):8775–8782, April 2020.
- [50] Geoffrey L. Fatin, Alex Matos-Abiague, Benedikt Scharf, and Igor Žutić. Wireless Majorana Bound States: From Magnetic Tunability to Braiding. *Phys. Rev. Lett.*, 117(7):077002, August 2016.
- [51] Jay D. Sau and S. Das Sarma. Realizing a robust practical Majorana chain in a quantum-dot-superconductor linear array. *Nat Commun*, 3(1):964, July 2012.
- [52] Martin Leijnse and Karsten Flensberg. Parity qubits and poor man’s Majorana bound states in double quantum dots. *Phys. Rev. B*, 86(13):134528, October 2012.
- [53] Tom Dvir, Guanzhong Wang, Nick van Loo, Chun-Xiao Liu, Grzegorz P. Mazur, Alberto Bordin, Sebastiaan L. D. ten Haaf, Ji-Yin Wang, David van Driel, Francesco Zatelli, Xiang Li, Filip K. Malinowski, Sasa Gazibegovic, Ghada Badawy, Erik P. A. M. Bakkers, Michael Wimmer, and Leo P. Kouwenhoven. Realization of a minimal Kitaev chain in coupled quantum dots. *Nature*, 614(7948):445–450, February 2023.
- [54] Torsten Karzig, Christina Knapp, Roman M. Lutchyn, Parsa Bonderson, Matthew B. Hastings, Chetan Nayak, Jason Alicea, Karsten Flensberg, Stephan Plugge, Yuval Oreg, Charles M. Marcus, and Michael H. Freedman. Scalable designs for quasiparticle-poisoning-protected topological quantum computation with Majorana zero modes. *Phys. Rev. B*, 95(23):235305, June 2017.

- 1695 [55] Andrew C. Potter and Patrick A. Lee. Multichannel Generalization of Kitaev's Majorana End States and a Practical Route to Realize Them in Thin Films. *Phys. Rev. Lett.*, 105(22):227003, November 2010.
- 1696
- 1697
- 1698 [56] Jian Li, Titus Neupert, B. Andrei Bernevig, and Ali Yazdani. Manipulating Majorana zero modes on atomic rings with an external magnetic field. *Nat Commun*, 7(1):10395, January 2016.
- 1699
- 1700
- 1701 [57] Tudor E. Pahomi, Manfred Sigrist, and Alexey A. Soluyanov. Braiding Majorana corner modes in a second-order topological superconductor. *Phys. Rev. Res.*, 2(3):032068, September 2020.
- 1702
- 1703
- 1704 [58] Song-Bo Zhang, Alessio Calzona, and Björn Trauzettel. All-electrically tunable networks of Majorana bound states. *Phys. Rev. B*, 102(10):100503, September 2020.
- 1705
- 1706 [59] Song-Bo Zhang, W. B. Rui, Alessio Calzona, Sang-Jun Choi, Andreas P. Schnyder, and Björn Trauzettel. Topological and holonomic quantum computation based on second-order topological superconductors. *Phys. Rev. Res.*, 2(4):043025, October 2020.
- 1707
- 1708
- 1709 [60] O. Pietzsch, S. Okatov, A. Kubetzka, M. Bode, S. Heinze, A. Lichtenstein, and R. Wiesendanger. Spin-Resolved Electronic Structure of Nanoscale Cobalt Islands on Cu(111). *Phys. Rev. Lett.*, 96(23):237203, June 2006.
- 1710
- 1711
- 1712 [61] Alessandro Romito, Jason Alicea, Gil Refael, and Felix von Oppen. Manipulating Majorana fermions using supercurrents. *Phys. Rev. B*, 85(2):020502, January 2012.
- 1713
- 1714 [62] Kazuaki Takasan, Shuntaro Sumita, and Youichi Yanase. Supercurrent-induced topological phase transitions. *Phys. Rev. B*, 106(1):014508, July 2022.
- 1715
- 1716 [63] T. Hyart, B. van Heck, I. C. Fulga, M. Burrello, A. R. Akhmerov, and C. W. J. Beenakker. Flux-controlled quantum computation with Majorana fermions. *Phys. Rev. B*, 88(3):035121, July 2013.
- 1717
- 1718

- [64] Olesia Dmytruk, Manisha Thakurathi, Daniel Loss, and Jelena Klinovaja. Majorana bound states in double nanowires with reduced Zeeman thresholds due to supercurrents. *Phys. Rev. B*, 99(24):245416, June 2019.
- [65] P. G. De Gennes. *Superconductivity Of Metals And Alloys*. CRC Press, Boca Raton, March 2018.
- [66] *See Supplemental Material at [url]*.
- [67] Guan-Hao Feng and Hong-Hao Zhang. Probing robust Majorana signatures by crossed Andreev reflection with a quantum dot. *Phys. Rev. B*, 105(3):035148, January 2022.
- [68] Bradraj Pandey, Nitin Kaushal, Gonzalo Alvarez, and Elbio Dagotto. Majorana zero modes in Y-shape interacting Kitaev wires. *npj Quantum Mater.*, 8(1):1–8, September 2023.
- [69] Jian Li, Hua Chen, Ilya K. Drozdov, A. Yazdani, B. Andrei Bernevig, and A. H. MacDonald. Topological superconductivity induced by ferromagnetic metal chains. *Phys. Rev. B*, 90(23):235433, December 2014.
- [70] Ryan V. Mishmash, Bela Bauer, Felix von Oppen, and Jason Alicea. Dephasing and leakage dynamics of noisy Majorana-based qubits: Topological versus Andreev. *Phys. Rev. B*, 101(7):075404, February 2020.
- [71] Gábor Széchenyi and András Pályi. Parity-to-charge conversion for readout of topological majorana qubits. *Phys. Rev. B*, 101:235441, Jun 2020.
- [72] K. v. Klitzing, G. Dorda, and M. Pepper. New method for high-accuracy determination of the fine-structure constant based on quantized hall resistance. *Phys. Rev. Lett.*, 45(6):494–497, August 1980.
- [73] A. H. Castro Neto, F. Guinea, N. M. R. Peres, K. S. Novoselov, and A. K. Geim. The electronic properties of graphene. *Rev. Mod. Phys.*, 81(1):109–162, January 2009.

- [74] K. S. Novoselov, A. K. Geim, S. V. Morozov, D. Jiang, M. I. Katsnelson, I. V. Grigorieva, Dubonos S. V., and A. A. Firsov. Two-dimensional gas of massless Dirac fermions in graphene. *Nature Physics*, 438:197, 2005.
- [75] Yuanbo Zhang, Yan-Wen Tan, Horst L. Stormer, and Philip Kim. Experimental observation of the quantum Hall effect and Berry's phase in graphene. *Nature Physics*, 438:201, 2005.
- [76] Netanel H. Lindner, Gil Refael, and Victor Galitski. Floquet topological insulator in semiconductor quantum wells. *Nature Physics*, 7:490, 2011.
- [77] André Eckardt and Egidijus Anisimovas. High-frequency approximation for periodically driven quantum systems from a Floquet-space perspective. *New J. Phys.*, 17:093039, 2015.
- [78] Mikael C. Rechtsman, Julia M. Zeuner, Yonatan Plotnik, Yaakov Lumer, Daniel Podolsky, Felix Dreisow, Stefan Nolte, Mordechai Segev, and Alexander Szameit. Photonic floquet topological insulators. *Nature Physics*, 496:196, 2013.
- [79] Y. H. Wang, H. Steinberg, P. Jarillo-Herrero, and N. Gedik. Observation of floquet-bloch states on the surface of a topological insulator. *Science*, 342(6157):453–457, 2013.
- [80] Hongbin Zhang, Jiandong Yao, Jianmei Shao, Hai Li, Shuwei Li, Dinghua Bao, Chengxin Wang, and Guowei Yang. Anomalous photoelectric effect of a polycrystalline topological insulator film. *Scientific Reports*, 4:5876, 2014.
- [81] J. W. McIver, B. Schulte, F.-U. Stein, T. Matsuyama, G. Jotzu, G. Meier, and A. Cavalleri. Light-induced anomalous Hall effect in graphene. *Nature Physics*, 11:123, 2019.
- [82] Marco Merboldt, Michael Schüler, David Schmitt, Jan Philipp Bange, Wiebke Bennecke, Karun Gadge, Klaus Pierz, Hans Werner Schumacher, Davood Momeni, Daniel Steil, Salvatore R. Manmana, Michael Sentef, Marcel Reutz, and Stefan Mathias. Observation of Floquet states in graphene, April 2024.

- [83] Dongsung Choi, Masataka Mogi, Umberto De Giovannini, Doron Azoury, Baiqing Lv, Yifan Su, Hannes Hübener, Angel Rubio, and Nuh Gedik. Direct observation of Floquet-Bloch states in monolayer graphene, April 2024.
- [84] Jon H. Shirley. Solution of the schrödinger equation with a hamiltonian periodic in time. *Phys. Rev.*, 138(4B):B979–B987, May 1965.
- [85] Hideo Sambe. Steady states and quasienergies of a quantum-mechanical system in an oscillating field. *Phys. Rev. A*, 7(6):2203–2213, June 1973.
- [86] Milena Grifoni and Peter Hänggi. Driven quantum tunneling. *Physics Reports*, 304:229, 1998.
- [87] M. Bukov, L. D’Alessio, and A. Polkovnikov. Universal high-frequency behavior of periodically driven systems: From dynamical stabilization to Floquet engineering. *Advances in Physics*, 64:139, 2015.
- [88] N. Goldman and J. Dalibard. Periodically driven quantum systems: Effective hamiltonians and engineered gauge fields. *Phys. Rev. X*, 4(3):031027, August 2014.
- [89] Saar Rahav, Ido Gilary, and Shmuel Fishman. Effective Hamiltonians for periodically driven systems. *Phys. Rev. A*, 68(1):013820, July 2003.
- [90] A. P. Itin and M. I. Katsnelson. Effective hamiltonians for rapidly driven many-body lattice systems: Induced exchange interactions and density-dependent hoppings. *Phys. Rev. Lett.*, 115(7):075301, August 2015.
- [91] Takahiro Mikami, Sota Kitamura, Kenji Yasuda, Naoto Tsuji, Takashi Oka, and Hideo Aoki. Brillouin-Wigner theory for high-frequency expansion in periodically driven systems: Application to Floquet topological insulators. *Phys. Rev. B*, 93(14):144307, April 2016.

- 1789 [92] E. S. Mananga and T. Charpentier. Introduction of the Floquet-Magnus expansion in
1790 solid-state nuclear magnetic resonance spectroscopy. *The Journal of Chemical Physics*,
1791 135:044109, 2011.
- 1792 [93] T. Kuwahara, T. Mori, and K. Saito. Floquet–Magnus theory and generic transient dynam-
1793 ics in periodically driven many-body quantum systems. *Annals of Physics*, 367:96, 2016.
- 1794 [94] A. López, A. Scholz, Z. Z. Sun, and J. Schliemann. Graphene with time-dependent spin-
1795 orbit coupling: Truncated Magnus expansion approach. *Eur. Phys. J. B*, 86:366, 2013.
- 1796 [95] F. Casas, J. A. Oteo, and J. Ros. Floquet theory: Exponential perturbative treatment. *J.*
1797 *Phys. A*, 34:3379, 2001.
- 1798 [96] Takuya Kitagawa, Takashi Oka, Arne Brataas, Liang Fu, and Eugene Demler. Trans-
1799 port properties of nonequilibrium systems under the application of light: Photoinduced
1800 quantum Hall insulators without Landau levels. *Phys. Rev. B*, 84(23):235108, December
1801 2011.
- 1802 [97] F. D. M. Haldane. Model for a quantum hall effect without landau levels: Condensed-
1803 matter realization of the "Parity Anomaly". *Phys. Rev. Lett.*, 61(18):2015–2018, October
1804 1988.
- 1805 [98] Andrei Kirilyuk, Alexey V. Kimel, and Theo Rasing. Ultrafast optical manipulation of mag-
1806 netic order. *Rev. Mod. Phys.*, 82(3):2731–2784, September 2010.
- 1807 [99] J. H. Mentink, K. Balzer, and M. Eckstein. Ultrafast and reversible control of the exchange
1808 interaction in Mott insulators. *Nature Communications*, 6:6708, 2015.
- 1809 [100] L. Stojchevska, I. Vaskivskyi, T. Mertelj, P. Kusar, D. Svetin, S. Brazovskii, and D. Mihailovic.
1810 Ultrafast switching to a stable hidden quantum state in an electronic crystal. *Science*,
1811 344(6180):177–180, 2014.

- 1812 [101] Adolfo G. Grushin, Álvaro Gómez-León, and Titus Neupert. Floquet fractional chern in-
1813 sulators. *Phys. Rev. Lett.*, 112(15):156801, April 2014.
- 1814 [102] Mark S. Rudner and Netanel H. Lindner. Band structure engineering and non-
1815 equilibrium dynamics in Floquet topological insulators. *Nat Rev Phys*, 2(5):229–244, May
1816 2020.
- 1817 [103] Nina Bielinski, Rajas Chari, Julian May-Mann, Soyeun Kim, Jack Zwettler, Yujun
1818 Deng, Anuva Aishwarya, Subhajit Roychowdhury, Chandra Shekhar, Makoto Hashimoto,
1819 Donghui Lu, Jiaqiang Yan, Claudia Felser, Vidya Madhavan, Zhi-Xun Shen, Taylor L.
1820 Hughes, and Fahad Mahmood. Floquet–Bloch manipulation of the Dirac gap in a topo-
1821 logical antiferromagnet. *Nat. Phys.*, pages 1–6, January 2025.
- 1822 [104] Ervand Kandelaki and Mark S. Rudner. Many-body dynamics and gap opening in inter-
1823 acting periodically driven systems. *Phys. Rev. Lett.*, 121(3):036801, July 2018.
- 1824 [105] G. Juzeliūnas and P. Öhberg. Slow light in degenerate fermi gases. *Phys. Rev. Lett.*,
1825 93(3):033602, July 2004.
- 1826 [106] J. Ruseckas, G. Juzeliūnas, P. Öhberg, and M. Fleischhauer. Non-abelian gauge potentials
1827 for ultracold atoms with degenerate dark states. *Phys. Rev. Lett.*, 95(1):010404, June 2005.
- 1828 [107] Shi-Liang Zhu, Hao Fu, C.-J. Wu, S.-C. Zhang, and L.-M. Duan. Spin hall effects for cold
1829 atoms in a light-induced gauge potential. *Phys. Rev. Lett.*, 97(24):240401, December 2006.
- 1830 [108] Jean Dalibard, Fabrice Gerbier, Gediminas Juzeliūnas, and Patrik Öhberg. Colloquium:
1831 Artificial gauge potentials for neutral atoms. *Rev. Mod. Phys.*, 83(4):1523–1543, November
1832 2011.
- 1833 [109] N Goldman, G Juzeliūnas, P Öhberg, and I B Spielman. Light-induced gauge fields for
1834 ultracold atoms. *Reports on Progress in Physics*, 77(12):126401, November 2014.

- 1835 [110] Hyunki Shim, Francesco Monticone, and Owen D. Miller. Fundamental Limits to the
1836 Refractive Index of Transparent Optical Materials. *Advanced Materials*, 33(43):2103946,
1837 2021.
- 1838 [111] Tatiana Amotchkina, Michael Trubetskov, Daniel Hahner, and Vladimir Pervak. Charac-
1839 terization of e-beam evaporated Ge, YbF₃, ZnS, and LaF₃ thin films for laser-oriented
1840 coatings. *Appl Opt*, 59(5):A40–A47, February 2020.